Sampo Mäkelä

Reflectarray for 120-GHz radar application - antenna element characterization with near-field measurements

School of Electrical Engineering

Thesis submitted for examination for the degree of Master of Science in Technology.

Espoo 9th May 2014

Thesis supervisor:

Professor Antti Räisänen

Thesis instructor:

D. Sc. (Tech.) Aleksi Tamminen

Aalto University
School of Electrical
Engineering

AALTO UNIVERSITY
SCHOOL OF ELECTRICAL ENGINEERING

ABSTRACT OF THE
MASTER'S THESIS

Author: Sampo Mäkelä

Title: Reflectarray for 120-GHz radar application - antenna element characterization with near-field measurements

Date: April 30, 2014 Language: English Number of pages: 83

Department of Radio Science and Technology

Professorship: Radio Engineering Code: S-26

Supervisor: Professor Antti Räisänen

Instructor: D. Sc. (Tech.) Aleksi Tamminen

This thesis presents the near-field measurements of a 120-GHz reflectarray (RA), which is developed to a short distance millimeter-wave radar application. The reconfigurable RA under development consists of 3700 coplanar patch antenna (CPA) elements, which are controlled by micro-electro-mechanical (MEMS) phase shifters. Static prototype RAs preceding the MEMS-controlled one are manufactured for measurements. The fundamentals of reflectarray design and analysis are described followed by an introduction of the main characteristics of the manufactured static reflectarrays. Beam patterns are measured at a 3-m distance and compared with the calculated ones. The plane-wave spectrum (PWS) and the diffraction efficiency of the reflectarray are determined with near-field imaging of the antenna aperture field. A reflection measurement method is developed for characterization of the individual antenna elements in the RA. The method has been modeled to validate the functionality of calibration and parameter extraction.

The measured beam patterns are in a good agreement with calculations in beam width and direction, but the presence of a strong specular component was observed in the measured PWS. RAs suffer from over-etching, which increases the resonant frequency. It is estimated to be 132.7 GHz, where the level of the main beam is increased 7.4–8.7 dB compared to those measured with 120 GHz. The proposed reflection measurement method proved to be sufficient for distinguishing the differently tuned elements in both amplitude and phase. The measured phase shift of the reflection coefficient varies from 20° to 190° and the designed phase shift of 90° is reached only with open-ended 195 µm and short-circuited 200 µm stubs. The measured diffraction efficiency is in range of 0.02–0.2 for differently tuned elements and it is in line with one calculated by a method based on computational back-propagation of the measured PWS.

Keywords: reflectarray, near-field measurements, millimeter-wave, waveguide calibration, beam pattern measurements

AALTO-YLIOPISTO
SÄHKÖTEKNIIKAN KORKEAKOULU

DIPLOMITYÖN
TIIVISTELMÄ

Tekijä: Sampo Mäkelä

Työn nimi: Heijastusryhmäantenni 120 GHz:n tutkasovellukseen - antennielementtien karakterisointi lähikenttämittauksin

Päivämäärä: 30.4.2014 Kieli: Englanti Sivumäärä: 83

Radiotieteen ja -tekniikan laitos

Professuuri: Radiotekniikka Koodi: S-26

Valvoja: Professori Antti Räisänen

Ohjaaja: TkT Aleksi Tamminen

Tämän diplomityön käsittelemä heijastusryhmäantenni, jota tutkitaan lähikenttämittauksin, on suunnitteilla 120 GHz:n lähialueen millimetriaaltotutkasovellukseen. Kehitteillä oleva sähköisesti keilaava heijastusryhmäantenni sisältää noin 3700 antennielementtiä, joita ohjataan mikrosähkömekaanisilla (MEMS) vaiheensiirtimillä. Ennen sähköisesti keilaavaa prototyyppiä antennista on valmistettu mittauksia varten staattiset versiot, joissa MEMS-vaiheensiirtimet on korvattu siirtojohdoilla, ja niiden pituutta muuttamalla aikaansaadaan sopiva vaiheensiirto. Sen toimintaperiaate, suunnitteluperusteet, analyysi ja valmistettujen antennien ominaisuudet on selitetty työn kirjallisuuskatsauksessa. Antennin säteilykuviot on mitattu kolmen metrin etäisyydeltä, ja niitä on verrattu laskennallisiin vastaaviin. Tasoaaltospektri ja diffraktiohyötysuhde on määritetty mittaamalla antennin apertuurikenttää lähietäisyydeltä. Yksittäisten antennielementtien karakterisointiin kehitetty heijastusmittausmenetelmä on mallinnettu kalibroinnin ja mitattujen parametrien erottelun varmistamiseksi.

Mitatut säteilykuviot vastaavat hyvin laskennallisia keilanleveyden ja -suunnan osalta, mutta mitatussa tasoaaltospektrissä havaittiin voimakas peiliheijastuskomponentti. Valmistetuissa antenneissa ilmeni ylietsaantumista, mikä kasvattaa elementtien resonanssitaajuutta. Sen havaittiin kasvaneen noin 132.7 GHz:iin, missä pääkeilan amplitudi oli 7.4–8.7 dB:ä suurempi kuin 120 GHz:llä mitatuissa. Tutkittavalla heijastusmittausmenetelmällä onnistuttiin erottelemaan sekä amplitudi että suhteellinen vaiheensiirto erilailla viritetyille elementeille. Heijastuskertoimen vaiheensiirto sijoittuu 20°:n ja 190°:n välille ja suunniteltu 90°:n vaiheensiirto saavutettiin vain avoimella piirillä päätetyllä 195 µm:n ja oikosuljetulla 200 µm:n siirtojohdolla. Mitattu diffraktiohyötysuhde vaihtelee 0.02:n ja 0.2:n välillä, mikä on linjassa tasoaaltospektristä holografisella projektiomenetelmällä määritetyn kanssa.

Avainsanat: Heijastusryhmäantenni, lähikenttämittaus, millimetriaalto, kalibrointi, säteilykuvion mittaus

Preface

This Master's thesis was written at the Aalto University Department of Radio Science and Engineering. The work was funded trough the SIMIDS project by the Finnish Agency for Technology and Innovation (TEKES), and by the Academy of Finland under the Centre of Excellence in Smart Radios and Wireless Research (SMARAD) Programme. First of all I am truly grateful to my supervisor Professor Antti Räisänen for offering me this opportunity to work on such challenging and interesting topics under the field of millimeter-wave engineering. Very warm thanks is directed to my instructor Dr. Aleksi Tamminen whose guidance has helped me to solve numerous key problems and put the thesis back on the right track. I would also like to thank all of my colleagues at the Department and my immediate supervisor Dr. Juha Ala-Laurinaho for his invaluable guidance and an encouraging advisement towards a scientific career – maybe someday.

I express my gratitude to my mother Päivi, father Ilkka, brothers Teppo and Kimmo, nephew Aatu and especially to my girlfriend Tuula for all the support and encouragement during my long-lasting studies. Lastly I want to thank my wonderful friends from both academia and elsewhere with whom I have spend most of my time with along all these years, especially: Ada, Anna, Anne, Emilia, Heini, Ida, Jani, Juho, Jukka, Jussi, Mauno, Mikko, Niilo, Olli, Pietu, Sanna H., Sanna Y., Tuomas, Tuomo, and Vellu. Special thanks is also directed to my friends from Skipoli and FLOB.

Northern Tapiola, Espoo, Walpurgis Eve, 2014

Sampo Mäkelä

Contents

Symbols and abbreviations

Symbols

α	attenuation constant
β	phase constant
γ	complex propagation constant [m^{-1}]
Γ	reflection coefficient
ΔL	effective length extension [m]
ϵ	permittivity ($\epsilon_0 \approx 8.854 \times 10^{-12}$ [F/m])
ϵ_r	relative permittivity
η	wave impedance (in free space, $\eta_0 = \frac{\lvert\mathbf{E}\rvert}{\lvert\mathbf{H}\rvert} = 120\pi\Omega$)
η_e	reflectarray element efficiency
θ	azimuthal angle [°]
λ	wavelength [m]
μ	permeability ($\mu_0 = 4\pi \times 10^{-7}$ [H/m])
ρ	alternative symbol for reflection coefficient
ϕ	polar angle [°]
$\phi_R(x_i, y_i)$	required relative phase shift of the i:th element from the center of the RA [rad]
ϕ_s	spatial path difference [rad]
ω	angular frequency [rad/s]
c	velocity of propagation (speed of light in vacuum, $c_0 \approx 3 \times 10^8$ [m/s])
C	coupling factor or alternatively an arbitrary phase constant
D	directivity
E_{DF}	directivity error
E_{RF}	reflection tracking error
E_{SF}	port match error
f	frequency [Hz]
G	antenna gain
I	isolation
j	imaginary unit ($j^2 = -1$)
k	wave number (in free space, $k_0 = \frac{2\pi}{\lambda_0}$)
k_x, k_y, k_z	spatial frequency components [rad/m]
L	insertion loss or alternatively, length [m]
r	radial distance [m]
S, S_a	surface [m^2]
$[S_{mn}]$	scattering matrix
U	uncertainty
V	volume [m^3]
Z	impedance [Ω]

$\mathbf{A}$	magnetic vector potential [Vs/m]
$\mathbf{d_i}$	vector from the feed to the i:th element
$\mathbf{d_i'}$	vector from the i:th element to the desired focus
$\mathbf{E}$	electric field strength [V/m]
$\mathbf{E_a}(S')$	tangential electric field in a closed surface S' [V/m]
$\mathbf{E}_\theta, \mathbf{E}_\phi$	polar components of the radiation pattern [V/m]
$\mathbf{F}$	electric vector potential [V/m]
$\boldsymbol{f}(\theta,\phi), \boldsymbol{g}(\theta,\phi)$	two-dimensional Fourier transforms of the aperture fields
$\overline{\overline{G}}(\mathbf{r}-\mathbf{r}')$	Green's dyad
$\mathbf{H}$	magnetic field strength [A/m]
$\mathbf{H_a}(S')$	tangential magnetic field in a closed surface S' [A/m]
$\overline{\overline{I}}$	unit dyad
$\mathbf{J}, \mathbf{J_s}$	electric current density [A/m^2]
$\mathbf{J_m}, \mathbf{J_{ms}}$	magnetic current density [A/m^2]
$\mathbf{n}$	unit normal vector
$\mathbf{r}$	position vector of the observation point
$\mathbf{r}'$	position vector of the source
$\mathbf{u_r}, \mathbf{u}_\theta, \mathbf{u}_\phi$	unit vectors in spherical coordinate system
$\mathbf{u_x}, \mathbf{u_y}, \mathbf{u_z}$	unit vectors in Cartesian coordinate system

Abbreviations

AUT	antenna under test
CBCPW	conductor-backed co-planar waveguide
CPW	co-planar waveguide
CPA	co-planar patch antenna
DUT	device under test
FFT	fast Fourier transform
GSM	generalized scattering matrix
LC	liquid crystal
MEMS	micro-electro-mechanical systems
MMID	millimeter-wave identification
MVNA	millimeter-wave network analyzer
OEWG	open-ended waveguide
PEC	perfect electric conductor
PMC	perfect magnetic conductor
PNA	programmable network analyzer
PWS	plane-wave spectrum
RA	reflectarray antenna
SLL	side-lobe level
SOLT	short-open-load-trough
SNR	signal-to-noise ratio
TEM	transverse electro-magnetic wave
VNA	vector network analyzer
VTT	Technical Research Centre of Finland

1 Introduction

A reflectarray (RA) is an antenna, which combines certain advantages of phased arrays with the simplicity of a conventional reflector antenna. The main advantage of the spatially fed RAs is that the lossy and complex microstrip feed network used in phased arrays is no longer required. Feeding of the reflectarray can be carried out in number of ways as it is possible to use prime focus- or offset-feed and different types of subreflector feeds, for example Cassegrain-feed, which is commonly used for parabolic reflectors. The incident field from the feed is scattered back to space from the RA elements.

Because of the planar aperture of the reflectarray the re-radiated field will not be in phase due to the path length difference from the different parts of the antenna. In parabolic reflectors, this problem is solved by unique curvature of the dish. However, the path length difference from the spatial feed antenna to each element can be compensated by adding a proper relative phase shift to each individual antenna element. The reason for tuning the antenna elements with phase shifters separately is to produce a collimated, focused, or shaped beam. A collimated beam means that the scattered fields from the RA's elements are phased in such a way that an imaginary aperture plane in the direction of an outgoing scattered wave has a planar phase front [1]. For focused beams, which are used in imaging applications, the scattered field is in phase at a certain point [2]. Shaped or contour beams are mainly used in direct broadcasting satellites, where the coverage of a continent is required with a given minimum gain [3].

The concept of a reflectarray antenna was first introduced by Berry et al. [4] in 1963 and was based on a horn-fed waveguide array. The path length differences were compensated by adjusting the lengths of the open-ended waveguides with shorts at the other end. The real interest for reflectarray antennas was evoked when the microstrip reflectarray was introduced by Malagisi in 1978 [5]. The printed reflectarray antenna consists of a very thin, flat or slightly curved reflecting surface and a spatial feed for illumination. A microstrip reflectarray is a planar or slightly curved reflecting surface composed of relatively simple radiating elements, for example printed dipoles or microstrip patches.

Printed reflectarrays have a few indisputable advantages compared to phased arrays and conventional reflectors. A light planar structure requires less supporting mass and it can also be mounted onto a slightly curved surface, the effect of which can be compensated by adjusting the phase delay of each element. As phased arrays, reflectarrays can also be used for electronic beam scanning by coupling antenna elements with electrically controllable phase-shifters such as *pin*-diodes, liquid crystal (LC) or microelectromechanical systems (MEMS) [5].

Among all capabilities of the reflectarray, it has one major limitation which is the narrow bandwidth. The limitation mainly depends on the bandwidth of the mi-

crostrip patch element, and especially in large reflectarrays, on the differential spatial phase delay of the elements [6]. Narrow bandwidth is characteristic of reflectarrays, which generally cannot exceed more than 10 percent. Therefore the bandwidth performance of the reflectarray is no match to a parabolic reflector with theoretically infinite bandwidth [2].

2 Reflectarray antenna

A reflectarray usually consist of an array of microstrip patches or printed dipoles on the top of a thin dielectric substrate. Individual elements are designed to scatter the incident field from the feed antenna with a proper phase to form a planar phase front in the far field. This chapter consist of general reflectarray theory which includes theoretical modeling and analysis of reflectarrays. At the end of the chapter, there is a description of a 120-GHz reflectarray under development.

2.1 Reflectarray design

The most critical step in the reflectarray design is how the individual elements are fixed to scatter the incident field with a proper phase-shift. The choosing criterion depends on the desired polarization, bandwidth and ability to provide electronic beam steering, which requires reconfigurable phase shifters. Element selection can be separated by the technique of producing relative phase. One method is to use identical elements and to induce a phase shift by either rotating the element (a good method for circular polarization) or alternatively attaching a variable length transmission line stub into the element. One weakness with this approach is that the phase shift is induced with a conventional microstrip transmission line, the upper frequency of which is bounded due to stiff manufacturing tolerances and dispersion.

A good approach for static designs is to use rectangular patches or printed dipoles of variable size. It is suitable for linear, dual and circular polarization and compared with stub-tuned ones, it gives more freedom for beam forming, larger bandwidth [7] and lower cross-polarization. Because of its good ability to form a contour beam, the variable-size patch reflectarray is very suitable for direct broadcasting satellites where a good coverage of a continent is desired [2]. The drawbacks of the use of variable sized elements are the limited ability to cover a wide phase range, the raised side-lobe level (SLL) caused by non-uniform edge-to-edge element spacing [8], and mutual coupling between cells especially with physically large adjacent elements [2]. Also, it is hard to implement a reconfigurable phase shifter, which changes the size of the element, especially at high frequencies. However, both methods are based on the same principle of inducing a small shift to the resonant frequency of the element which has an effect on changing the phase of the reflected field [7].

The reflectarray cell can be designed as an individual element based on the use of design curves related to the phase of the re-radiated field. A design curve is determined by changing a certain geometrical parameter, in this case, the length of the attached stub and assuming a normal incidence. This approach assumes that the influence of the angle of incidence is negligible to the phase response of the element. The assumption is only valid for the central elements of the reflectarray with reasonably large F/D-ratios [2]. However, as the largest part of the illuminated power is reflected from the central part of the reflectarray, the normal incidence approximation can provide a good prediction for small angles of incidence [2].

It was stated in [9], that the phase response of the element does not differ greatly until the angle of incidence approaches 40°. In offset feed configurations, which are normally used to avoid the feed shadow effect, the angles of incidence for the outermost elements are the order of 40° and larger. Thus, the angle of incidence must be considered in the design. An array cell can be analyzed as an isolated element, which is commonly used in reflectarrays with attached stubs or in an array environment by using an infinite array approach. It is stated in [10] that when the distance between the edges of the adjacent patches is greater than one quarter of a wavelength in the dielectric, the mutual coupling between the neighboring elements can be neglected.

The concept of the reflectarray gives a great amount of flexibility for the selection of the feed topology. As in parabolic reflectors, a prime-focus or Cassegrein feed can be used. Also, an offset feed can be used to prevent the feed antenna from obscuring the main beam and thus expand the visible region of the antenna.

2.1.1 Element spacing

All elements of the reflectarray must have a proper spacing between adjacent elements in order to avoid grating lobes entering the visible region [2]. Generally the center-to-center spacing of the elements should not exceed the limit of $\frac{\lambda_0}{2}$. However, especially in reconfigurable reflectarrays this limit is often too strict due to space allocated for the phase-shifter. Grating lobes enter the visible region if the condition in Eq. (2.1) is violated [11]:

$$\frac{d}{\lambda_0} \leq \frac{1}{1+\sin\theta_0}, \tag{2.1}$$

where d is the element spacing, λ_0 is the free-space wavelength and θ_0 is either the incident angle from the feed or the main beam tilt angle, whichever is larger [2]. The grating lobes can be avoided by limiting the maximum main beam tilt angle. If the element spacing is determined improperly, distributed grating lobes, which are difficult to observe in the beam patterns, are formed due the varying incident on the different parts of the reflectarray [2]. Especially offset-fed designs, in which the element spacing exceeds $0.5\lambda_0$, are more prone to the distributed grating lobe generation. Generally, the problem can be minimized with a reasonably large $\frac{f}{D}$ ratio.

2.1.2 Calculation of the desired relative phase-shift

In order to convert the spherical wave radiated from the feed horn antenna into a focused, collimated or shaped beam, the reflected field from each element must induce a proper phase shift to the incident field. To produce a collimated beam in the direction (θ_b, φ_b), where θ_b and φ_b are represented in spherical coordinates shown in Fig. 2.1, a progressive phase-shift distribution of $\phi(x_i, y_i)$ must be acquired. It

can be calculated with

$$\phi(x_i, y_i) = -k_0 \sin\theta_b \cos\varphi_b x_i - k_0 \sin\theta_b \sin\varphi_b y_i, \tag{2.2}$$

where $k_0 = \frac{2\pi}{\lambda}$ is the free-space wave number and (x_i, y_i) are the coordinates of the element (in respect of the central element of the antenna)[2]. Eq. (2.2) is known from the conventional array theory, but in case of reflectarrays also the spatial path difference ϕ_s from the feed to individual elements must be taken in account with Eq. (2.3).

$$\phi_s(x_i, y_i) = -k_0|\mathbf{d_i}| + \phi_R(x_i, y_i), \tag{2.3}$$

where $\mathbf{d_i}$ is a vector from the phase center of the feed to the i:th element and ϕ_R is the required phase shift for each element which can be calculated from Eqs. (2.2) and (2.3):

$$\phi_R(x_i, y_i) = k_0(|\mathbf{d_i}| - (x_i \cos\varphi_b + y_i \sin\varphi_b)\sin\theta_b). \tag{2.4}$$

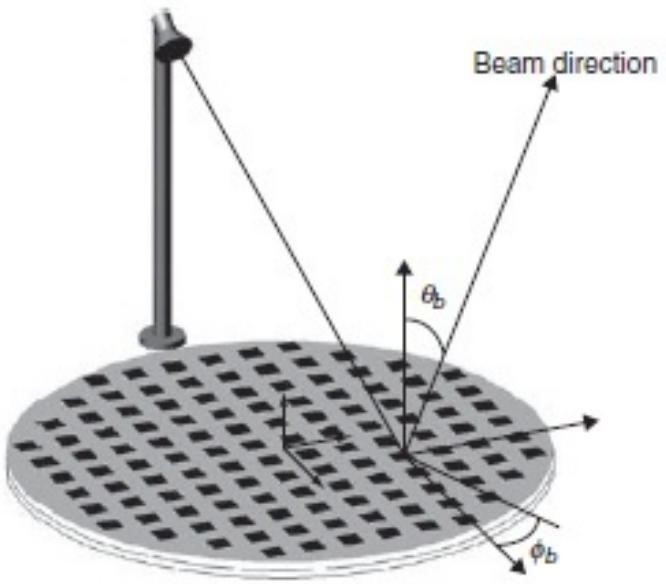

Figure 2.1: Spherical coordinate system of the reflectarray [2].

However, our RA is slightly different since its operation principle resembles that of an elliptic reflector in optical terms, and instead of a collimated beam, it produces a focused one to a finite distance d_2. Now, not only the direction of the beam is important but also the distance must be taken into account. Hence, it is more convenient to use Cartesian coordinate system instead of the spherical one used above. For a focused beam, Eq. (2.4) simplifies to a more convenient form for an imaging application [12]:

$$\phi_R(mod 2\pi) = C - k_0(|\mathbf{d_i}| + |\mathbf{d_i'}|), \tag{2.5}$$

where $\mathbf{d_i}$, as it was in the previous case, is a vector from the phase center of the feed to the i:th element and $\mathbf{d_i'}$ is, respectively, a vector pointing from i:th element

to the desired focus point. C is an arbitrary phase constant, in place of which can be used a reference phase shift caused by the path from feed to focus through the central element of the RA.

2.2 Reflectarray antenna analysis

The analysis of RA's ability to produce a collimated, focused or shaped beam is quite straightforward when using a unit cell approach with suitable boundary conditions. Reflectarray is considered to be in a transmitting mode and the feed antenna is located far enough from the RA, so that the incident field at each element can be locally acknowledged as a plane wave with a phase proportional to the distance from the phase center of the feed. It corresponds to a spherical wave propagation from the feed to the RA [2].

The analysis of the reflectarray, like every other antenna, is based on Maxwell's equations:

$$\nabla \times \mathbf{E} = -j\omega\mu\mathbf{H} - \mathbf{J_m}, \tag{2.6}$$

$$\nabla \times \mathbf{H} = j\omega\mu\epsilon\mathbf{E} + \mathbf{J}, \tag{2.7}$$

where electric and magnetic current densities $\mathbf{J}$ and $\mathbf{J_m}$ are sources of electric and magnetic fields $\mathbf{E}$ and $\mathbf{H}$.

If equivalent sources at the surface S are known, the field outside the surface can be calculated with Green's dyad:

$$\overline{\overline{G}}(\mathbf{r}-\mathbf{r}') = (\overline{\overline{I}} + \frac{1}{k^2}\nabla\nabla)G(\mathbf{r}-\mathbf{r}'), \tag{2.8}$$

where $\overline{\overline{I}}$ is an unit dyad, k is the wave number, $\mathbf{r}$ is the position vector of the field, $\mathbf{r}'$ is the source position vector and

$$G(\mathbf{r}-\mathbf{r}') = \frac{e^{-jk|\mathbf{r}-\mathbf{r}'|}}{4\pi|\mathbf{r}-\mathbf{r}'|}, |\mathbf{r}-\mathbf{r}'| = \sqrt{(\mathbf{r}-\mathbf{r}')\cdot(\mathbf{r}-\mathbf{r}')}, \tag{2.9}$$

is a scalar Green's function which satisfies the Helmholtz equation:

$$\nabla^2 G(\mathbf{r}-\mathbf{r}') + k^2 G(\mathbf{r}-\mathbf{r}') = -\delta(\mathbf{r}-\mathbf{r}'). \tag{2.10}$$

The electric current of the source $\mathbf{J}$ at different points $\mathbf{r}'$ in space produces an electric field to the point $\mathbf{r}$ which can be represented in a vector form (dot product of a dyad and a vector produces a vector) [13]:

$$\mathbf{E}(\mathbf{r}) = -j\omega\mu \int_V \overline{\overline{G}}(\mathbf{r}-\mathbf{r}')\cdot\mathbf{J}(\mathbf{r}')dV'. \tag{2.11}$$

Magnetic field can be calculated by placing Eq. (2.11) to Maxwell's equation (2.6) in a form:

$$\mathbf{H}(\mathbf{r}) = \int_V [\nabla \times \overline{\overline{G}}(\mathbf{r}-\mathbf{r}')] \times \mathbf{J}(\mathbf{r}')dV' = \int_V [\nabla G(\mathbf{r}-\mathbf{r}')] \times \mathbf{J}(\mathbf{r}')dV'. \tag{2.12}$$

Respectively, fields produced by magnetic current $\mathbf{J_m}$ are:

$$\mathbf{H}(\mathbf{r}) = -j\omega\epsilon \int_V \overline{\overline{G}}(\mathbf{r}-\mathbf{r}') \cdot \mathbf{J_m}(\mathbf{r}')dV', \tag{2.13}$$

$$\mathbf{E}(\mathbf{r}) = \int_V [\nabla \times \overline{\overline{G}}(\mathbf{r}-\mathbf{r}')] \times \mathbf{J_m}(\mathbf{r}')dV' = -\int_V [\nabla G(\mathbf{r}-\mathbf{r}')] \times \mathbf{J_m}(\mathbf{r}')dV'. \tag{2.14}$$

2.2.1 Huygens' principle

Huygens' principle is an important tool in electromagnetics for solving complex boundary problems by transforming it to a form which is easier to handle. It states that each point on a primary wave front can be considered a new source of a secondary spherical wave [14]. According to Huygens' principle, sources inside a volume V bounded by the closed surface S can be replaced with equivalent sources $\mathbf{J_s}$ and $\mathbf{J_{ms}}$ which depends on electric and magnetic fields at the surface S as follows:

$$\mathbf{J_s} = \mathbf{n} \times \mathbf{H}(S), \tag{2.15}$$

$$\mathbf{J_{ms}} = \mathbf{E}(S) \times \mathbf{n}, \tag{2.16}$$

where $\mathbf{E}(S)$ and $\mathbf{H}(S)$ are tangential electric and magnetic fields on the surface S and $\mathbf{n}$ is a unit vector normal to the surface. The principle can be used, when the space outside the surface S is homogeneous [13]. Thus the original problem can be replaced by an equivalent source, which produces fields $\mathbf{E}(\mathbf{r})$ and $\mathbf{H}(\mathbf{r})$ outside the surface S. The field inside the surface S equals to zero since $\mathbf{J_s}$ cancels out the field produced by $\mathbf{J_{ms}}$. Therefore this volume can be filled with an arbitrary medium without affecting fields outside S. Huygens' principle is closely linked to Love's equivalence principle [15], which is very useful for analyzing aperture-type antennas.

There are four types of equivalent boundary problems where each one gives the same result outside the surface S [13]:

1. Original sources and antenna structures inside S.
2. Equivalent sources $\mathbf{J_s}$ and $\mathbf{J_{ms}}$ in the surface S, air inside.
3. Equivalent source $2\mathbf{J_{ms}}$ on the surface S, the inside of which is filled with perfect electric conductor (PEC) thus the equivalent source $\mathbf{J_s}$ can be ignored.
4. Equivalent source $2\mathbf{J_s}$ on the surface S, the inside of which is filled with perfect magnetic conductor (PMC) thus the equivalent source $\mathbf{J_{ms}}$ can be ignored.

If equivalent sources are known, the second problem is just an integral assignment. Instead, items 1, 3 and 4 are boundary problems. It is only worth changing the boundary problem 2 to another one, 3 or 4, if the new one is more straightforward to solve. That is the case if S is a plane and even then the surface is closed through infinity, which makes Huygens' principle still valid. The mirror principle can be used for solving boundary problems of electric and magnetic conductors. An electro-conductive half-space can be replaced with a mirror of the magnetic current source, and magnetic conductive with a mirror of the electric current source, respectively. In that case, as a source there is only either $2\mathbf{J_{ms}}$ or $2\mathbf{J_s}$ and the fields outside S can be calculated with the approximate knowledge of only one field, $\mathbf{E}$ of $\mathbf{H}$ at the surface. Which representation to use depends on the case. For example, the representation 3 is suitable in the case of microstrip patches and can be applied by filling the other half-space with PEC.

The electric and magnetic field produced by equivalent current sources $\mathbf{J_s}$ and $\mathbf{J_{ms}}$ outside S can be expressed in an integral form as follows. When comparing these to the case of a point source described with Eqs. (2.11)-(2.14), despite the use of equivalent current sources, the integral of a volume is now replaced by a closed surface integral:

$$\mathbf{E}(\mathbf{r}) = -j\omega\mu \oint_S \overline{\overline{G}}(\mathbf{r}-\mathbf{r}') \cdot \mathbf{J_s}(\mathbf{r}')dS', \tag{2.17}$$

$$\mathbf{H}(\mathbf{r}) = \oint_S [\nabla G(\mathbf{r}-\mathbf{r}')] \times \mathbf{J_s}(\mathbf{r}')dS', \tag{2.18}$$

$$\mathbf{E}(\mathbf{r}) = -\oint_S [\nabla G(\mathbf{r}-\mathbf{r}')] \times \mathbf{J_{ms}}(\mathbf{r}')dS', \tag{2.19}$$

$$\mathbf{H}(\mathbf{r}) = -j\omega\epsilon \oint_S \overline{\overline{G}}(\mathbf{r}-\mathbf{r}') \cdot \mathbf{J_{ms}}(\mathbf{r}')dS'. \tag{2.20}$$

In most cases we are only interested on the far-field properties to obtain the radiation pattern of the antenna. Far-fields produced by equivalent sources can be determined by using Green's function far-field approximation:

$$G(\mathbf{r}-\mathbf{r}') \approx \frac{e^{-jkr}}{4\pi r} e^{jk\mathbf{u_r}\cdot\mathbf{r}'}, \tag{2.21}$$

and when using $\nabla \approx jk\mathbf{u_r}$, field equations (2.14)-(2.20) can be written in a simplified form as follows [16].

The effect of electric surface current density is found from the magnetic vector potential

$$\mathbf{A} = \frac{e^{-jkr}}{4\pi r} \iint_S \mathbf{J_s}(\mathbf{r}') e^{jk\mathbf{u_r}\cdot\mathbf{r}'} dS', \tag{2.22}$$

and by duality, the electric vector potential

$$\mathbf{F} = \frac{e^{-jkr}}{4\pi r} \iint_S \mathbf{J_{ms}}(\mathbf{r}') e^{jk\mathbf{u_r}\cdot\mathbf{r}'} dS', \tag{2.23}$$

which is related to the magnetic current density.

The far-fields produced by electric and magnetic vector potentials are:

$$\mathbf{E_A} = -j\omega\mu\mathbf{A}[\frac{Vs}{Am}], \tag{2.24}$$

$$\mathbf{H_F} = -j\omega\epsilon\mathbf{F}[\frac{Vs}{Am}]. \tag{2.25}$$

However, Eqs. (2.22) and (2.23) include only the transversal (in respect to $\mathbf{u_r}$) components. The electric field associated with $\mathbf{H_F}$ is found from a transverse electromagnetic wave (TEM) relationship

$$\mathbf{E_F}(\mathbf{r}) = \eta\mathbf{H_F}(\mathbf{r}) \times \mathbf{u_r}, \tag{2.26}$$

and the magnetic field associated with $\mathbf{E_A}$, from the relation of

$$\mathbf{H_A}(\mathbf{r}) = \frac{\mathbf{u_r} \times \mathbf{E_A}(\mathbf{r})}{\eta}, \tag{2.27}$$

respectively. The total electric and magnetic field in the far-field induced by the equivalent current sources $\mathbf{J_s}$ and $\mathbf{J_{ms}}$ can be now written as:

$$\mathbf{E}(\mathbf{r}) = \mathbf{E_A} + \mathbf{E_F} = -j\omega\mu\mathbf{A} - j\omega\eta\epsilon\mathbf{F} \times \mathbf{u_r}, \tag{2.28}$$

$$\mathbf{H}(\mathbf{r}) = \mathbf{H_F} + \mathbf{H_A} = -j\omega\epsilon\mathbf{F} - \frac{\mathbf{u_r} \times j\omega\mu\mathbf{A}}{\eta}. \tag{2.29}$$

Equations (2.28) and (2.29) are now dependent on both electric and magnetic current densities. However, since the equivalent current sources were determined by using zero fields for $z < 0$, the left half space can be replaced by PMC or PEC and using image currents ($2\mathbf{J_S}$ and $2\mathbf{J_{MS}}$) as mentioned at the beginning of this Section. Thus, when the material from the negative half-space is removed and respective equivalent current source is doubled due to image current, fields in the positive half-space remain unchanged and, hence, the Huygens' principle is still valid.

Magnetic vector potential for the case of the left half-space filled with PEC is

$$\mathbf{A} = \frac{e^{-jkr}}{4\pi r} \iint_S 2\mathbf{J_s}(\mathbf{r}') e^{jk\mathbf{u_r}\cdot\mathbf{r}'} dS', \tag{2.30}$$

and in a similar way, the electric vector potential for the PMC case:

$$\mathbf{F} = \frac{e^{-jkr}}{4\pi r} \iint_S 2\mathbf{J_{ms}}(\mathbf{r}') e^{jk\mathbf{u_r}\cdot\mathbf{r}'} dS'. \tag{2.31}$$

Electric and magnetic fields are now dependent on only one equivalent surface current density, either $\mathbf{J_s}$ or $\mathbf{J_{ms}}$:

$$\mathbf{E} = -j\omega\mu A_\theta \mathbf{u}_\theta - j\omega\mu A_\phi \mathbf{u}_\phi, \tag{2.32}$$

$$\mathbf{H} = -j\omega\epsilon F_\theta \mathbf{u}_\theta - j\omega\epsilon F_\phi \mathbf{u}_\phi, \tag{2.33}$$

where one can be calculated from the other one by using Eqs. (2.26) and (2.27).

2.2.2 Fourier transform in planar antenna problems

Fourier transform is a convenient tool for problems which are determined by differential equations such as spectroscopy, signal processing and quantum mechanics. A discrete version of this linear and invertible operation can be rapidly computed with fast Fourier transform (FFT) algorithms. In computational electro-magnetics and especially with antenna problems, FFT can be used to evaluate the radiation patterns for aperture-type antennas. The other useful application is FFT-based near- to far-field transform in antenna measurements. Planar near-field measurement range is often required when the minimum distance for the assumption of far-field conditions is impractical to satisfy. This is usually the case with large aperture millimeter-wave antennas. The relation between the aperture distribution and produced far-field pattern can be described with 2-dimensional Fourier transform as follows [14]:

$$E(x,y,z) = \frac{1}{(2\pi)^2} \int_{-\infty}^{\infty} \int_{-\infty}^{\infty} \mathbf{A}(k_x,k_y) e^{j\mathbf{k}\cdot\mathbf{r}'} dk_x dk_y, \tag{2.34}$$

where $\mathbf{k} = k_x\mathbf{u_x} + k_y\mathbf{u_y} + k_z\mathbf{u_z}$ represents spatial propagation constants in Cartesian coordinates and is related to the free-space wave number as:

$$k_0 = \frac{2\pi}{\lambda_0} = \sqrt{k_x^2 + k_y^2 + k_z^2}. \tag{2.35}$$

Thus,

$$\mathbf{k}\cdot\mathbf{r}' = (k_x\mathbf{u_x} + k_y\mathbf{u_y} + k_z\mathbf{u_z}) \cdot (x'\mathbf{u_x} + y'\mathbf{u_y} + z'\mathbf{u_z}) = k_x x' + k_y y' + k_z z'. \tag{2.36}$$

$\mathbf{A}(k_x,k_y)$ denotes a plane-wave spectrum (PWS) of the radiated field, which is discussed further in detail in Section 4.1.

$$\mathbf{A}(k_x,k_y) = \mathbf{A_T}(k_x,k_y) + A_z(k_x,k_y)\mathbf{u_z}, \tag{2.37}$$

where

$$A_z(k_x,k_y) = \frac{\mathbf{k}\cdot\mathbf{A_T}(k_x,k_y)}{k_z}, \tag{2.38}$$

and

$$\mathbf{A_T}(k_x,k_y) = A_x(k_x,k_y)\mathbf{u_x} + A_y(k_x,k_y)\mathbf{u_y} = \iint_{S_a} \mathbf{E}_a(x,y) e^{j(k_x x' + k_y y')} dxdy, \tag{2.39}$$

which is the two dimensional Fourier transform of the aperture field.

2.2.3 Physical optics approximation

So far, there is no approximation used and equations (2.17) - (2.20) give the exact field outside S at positive half space, as far as exact fields in equations (2.15) and (2.16) are known. However, the exact knowledge of the fields over the entire surface S are known only in rare cases and generally some approximation is needed. One popular approach is the physical optics approximation, where the tangential fields $\mathbf{E_a}$ and $\mathbf{H_a}$ have non-zero values only in a small proportion S_a of the infinite plane S [16]. S_a usually corresponds with the physical aperture of the antenna.

New equivalent surface currents can be written as:

$$\mathbf{J_s} = \mathbf{n} \times \mathbf{H_a}, \tag{2.40}$$

$$\mathbf{J_{ms}} = \mathbf{E_a} \times \mathbf{n}, \tag{2.41}$$

on S_a and zero elsewhere.

By using Eqs. (2.40) and (2.40), radiation vectors (2.22) and (2.23) can be written as:

$$\mathbf{A} = \frac{e^{-jkr}}{4\pi r}\mathbf{n} \times \iint\limits_{S_a} \mathbf{H_a} e^{j\mathbf{k}\cdot\mathbf{r}'} dS'_a, \tag{2.42}$$

$$\mathbf{F} = -\frac{e^{-jkr}}{4\pi r}\mathbf{n} \times \iint\limits_{S_a} \mathbf{E_a} e^{j\mathbf{k}\cdot\mathbf{r}'} dS'_a. \tag{2.43}$$

The integral in each of equations above is a two dimensional Fourier transform of the aperture field like in Eq. (2.39):

$$\boldsymbol{f}(\theta,\phi) = \iint\limits_{S_a} \mathbf{E_a} e^{j\mathbf{k}\cdot\mathbf{r}'} dS'_a = \iint\limits_{S_a} \mathbf{E_a}(x',y') e^{j(k_x x' + k_y y')} dx'dy', \tag{2.44}$$

$$\boldsymbol{g}(\theta,\phi) = \iint\limits_{S_a} \mathbf{H_a} e^{j\mathbf{k}\cdot\mathbf{r}'} dS'_a = \iint\limits_{S_a} \mathbf{H_a}(x',y') e^{j(k_x x' + k_y y')} dx'dy', \tag{2.45}$$

where $k_x = k\cos\phi\sin\theta$ and $k_y = k\sin\phi\sin\theta$. Both E_a and H_a lie on the xy-plane, thus $\mathbf{n} = \mathbf{u_z}$ and radiation vectors become:

$$\mathbf{A} = \frac{e^{-jkr}}{4\pi r}\mathbf{u_z} \times \boldsymbol{g}(\theta,\phi), \tag{2.46}$$

$$\mathbf{F} = -\frac{e^{-jkr}}{4\pi r}\mathbf{u_z} \times \boldsymbol{f}(\theta,\phi). \tag{2.47}$$

Because E_a and H_a are tangential to the aperture plane, they can be expressed in Cartesian coordinates as $\mathbf{E_a} = E_{ax}\mathbf{u_x} + E_{ay}\mathbf{u_y}$. In a similar manner quantities $\boldsymbol{f}$ and $\boldsymbol{g}$ are resolved as $f_x\mathbf{u_x} + f_y\mathbf{u_y}$ and $g_x\mathbf{u_x} + g_y\mathbf{u_y}$. Hence,

$$\mathbf{A} = \frac{e^{-jkr}}{4\pi r}\mathbf{u_z} \times (g_x\mathbf{u_x} + g_y\mathbf{u_y}) = \frac{e^{-jkr}}{4\pi r}(g_x\mathbf{u_y} - g_y\mathbf{u_x}), \tag{2.48}$$

$$\mathbf{F} = -\frac{e^{-jkr}}{4\pi r}\mathbf{u_z} \times (f_x\mathbf{u_x} + f_y\mathbf{u_y}) = \frac{e^{-jkr}}{4\pi r}(f_y\mathbf{u_x} - f_x\mathbf{u_y}). \tag{2.49}$$

The polar components of the radiation vectors can be determined with a dot product by using following identities:

$$\mathbf{u}_\theta = \cos\phi\mathbf{u_x} + \sin\phi\cos\theta\mathbf{u_y} - \sin\theta\mathbf{u_z}, \tag{2.50}$$

$$\mathbf{u}_\phi = -\sin\phi\mathbf{u_x} + \cos\phi\mathbf{u_y}. \tag{2.51}$$

Thus,

$$A_\theta = \mathbf{u}_\theta \cdot \mathbf{A} = -\frac{e^{-jkr}}{4\pi r}\cos\theta(g_y\cos\phi - g_x\sin\phi), \tag{2.52}$$

$$A_\phi = \mathbf{u}_\phi \cdot \mathbf{A} = \frac{e^{-jkr}}{4\pi r}(g_x\cos\phi + g_y\sin\phi), \tag{2.53}$$

$$F_\theta = \mathbf{u}_\theta \cdot \mathbf{F} = \frac{e^{-jkr}}{4\pi r}\cos\theta(f_y\cos\phi - f_x\sin\phi), \tag{2.54}$$

$$F_\phi = \mathbf{u}_\phi \cdot \mathbf{F} = -\frac{e^{-jkr}}{4\pi r}(f_x\cos\phi + f_y\sin\phi). \tag{2.55}$$

The electric field can be now calculated by introducing Eqs. (2.52)-(2.55) in Eq. (2.28):

$$E_\theta = jk\frac{e^{-jkr}}{4\pi r}[(f_x\cos\phi + f_y\sin\phi) + \eta\cos\theta(g_y\cos\phi - g_x\sin\phi)], \tag{2.56}$$

$$E_\phi = jk\frac{e^{-jkr}}{4\pi r}[\cos\theta(f_y\cos\phi - f_x\sin\phi) - \eta(g_x\cos\phi + g_y\sin\phi)]. \tag{2.57}$$

For the other two equivalent systems, the components of the electric field are solved by removing either g- or f-terms and doubling the remaining ones. In the case of PEC, we have:

$$E_\theta = jk\frac{e^{-jkr}}{2\pi r}[f_x\cos\phi + f_y\sin\phi], \tag{2.58}$$

$$E_\phi = jk\frac{e^{-jkr}}{2\pi r}[\cos\theta(f_y\cos\phi - f_x\sin\phi)], \tag{2.59}$$

and in a similar way for the PMC case:

$$E_\theta = jk\frac{e^{-jkr}}{2\pi r}[\eta\cos\theta(g_y\cos\phi - g_x\sin\phi)], \tag{2.60}$$

$$E_\phi = -jk\frac{e^{-jkr}}{2\pi r}[\eta(g_x\cos\phi + g_y\sin\phi)]. \tag{2.61}$$

Alternatively, the radiation fields can be calculated by placing Eqs. (2.52)-(2.55) by Eq. (2.33) (PEC) or Eq. (2.32) (PMC), which gives the same result. In all the three cases the components of the radiating magnetic field can be calculated from relations:

$$H_\theta = -\frac{E_\phi}{\eta}, \tag{2.62}$$

$$H_\phi = \frac{E_\theta}{\eta}. \tag{2.63}$$

2.2.4 Radiation pattern calculation

Once the reflectarray unit cells have been fully characterized, the radiation pattern produced by these elements can be evaluated. There are various approaches presented in the literature which differ in terms of how the polarization is taken into account and how many Floquet harmonics are used. One connective feature of all approaches is to form a generalized scattering matrix (GSM) to describe how the incident field scatters from the RA elements. It is usually divided into two parts, where the first one illustrates the reflected field from the ground plane and dielectric substrate and the second one represents the field scattered from the antenna elements. Multilayer structures can be analyzed with a cascade process by generating GSM for each layer separately [2].

Before the scattered field can be calculated, the incident field on each reflectarray element must be known. It is determined by the position and the radiation pattern of the feed. A horn antenna is commonly used as the feed for reflectarray and its radiation pattern can be expressed with $\cos^q(\theta)$ function. A generalized model for an y-polarized feed can be expressed with as:

$$\mathbf{E_f}(\theta,\phi) = jk\frac{e^{-jkr}}{2\pi r}[\mathbf{u}_\theta C_E(\theta)\sin\phi + \mathbf{u}_\phi C_H(\theta)\cos\phi], \tag{2.64}$$

where C_E and C_H are defined as a power of q. The spherical coordinate system used for the feed points ($\mathbf{u_r}$) from the phase center of the feed to the center of the RA. The field radiated from the feed horn to the central point of each RA cell can be determined from (2.64). Then, this field is transformed to a Cartesian coordinate system of the reflectarray, where the RA lies in the xy-plane and the z-axis points to the antenna's boresight direction. The field can be transformed into Cartesian components by the expression:

$$\begin{pmatrix} f_r \\ f_\theta \\ f_\phi \end{pmatrix} = \begin{pmatrix} \sin\theta\cos\phi & \sin\theta\sin\phi & \cos\theta \\ \cos\theta\cos\phi & \cos\theta\sin\phi & -\sin\phi \\ -\sin\phi & \cos\phi & 0 \end{pmatrix} \begin{pmatrix} f_x \\ f_y \\ f_z \end{pmatrix}. \tag{2.65}$$

Since parameters θ and ϕ changes with the position of the element, the transformation must be evaluated for each RA element separately.

The application of the reflectarray under development is an imaging radar, where the use of a Gaussian beam distribution is more convenient than general cos^q beam distribution used here. Thus instead of (2.64), a fundamental Gaussian beam mode (2.66) is used as a feed model.

$$\mathbf{E_f}(\mathbf{r}') = \frac{w_0}{w(r')} e^{\frac{-r(r')^2}{w(r')^2}} e^{-jkz} e^{\frac{-j\pi r(r')^2}{\lambda R(z)}} e^{j\phi_0}, \tag{2.66}$$

where w_0 and $w(z)$ are the beam waist and beam radius, $r(r') = \sqrt{x'^2 + y'^2}$ is the distance from the axis of propagation and $\phi_0 = \arctan\frac{\lambda z}{\pi w_o^2}$ is the Gaussian beam

phase shift. Constant phase surfaces of the Gaussian beam are surfaces of a sphere, the radius of curvature of which are:

$$R(z) = z\left[1 + \left(\frac{\pi w_0^2}{\lambda z}\right)\right]. \tag{2.67}$$

Gaussian beam is rotationally symmetrical and its transversal plane amplitude distribution is Gaussian in such a way that the $\frac{1}{e}$-part of the amplitude maximum is at a distance of the beam radius w from the axis of propagation.

Once the tangential electric field on the reflectarray elements has been determined, the electric field outside the reflectarray aperture can be calculated with (2.19), where the surface current

$$\mathbf{J_{ms}}(\mathbf{r}') = -2\mathbf{n} \times \Gamma_e(\mathbf{r}')E_f(\mathbf{r}')\mathbf{u_y} \tag{2.68}$$

depends on the feeding field and $\Gamma_e(\mathbf{r}')$, which is the reflection coefficient of the element. The normal vector $\mathbf{n}$ points to $\mathbf{u_z}$ direction in RA coordinate system. Since the RA can also be focused onto the near-field region, the far-field approximation (2.21) of the scalar Green's function (2.9) does not give exact results of the fields close to the antenna aperture. The gradient of the scalar Green's function becomes [17]

$$\nabla G(\mathbf{r} - \mathbf{r}') = \left(\frac{1}{|\mathbf{r} - \mathbf{r}'|} - jk\right)\frac{e^{-jk|\mathbf{r}-\mathbf{r}'|}}{4\pi|\mathbf{r} - \mathbf{r}'|}\mathbf{u_r}, \tag{2.69}$$

where $\mathbf{u_r} = \frac{(\mathbf{r}-\mathbf{r}')}{|\mathbf{r}-\mathbf{r}'|}$. The electric field outside the reflectarray (2.19) becomes

$$\mathbf{E}(\mathbf{r}) = \oint_S \left(\frac{1}{|\mathbf{r} - \mathbf{r}'|} - jk\right)\frac{e^{-jk|\mathbf{r}-\mathbf{r}'|}}{4\pi|\mathbf{r} - \mathbf{r}'|}\mathbf{u_r} \times 2\mathbf{u_z} \times \Gamma_e(\mathbf{r}')E_f(\mathbf{r}')\mathbf{u_y}dS'. \tag{2.70}$$

The radial unit vector $\mathbf{u_r}$ can be transformed to Cartesian coordinates with (2.65):

$$\mathbf{u_r} = \sin\theta\cos\phi\mathbf{u_x} + \sin\theta\sin\phi\mathbf{u_y} + \cos\theta\mathbf{u_z}, \tag{2.71}$$

which can be written in a form:

$$\mathbf{u_r} = \frac{x - x'}{|\mathbf{r} - \mathbf{r}'|}\mathbf{u_x} + \frac{y - y'}{|\mathbf{r} - \mathbf{r}'|}\mathbf{u_y} + \frac{z - z'}{|\mathbf{r} - \mathbf{r}'|}\mathbf{u_z}, \tag{2.72}$$

where the dotted coordinates are in a plane of the RA surface. The electric field outside the RA (2.70) can be now written in a Cartesian form:

$$\mathbf{E}(\mathbf{r}) = \oint_S \Gamma_e(\mathbf{r}')E_f(\mathbf{r}')\frac{1 - jk|\mathbf{r} - \mathbf{r}'|}{2\pi|\mathbf{r} - \mathbf{r}'|^3}e^{-jk|\mathbf{r}-\mathbf{r}'|}\left[(y - y')\mathbf{u_y} - (z - z')\mathbf{u_z}\right]dS'. \tag{2.73}$$

2.3 A 120-GHz reconfigurable reflectarray antenna for radar application

A reconfigurable 120-GHz reflectarray antenna is being developed at Aalto University Department of Radio Science and Engineering and at Technical Research Centre of Finland (VTT). The reflectarray will consist of approximately 3700 microstrip-based antenna elements similar to the coplanar patch antenna (CPA) presented in [18]. Antenna elements will be coupled with MEMS phase shifters, which can be individually controlled to create the desired beam. The element spacing is 2 mm, which allows beam steering up to 38 degrees from normal before grating lobes enter the visible area [19].

The state of the MEMS phase shifters can be rapidly changed, which makes real-time scanning for video imaging applications or millimeter-wave identification (MMID) possible. For electronic beam steering also *pin*-diodes are used for antenna element tuning but they are considered to be too lossy due to high series resistance of the diode and can not be used at the upper millimeter-wave frequency range [20]. Another promising technique for beam steering in millimeter-wave reflectarrays is liquid crystal where the permittivity of the substrate can be varied with an applied bias voltage. However, the time constant of the variation can be too long for an imaging application [21].

The reflectarray is designed to be illuminated with Gaussian beam which is created by a corrugated horn antenna. Offset configuration is used to avoid feed shadow effect. The feed structure is located at a position of ($x = 150$ mm, $y = 0$, $z = 300$ mm), when the origin is at the center of the reflectarray. A corrugated horn antenna has good electrical characteristics for Gaussian beam forming. It produces an extremely circularly symmetric beam which has low side-lobe- and cross-polarization levels although the antenna has a considerably wide bandwidth.

A computation of the required relative phase shift for each element is done with physical optics based simulations optimized with a genetic algorithm (GA) developed in VTT. GA is a stochastic multiple agent optimization procedure which is based on natural selection and genetic pressure. As GAs are typically used for binary problems, it is a convenient tool for discrete phase distribution optimization of the RA. Fig. 2.2 shows the calculated relative phase shift for the boresight-focused (to 3 m) reflectarray.

The design goal of the reflectarray proposed here is to develop a millimeter-wave radar for imaging and identification applications. The radar operates at the near-field region at the distance of a few meters. The phase pattern of the reflectarray is optimized to each focusing distance separately to obtain a sufficient resolution and to get a strong reflection back from the target.

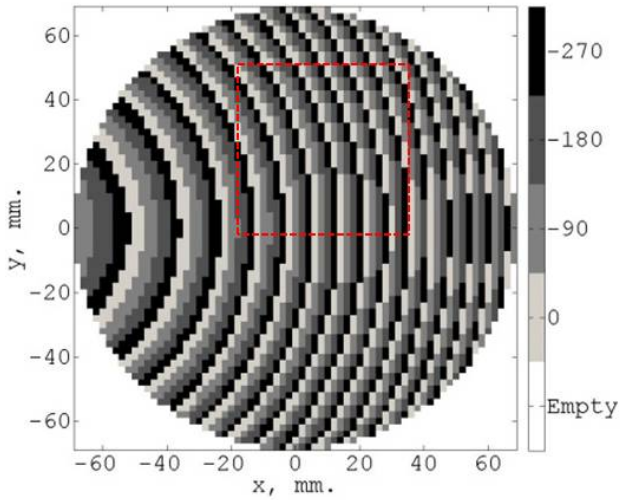

Figure 2.2: Relative phase shift of the static reflectarray (focused to 3 m, 50 cm aside) [19]. The red rectangle represents an area of 25×25 elements which is chosen to be characterized with a near-field measurement method presented in Section 3.2.

2.3.1 Coplanar patch antenna

The selection of an antenna topology is crucial to accomplish sufficient performance requirements such as bandwidth, directivity, beam width, side-lobe level (SLL), polarization, and when electronic beam steering is desired, the antenna must be suitable for reconfigurability. The bandwidth of a microstrip RA is mainly bounded by the bandwidth of a single element and the spatial phase delay [6].

Despite the fact that a conventional rectangular microstrip patch antenna would be the best solution in all its simplicity, the implementation of the reconfigurable MEMS phase shifter makes the structure more complicated since it also needs the ground signal in addition to biasing voltage. For the sake of such a high central frequency of the antenna, 120 GHz, the manufacturing capabilities must be considered.

A coplanar patch antenna (CPA) introduced in [18] is a combination of a conventional microstrip patch antenna and a loop slot antenna. The concept of CPA is well compatible for the proposed reflectarray design since it is easy to fabricate, losses are relatively low compared to conventional microstrip patches even at high frequencies, and due to its uni-planar structure, the ease of integration with active and passive devices - such as MEMS phase shifter. A coplanar patch antenna consists of a rectangular or square microstrip patch with a closely surrounded ground conductor which makes the antenna ideal for coplanar waveguide (CPW) feed.

The concept of the CPA was introduced by J.W. Greiser in 1976 [22]. Back then the antenna was considered to be a loop slot antenna since it looks very similar but it behaves more like a rectangular patch antenna since the resonant properties are

determined by the length of patch, not the total length of the loop. Therefore the width of the patch can now be used as a free parameter for impedance matching. The microstrip patch-like behavior of the CPA was confirmed with measurements and a full-wave simulation by K. Li et al. in [23].

Tuning elements are connected to the antennas with conductor-backed coplanar waveguide (CBCPW) transmission lines which are also compatible with MEMS-phase shifters in the future. The major issue with CBCPWs is the unwanted wave mode creation [24]. Although the desired CPW-mode must propagate without notable attenuation, the generation of most dominating unwanted wave mode, the parallel-plate-mode, must be prevented to maintain the sufficient efficiency for the antenna element. For the static reflectarrays, the leakage of power to the substrate between the parallel ground planes is prevented by surrounding each coupled antenna element with grounding vias, which can be seen in Fig. 2.3. The via pattern and antenna dimensions are optimized with simulations.

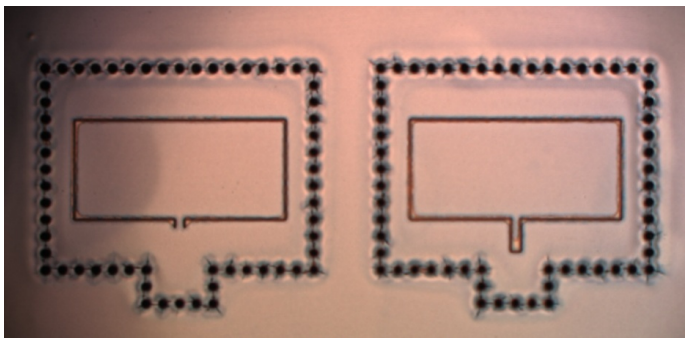

Figure 2.3: Microscope image of the static reflectarray antenna elements. The 54-μm long short-circuited stub (left) and the 195-μm long open stub (right) represents the relative phase shift of $-180°$ and $0°$, respectively. Grounding vias are shown in black around the antenna.

The resonant frequency of the CPA can be determined with the theory of conventional microstrip patch antenna as:

$$f_{res} = \frac{c}{\sqrt{\epsilon_r(L + \Delta L)}}, \tag{2.74}$$

where c is the speed of light, L is the length of the patch and ΔL is the effective length extension due to fringe fields. Since the resonant properties of the CPA is determined by the length L, thus the width of the patch can be used to improve matching between the patch and the CBCPW transmission line.

2.3.2 Reflection coefficient of the element

Design curves of the reflectarray element can be determined by performing a full-wave simulation with a commercial simulation software such as Ansoft HFSS or CST

Microwave Studio. A reflectarray cell is modeled with the specifications introduced in [19] and [12].

The HFSS simulation model presented in Fig. 2.4 consists of two ports. Port #1 is a Floquet mode excitation which simulates the incident plane wave and port #2 is lumped to the end of the CBCPW transmission line. The effect of the adjacent elements are taken into account by using periodic boundary conditions, which simulates an infinite array of similar elements. The design curves for both shorted and open-ended case are obtained with a parametric sweep by varying the length of the stub from 0 to 400 µm.

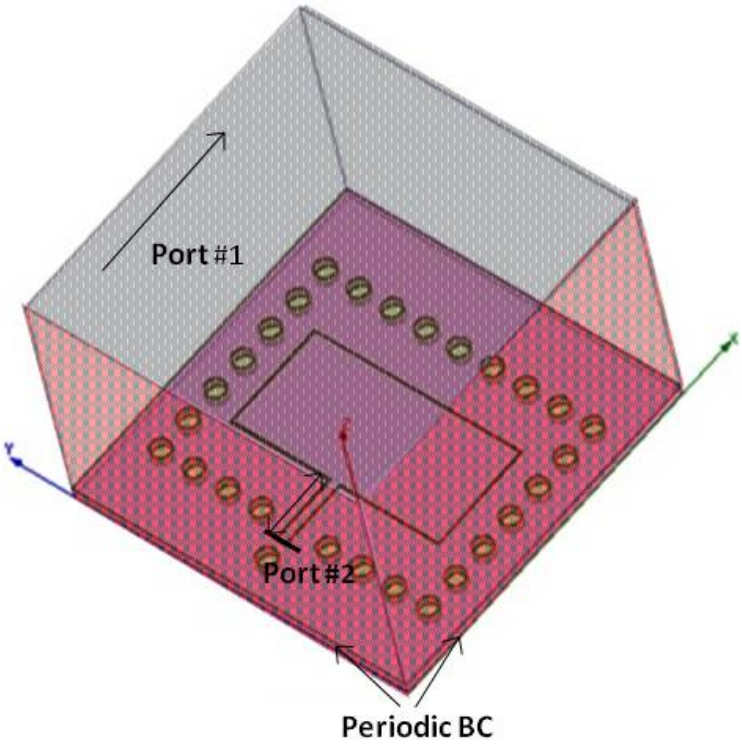

Figure 2.4: Simulation model of the RA element.

The reflection coefficient of the element can be calculated from the simulated two-port system with

$$\Gamma_e = \Gamma_s + \Gamma_m = S_{11} + \frac{S_{21}S_{12}\rho_l}{1 - S_{22}\rho_l}, \tag{2.75}$$

where Γ_s is the specular reflection (S_{11} in the simulation model) [12]. The second summand, Γ_m, represents the modulated part of the reflection coefficient. S_{21} and S_{12} describe the coupling between the patch and the transmission line and S_{22} is the reflection from the antenna terminal. The reflection from the end of the stub is represented with

$$\rho_l = e^{-j\theta_e}, \tag{2.76}$$

where the short and open ends of the transmission line are achieved with angles of $-1.6°$ and $175.8°$. The angles differ from ideal $0°$ and $180°$ due to short-circuit inductance and open-end capacitance [12].

The simulated reflection coefficient for both shorted and open-ended are shown in Fig. 2.5. When comparing the produced circles in the complex plane, the radius is smaller for the open-ended stub which means slightly poorer element efficiency since the amplitude of the reflection coefficient, $|\Gamma_m|$, is determined by the radius. The reason for using both short-circuited and open-ended stubs is that the use of only one type of termination would significantly increase the stub length and thus the stub has to be twisted, which increases the level of cross-polarization [2].

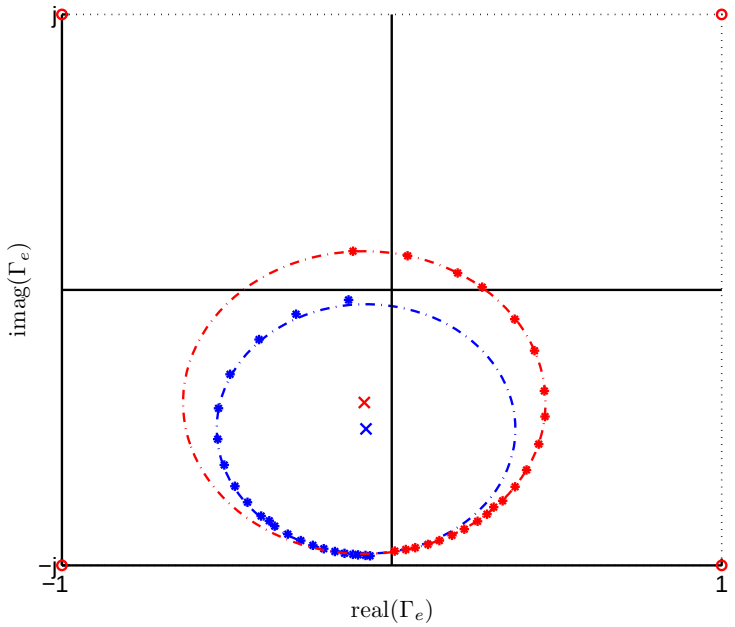

Figure 2.5: Simulated reflection coefficient with short-circuited (red) and open-ended stub in the RA element. Central points of these circles marked with crosses corresponds the specular component of Γ_e.

The alignment of the circles differ from the origin of the plane due to offset-component produced by the specular reflection Γ_s from the ground plane. When the specular component represented with a x-mark is subtracted from Γ_e, the modulated component of the element reflection coefficient can be represented in more conventional manner seen in Fig. 2.6, where the angle θ_e is changing in respect of the length of the stub.

When a reflectarray element is illuminated by an incident field from the transmitter, all the energy (substrate and conductor losses are ignored in this example) is scattered back due to existence of the ground plane below the substrate. The back-

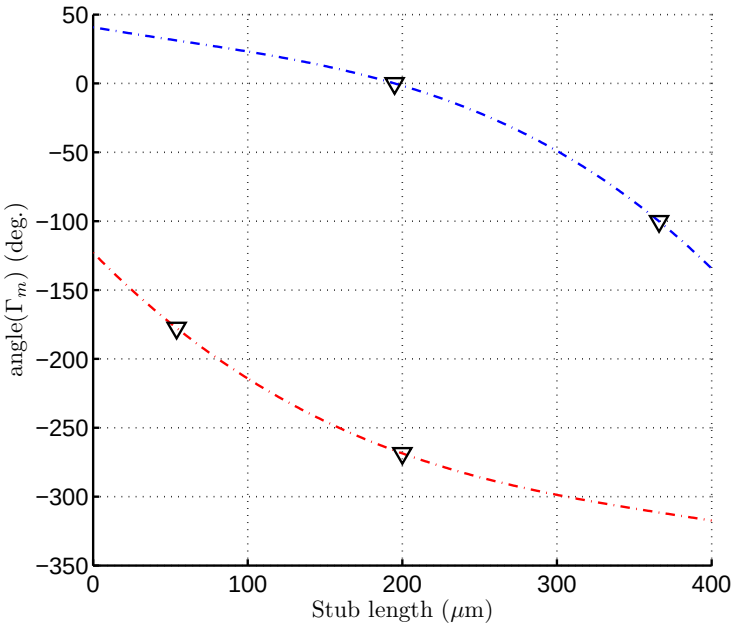

Figure 2.6: Phase of the simulated reflection coefficient with short-circuited (red) and open-ended stub in the RA element.

scattered field is a summation of three components. The first one is the re-radiated component due the resonant activity of the patch, the phase of which is proportional to two times the length of the attached delay line. The second one is the specular component which is caused by reflections from the ground plane between the elements. If the matching between the antenna element and the phase shifter is poor, a part of the power captured by the antenna is reflected without being phase shifted. The third one is a reflection from the non-resonant structures of the antenna. Because substrates of reflectarrays are generally very thin, the thickness of which much less than 0.1 λ_0, only the first two components seen in Fig. 2.7, dominate [2].

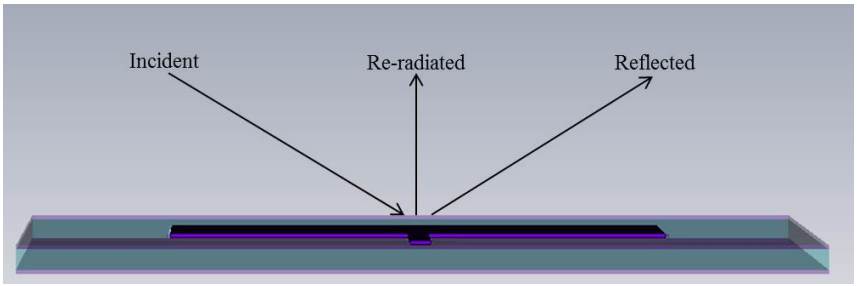

Figure 2.7: Two dominant components of the field scattered from the reflectarray element. Reflected component here illustrates the specular reflection from the ground plane.

The reflectarray antenna element efficiency is defined with Eq. (2.77) [12]. It de-

scribes how the reflected power is divided between the steered beam and the specular reflection:

$$\eta_e = \frac{|\Gamma_m|^2}{|\Gamma_m|^2 + |\Gamma_s|^2}, \tag{2.77}$$

where $|\Gamma_m|$ and $|\Gamma_s|$ can be determined from Fig. 2.5. The simulated efficiency for short-circuited and open-ended stubs are 0.64 and 0.45, respectively. The less-than-unity efficiency can be taken into account in beam pattern calculations by using Eq. (2.75) as the reflection coefficient in Eq. (2.73) [12]. The dimensions and corresponding relative phase shifts of the chosen CBCPW stubs are listed in Table 1.

Table 1: Phase shifting stubs

Parameter	Value		
CBCPW impedance	50 Ω		
CBCPW center conductor width	50 µm		
CBCPW slot width	8 µm		
Relative phase-shift	length	end	efficiency
0°	195 µm	open	0.45
−90°	366 µm	open	0.45
−180°	54 µm	short	0.62
−270°	200 µm	short	0.62

2.3.3 Fabricated reflectarrays

Before designing the final, reconfigurable reflectarray, three static RA wafers have been manufactured for measurements. A photo of one fabricated RA is presented in Fig. 2.8. These antennas are focused to three different focus points. The focus point in two of them is at boresight direction, the first one at 3 m and the second one at 3 km. The third one is focused 0.5-m off-boresight at 3-m distance. Antenna elements of these static reflectarrays are coupled with both open-ended and short-circuited stubs with various lengths for discrete 4-state phase shift generation.

Reflectarrays are fabricated on the top of a 150 mm silicon wafer by a lithographic process. The bottom layer is a 1 µm thick copper ground plane. The substrate layer is 50 µm thick polyimide, the relative permittivity of which is 3.5. For the reconfigurable RA, the substrate material will be replaced with SU-8. The antenna elements are etched to the 1 µm thick copper layer and surrounded with grounding vias trough the substrate to improve element-to-element isolation and prevent parallel plate mode creation.

The spacing of the elements is chosen to be 2 mm ($\approx 0.8\lambda$) and the CPA dimensions are $1250 \times 585\ \mu m^2$. Open-ended and short-circuited CBCPW transmission lines with

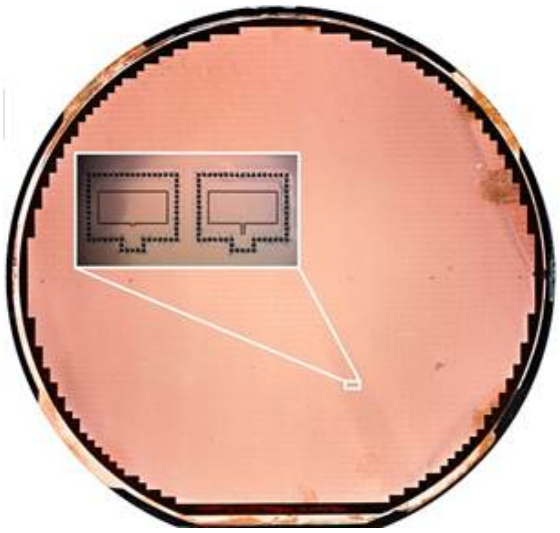

Figure 2.8: Photograph of a fabricated reflectarray antenna.

various lengths are connected to CPAs for four-state phase shift generation. The antenna element has −3 dB beam width in both E- and H-planes. Key features and antenna dimensions of fabricated RAs are listed in Table 2.

Table 2: Parameters of fabricated reflectarrays

Parameter	Value
Focus	RA#1: z=3 m, boresight
	RA#2: z=3 m, 50 cm aside
	RA#3: z=3 km, boresight
RA diameter	138 mm
Number of elements	3700
Element spacing	Δx = 2 mm / Δy = 2 mm
Substrate material	Polyimide
Substrate thickness	50 µm
Substrate relative permittivity	3.5
Substrate loss tangent	0.008
Metallization thickness	1 µm
CPA dimensions	1250×585 µm^2

2.3.4 Radiation patterns

Once the unit cell and the feed pattern are characterized, the radiation pattern of the RA should be accurately calculated so that the main beam width and direction and the side-lobe level could be determined. The beam patterns for the manufactured reflectarrays can be numerically modeled with Eq. (2.73), where the feeding field,

$E_f(\mathbf{r}')$, is the fundamental Gaussian beam mode from Eq. (2.66). The beam waist is chosen to be 3.5 mm, which means −8-dB edge taper for the outermost elements of the RA [12]. Beam patterns for the fabricated reflectarrays are presented in Figs. 2.9-2.11.

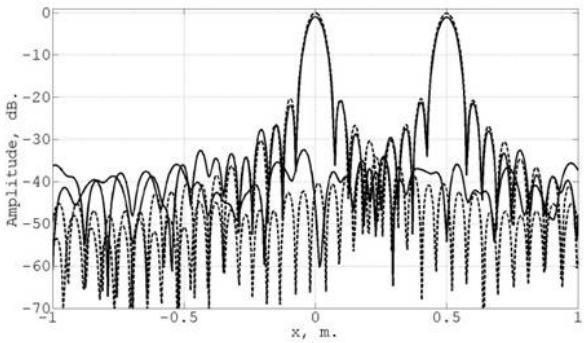

Figure 2.9: Calculated x-axis beam pattern for RA#1 and RA#2 at 3-m distance [12].

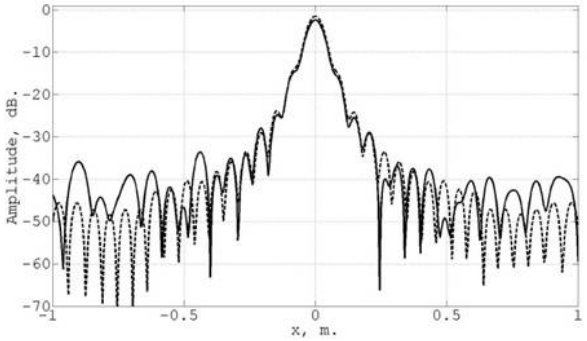

Figure 2.10: Calculated x-axis beam pattern for RA#3 at 3-m distance [12].

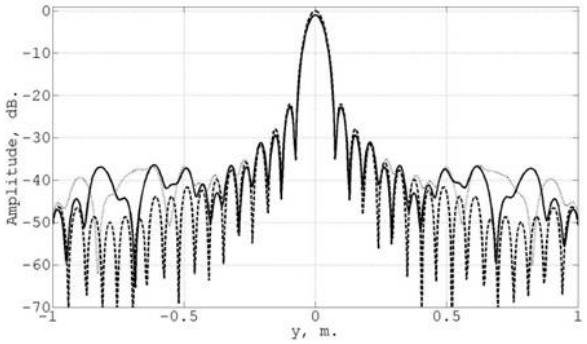

Figure 2.11: Calculated y-axis beam pattern for RA#1 at 3-m distance [12].

The patterns are calculated for both continuous (dashed) and discretized (solid) phase distribution. All patterns are normalized to the maximum of the RA#1 main beam. In this preliminary modeling of the RA, the elements are assumed to be isotropic with an unity radiation efficiency and a zero cross-polarization level. The model is rather simple, but it can accurately predict the main beam width and direction. It also takes into account the discretized phase in the RA [12]. The model can be made more accurate by using Eq. (2.75) in place of the reflection coefficient.

2.3.5 Contribution to manufacturing errors

Manufactured reflectarrays are found to be suffering from over etching, which could decrease the performance of the antenna. Gap width from the ground plane to the patch was measured to be 15.5 µm on average – almost twice the designed value (8 µm). CPAs are in general, like any other type of microstrip patch antennas, very narrow band, and hence very sensitive for dimensional changes. Over etching decreases the effective length of the antenna which determines the resonant frequency of the patch.

The fabricated reflectarrays found out to be slightly curved due to internal contraction and thus the RA planarity was measured with a dial indicator. According to results presented in Fig. 2.12, RAs are concave and their deviation from planar is up to 320 µm, which means a 89° difference in aperture phase. The effect of the RA curvature is taken into account in the beam patterns presented in [12]. It results a slight gain reduction and higher side-lobe level.

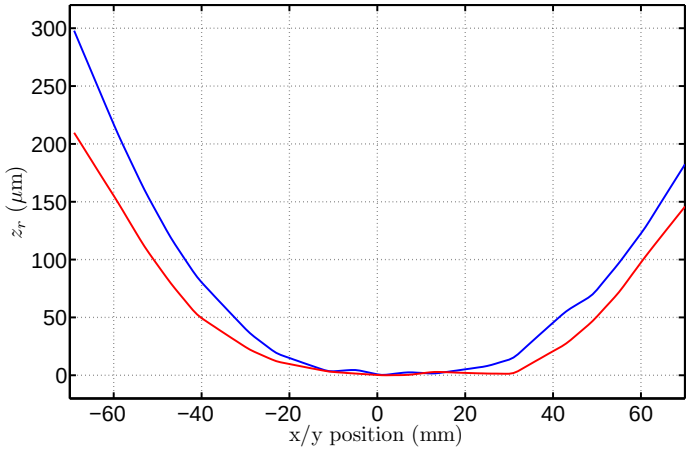

Figure 2.12: Measured planarity of the manufactured reflectarray surface in x- (blue) and y-direction (red).

3 Millimeter-wave near-field imaging

This Section provides information about a near-field measurement method for reflectarray element characterization in addition with calibration and modeling of the measurement scheme. It is widely based on articles "Near-field measurements of a millimeter-wave reflectarray at 120 GHz" in Appendix A [25] and "Calibration method for near-field measurement used in reflectarray characterization" in Appendix B [26] published in the proceedings of the 42nd and the 43rd European Microwave Conference, respectively.

Analysis of the single antenna element in a reflectarray is possible with advanced simulation tools by creating infinite array with periodic boundary conditions. Simulation results can be verified with near-field probe measurements for characterizing behavior of the individual elements a fraction of a wavelength apart from the surface of the reflectarray antenna [27]. Near-field probing of the individual antenna elements of the reflectarray came into consideration because of the need to study reasons for the observed decrease in the modulation efficiency of the antenna elements. According to simulations presented in [19], the modulation efficiency should be above 0.5. It means that the field strength of the specular reflection should be at a lower level than the modulated field. In this thesis, the near-field-probe measurement is applied for studying the behaviour of the antenna elements of the developed reflectarrays at 120 GHz.

Near-field probing of reflectarray antenna surface have been presented by S. Dieter and W. Menzel in [27]. Their paper illustrates a method based on [28] by J.-D. Lacasse et al., which is used to characterize the performance of a static 35-GHz reflectarray elements with different high-resolution probes. Measurement is performed in such a way that the reflectarray is illuminated by an offset open-ended waveguide (OEWG) feed which is located far enough from the RA surface that the far-field conditions can be assumed for the incident field. The scattered field is received with a probe which is located in the near-field region, only a few millimeters from the surface. The position of the RA is automatically controlled during the measurement with a precise scanner. To get an accurate response for both amplitude and phase without a significant interference of the adjacent elements, the measurement must be performed from only a fraction of the wavelength apart from the antenna surface [29].

The presented method can not be directly implemented for our 120-GHz reflectarray characterization for two reasons. First, the structure of our reflectarray is notably different. Modulation of the 35-GHz reflectarray in [27] is carried out with patches of variable size and the antenna does not contain a ground plane at the surface, which increases the effect of edge diffraction. Second, the line-of-sight propagation path from the feed to the measured antenna element would be obscured by the receiver probe. However, when the near-field measurement is performed in such a short distance, the scattering performance of the element is not significantly depended of the angle of incidence [30]. Therefore the same antenna can be used for both illumina-

tion and receiving the scattered field.

Another challenge is the high central frequency of the RA under development as the influence of fabrication errors rises significantly with frequency. This is also a problem for mechanical positioning of the measurement scheme. At the 120-GHz central frequency of our RA, a 100-µm change in distance turns the phase of the received field by 28.8° [26].

3.1 Calibration

Systematic errors are commonly the foremost factor of uncertainty in network analyzer measurements. These errors are caused by mismatch between components of the test unit, finite directivity of directional couplers and crosstalk between channels. Calibration is required to relate the measured electric field to the actual S-parameters of the device under test (DUT) [31]. Since S-paremeters are complex quantities thus besides the amplitude, also the related phase of the parameter is important. Calibration is performed by measuring S-parameters of calibration standards, the electrical characteristics of which such as reflection coefficients are known, in the place of the DUT.

The relation between measured values and actual S-parameters can be described with an error network. The actual S-parameters of the DUT can be calculated from the calibration data by using de-embedding techniques. In general, the calibration process is a way to create a reference plane at the point, where the standards are connected. As long as a precise model of each calibration standard is used, an accurate reference plane can be established.

3.1.1 Impedance de-embedding

De-embedding is a process to determine the impedance of the DUT when the measurements are made from distance and the electrical properties of the intervening structure is known [32]. The structure between the measurement plane and DUT is described with an embedding network, which is in impedance measurements described with a Z-matrix. If we have a known load Z_L which is terminating the embedding network Z, the input impedance can be expressed with a well-known equation as:

$$Z_{IN} = Z_{11} - \frac{Z_{12}Z_{21}}{Z_{22} + Z_L}. \tag{3.1}$$

In a similar way, the equation can be established for reflection coefficients by using flow chart analysis [33]. In Fig. 3.1 a network S has been terminated with a load impedance Z_L. The input reflection coefficient ρ_S can be solved if the S-parameters of the embedding network and the reflection coefficient of the ρ_L are known. The loop of S_{22} and ρ_L does not include any amplification thus it can be copied to the node b_2. The formed loop can be removed by using recursion rule where all other

paths into the node are divided by (1-S). All the nodes which are now connected in series can be combined by multiplying and, hence, the final parallel connection can be added together.

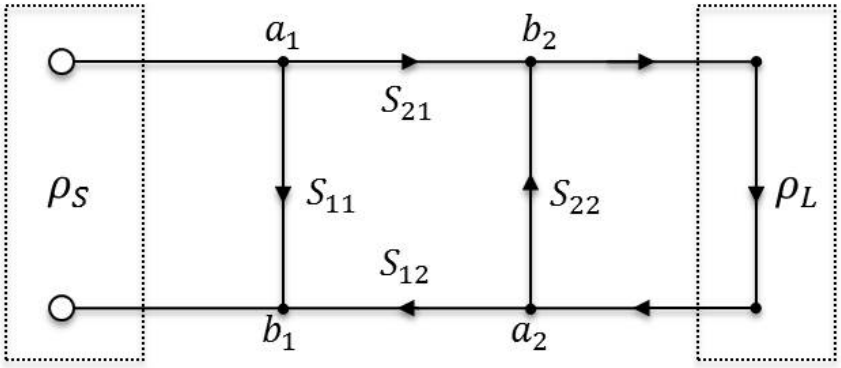

Figure 3.1: Reflection coefficient de-embedding.

The reflection coefficient of the input is:

$$\rho_S = S_{11} - \frac{S_{12}S_{21}}{S_{22} - \frac{1}{\rho_L}}, \tag{3.2}$$

which is similar as Eq. (3.1) except that Z_L is now replaced with $-\frac{1}{\rho_L}$. De-embedding procedure is in fact only an arithmetic problem, which makes it very straightforward to use.

3.1.2 Three-term error model for reflection measurement

The effect of systematic errors can be significantly reduced by applying an error model. For reflection measurements, the simplest way is a response calibration which can be done by measuring short- or open-circuit in addition with a matched load for solving two error terms. However, response calibration does not take into account the port match error which reduces the accuracy of measurement. The most commonly used method for VNA error correction is a short-open-load-through (SOLT) calibration, where the last one (through) is only applied in 2-port measurements. Terms in the model are directivity error E_{DF}, port match error E_{SF} and reflection tracking error E_{RF}. Three-term error model is presented as a flow chart in Fig. 3.2, where the actual reflection coefficient Γ_L can be solved from the measured Γ_S by using the flow chart analysis presented in Section 3.1.1:

$$\Gamma_S = E_{DF} + \frac{\Gamma_L E_{RF}}{1 - E_{SF}\Gamma_L}. \tag{3.3}$$

The actual reflection coefficient of the load is:

$$\Gamma_L = \frac{\Gamma_S - E_{DF}}{E_{RF} - E_{SF}E_{DF} + \Gamma_S E_{SF}}. \tag{3.4}$$

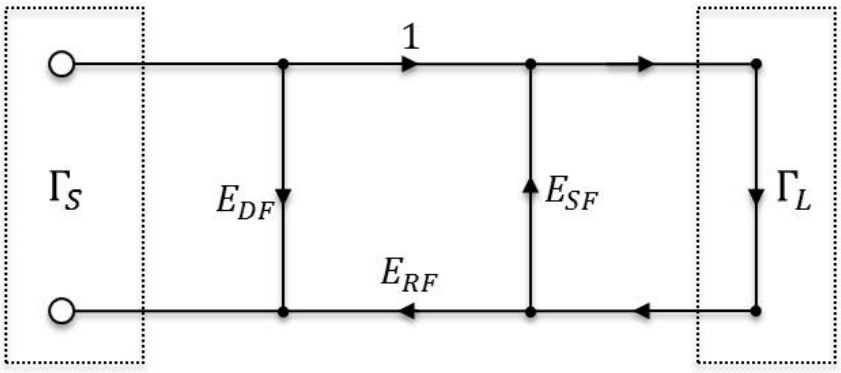

Figure 3.2: Three-term error model for reflection measurement.

To make the equation easier to solve, variables a, b and c are used:

$$\begin{cases} a = E_{RF} - E_{SF}E_{DF}, \\ b = E_{DF}, \\ c = -E_{SF}. \end{cases} \tag{3.5}$$

Eq. (3.4) can be now written as:

$$\Gamma_L = \frac{\Gamma_S - b}{a - \Gamma_S c}. \tag{3.6}$$

In order to solve parameters a, b and c from Eq. (3.6), reflection coefficients Γ_{m1}, Γ_{m2} and Γ_{m3} have to be measured with corresponding loads Z_1, Z_2 and Z_3 whose reflection coefficients Γ_1, Γ_2 and Γ_3 are known:

$$a = \frac{\Gamma_{m2} - \Gamma_{m1} - (\Gamma_{m1}\Gamma_1 - \Gamma_{m2}\Gamma_2)}{\Gamma_2 - \Gamma_1}, \tag{3.7}$$

$$b = \Gamma_{m1} - \Gamma_1 a + \Gamma_{m1}\Gamma_1 c, \tag{3.8}$$

$$c = \frac{(\Gamma_2 - \Gamma_1)(\Gamma_{m3} - \Gamma_{m1}) - (\Gamma_3 - \Gamma_1)(\Gamma_{m2} - \Gamma_{m1})}{(\Gamma_2 - \Gamma_1)(\Gamma_{m1}\Gamma_1 - \Gamma_{m3}\Gamma_3) - (\Gamma_3 - \Gamma_1)(\Gamma_{m1}\Gamma_1 - \Gamma_{m2}\Gamma_2)}. \tag{3.9}$$

The accuracy of the calibration depends on the availability of high-quality calibration standards [34]. For coaxial media, it is easy to fabricate a set of three distinct impedances such as open-circuit, short-circuit and matched load. In a waveguide environment, the task is not that straightforward except the short-circuit which can be applied by using just a flat metal flange.

If the waveguide is terminated with an ideal matched load, the amplitude of the reflected signal is exactly zero. However, a perfect matched load is impossible to fabricate for waveguide environment which means that a small reflection ΔE_{DF} from an unideal termination is always present. ΔE_{DF} adds up with the calibration model

error term E_{DF} and hence reduces the accuracy of the calibration. If the goal is to achieve a precise calibration the effect of ΔE_{DF} can be taken in account with a sliding termination. When the position of the termination is changed the angle between E_{DF} and ΔE_{DF} also changes and sum of E_{DF} and ΔE_{DF} forms an error circle. When the measurement is done with a multiple positions of the load, the actual E_{DF} can be solved from the central point of this circle [35].

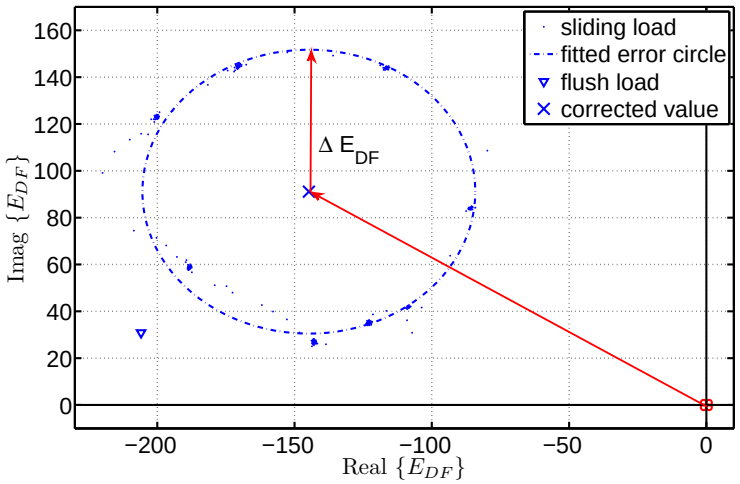

Figure 3.3: Reflection correction for an unideal matched load.

When a sliding load is connected to terminate the waveguide, the measured reflection coefficient is clearly changing in respect to the position of the load. To determine whether its effect is or is not significant, the reflection coefficient of the used open-ended waveguide is evaluated with the method presented above and compared to the result achieved with a static termination, which is often called as a flush load in the literature. Multiple points for the error circle can be determined at once by using MVNA. The position of the sliding load is carefully adjusted on the fly and the corresponding amplitude and phase of the received field is read simultaneously from MVNA. The whole error circle is obtained when the position of the termination has been moved the whole path of a one half guided wavelengths which means that the measured reflection coefficient has arrived to the same position as it was before scan. The measured reflection coefficient of the open-ended waveguide probe is $0.233\angle 40.03°$ with a flush load and $0.227\angle 41.98°$ when the reflection from an ideal load is taken into account. An amplitude error of 2.5 percent and phase error of 1.96° can be significant when the reflection from the probe is used as a reference point for the measurement.

Determination of the calibration standard for open-circuit is slightly more complicated but can be established using offset shorts [36]. In terms of reflection coefficients in a waveguide reflection measurement, open-circuit standard can be achieved by adding a quarter-wave offset shim between the reference plane and a short-circuit

flange. However, for the WR-6 waveguide band, the thickness of such a shim would be only 0.703 mm thus it could easily bend or become distorted during use and hence not a practical choice for a calibration standard. In waveguide calibration kits for millimeter-wave frequency range, a quarter-wave offset shim is commonly replaced with two precise waveguide sections whose separation in thickness is one quarter guided wavelengths, determined in Eq. (3.10), at the central frequency of the waveguide band. Therefore two measurements are needed to realize a calibration standard for open circuit. The guided wavelength is always longer than the wavelength would be in free-space:

$$\lambda_g = \frac{\lambda_0}{\sqrt{1-(\frac{\lambda_0}{\lambda_c})^2}}, \tag{3.10}$$

where the lower cut-off wavelength $\lambda_c = 2a$ and a is the width of the waveguide. For reflectarray central frequency, 120 GHz, guided wavelength in a WR-6 waveguide is 3.8 mm. The scattering parameters of a waveguide section can be expressed as:

$$S_{thru} = \begin{bmatrix} 0 & e^{-\gamma s} \\ e^{-\gamma s} & 0 \end{bmatrix}, \tag{3.11}$$

where s is the length of the transmission line.

$$\gamma = \alpha + j\beta \tag{3.12}$$

is a complex propagation constant, where α denotes the attenuation constant and β is the phase constant.

The calibration kit used here includes waveguide sections with lengths (thicknesses) of 2.542 mm and 3.2741 mm. The difference in length of these sections is 0.7316 mm, which means $0.1915\lambda_g$ in guided wavelengths at 120 GHz. To obtain the response of a waveguide section having the length (thickness) of the difference between the two measured offset shorts, the short-circuited end of the shorter (thinner) waveguide section has to be chosen as the reference plane. Offset short with a longer (thicker) waveguide section can be de-embedded to this plane by using Eq. (3.2):

$$\rho_{ref} = S_{11} - \frac{S_{12}S_{21}}{S_{22} - \frac{1}{\rho_{os}}}. \tag{3.13}$$

Scattering parameters of the waveguide section (Eq. (3.11)) is placed to Eq. (3.13):

$$\rho_{ref} = \rho_{os} e^{-2\gamma s}, \tag{3.14}$$

$$\frac{|\rho_{ref}|}{|\rho_{os}|} e^{j(\phi_{ref}-\phi_{os})} = e^{-2(\alpha+j\beta)s}. \tag{3.15}$$

The propagation constant β can be now calculated from the phase difference of two offset shorts:

$$\beta = \frac{\phi_{ref} - \phi_{os}}{2s}. \tag{3.16}$$

The attenuation coefficient α can also be calculated from the Eq. (3.15) as:

$$\alpha = -\frac{\ln(\frac{|\rho_{ref}|}{|\rho_{os}|})}{2s}. \tag{3.17}$$

However, determination of the attenuation coefficient this way is not feasible due to standing wave between directional coupler and short-circuit termination at the end of the line.

3.1.3 Parameter extraction

Despite the scattered field from the illuminated coplanar patch antenna element, the received field is a vector sum of multiple components illustrated in Fig. 3.4. It is caused by reflections in different parts of the antenna under test (AUT). The measured reflection coefficient, Γ_e of the reflectarray element, can be written in terms as:

$$\Gamma_e = \Gamma_m + \Gamma_s + \Gamma_{probe}, \tag{3.18}$$

where Γ_s is the specular reflection, Γ_{probe} is the reflection from the probe, and Γ_m is the reflection coefficient of the modulated field [28]. Γ_{probe} can be determined with a free-space measurement by placing absorber in front of the probe. Γ_s can be calculated by averaging the measurement data or measuring an equal-sized (to RA) copper plate reference.

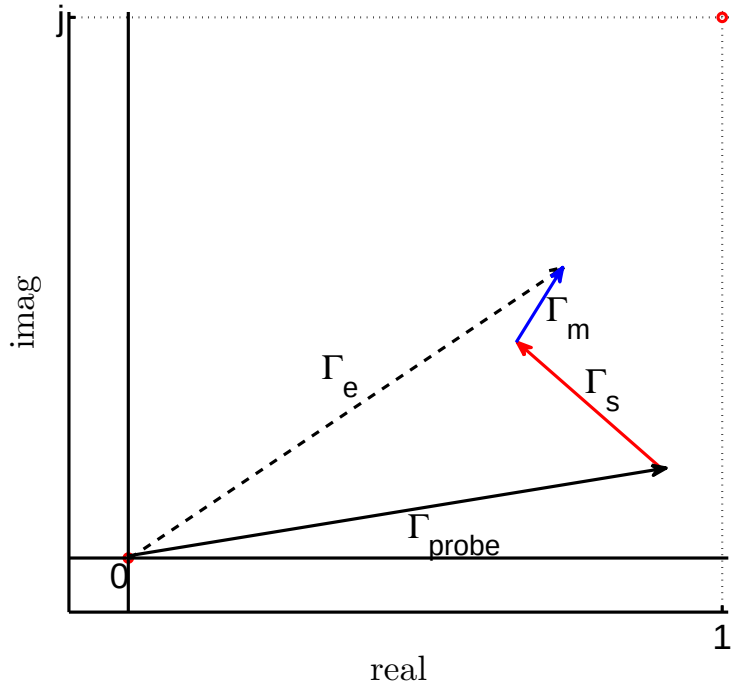

Figure 3.4: Components of the measured reflection coefficient.

3.2 Proposed method for reflection measurement

As stated in the beginning of this Section, applying the characterization method to higher frequencies is challenging due to alignment issues of a separate transmitter and receiver. A way to overcome this problem is to use an integrated near-field probe [37] or a waveguide directional coupler [25]. The proposed measurement setup is presented in Fig. 3.5. Here, the transmitter and the receiver are connected together with a WR-6 waveguide directional coupler. Due to high mm-wave output power (about 32 mW@120 GHz) of the Gunn oscillator, a 10-dB waveguide attenuator is placed between the transmitter and the directional coupler. It is used to prevent the signal to be cut in the receiver amplifier and to reduce the effects of the multiple reflections.

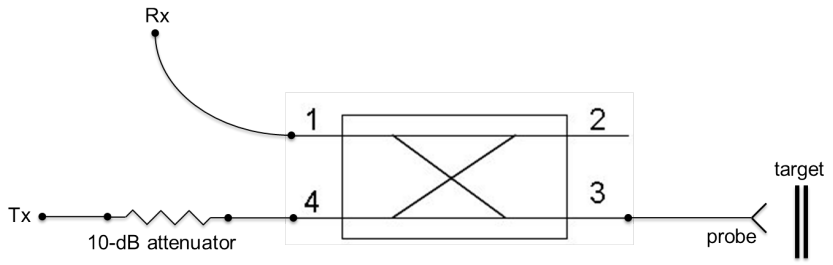

Figure 3.5: Proposed measurement scheme for near-field imaging.

The directional coupler is fed with a millimeter-wave network analyzer (MVNA). Its tunable local oscillator produces a stable microwave signal which is multiplied to a 120-GHz millimeter-wave signal. The multiplier output and open-ended waveguide probe is connected to the through path of the directional coupler. The sample taken from the reflected field received by the probe is mixed back to microwave frequency for the receiver of the MVNA. Besides the reflected field from the target, also a small part of the transmitted field is leaking straight to the receiver due to reflection from the probe and unideality of the directional coupler. To achieve a better signal-to-noise ratio, the transmitter multiplier was replaced with a millimeter-wave extension Gunn-oscillator.

3.2.1 Probe selection

Various types of probes can be used for near-field millimeter-wave imaging. The simplest solution is to use an open-ended waveguide (OEWG) as a receiving antenna, although it can at its best reach for a slightly below one wavelength cross-range resolution. However, the performance of a waveguide can be improved by filling it with a dielectric material, for example with a sapphire rod. The rod is shaped in such a way that outside of the waveguide there is a sharp tip of the rod where the field is focusing. Dimensions can be optimized with simulation tools for a specific frequency.

Another option is to use conical antennas filled with dielectric material, for example corrugated conical horn antenna which is used as a feed antenna for the reflectarray.

The dielectric probe could be manufactured out of Teflon, Rexolite, or other easily machined material. The probe antenna beam depends on its dimensions and dielectric characteristics. Because of the spherically symmetric shape of the conical probes, the resolution is nearly the same in every direction unlike in rectangular-waveguide-based probes. In [38], conical Teflon probe have been designed for millimeter wave near-field imaging.

Two different near-field probes have been designed for measuring the surface of the reflectarray. First one is an open ended WR-6 waveguide which is filled by a sapphire rod. The second one is similar to the probe illustrated in [38] but instead of Teflon the probe is made from Rexolite and dimensions have been optimized for 120-GHz frequency.

Both of these probes gave promising results in the simulations but did not achieve the performance of an open-ended waveguide. Although both of the designed probes focused the beam sufficiently, power leakage before the tip of the probe causes unwanted illumination of the adjacent elements. Also, the measurement setup alone is fairly complicated and the increased number of multiple reflections from the dielectric material interfaces makes the system more difficult to analyze. Therefore, an open-ended WR-6 waveguide is finally chosen for measurements presented here.

3.2.2 Directional coupler

Directional coupler is a passive reciprocal network where one port is isolated from the input. It provides a method for sampling the propagating power in a transmission line and, hence, is widely used to measure the reflection coefficient in reflectometers and network analyzers. Directional coupler presented in Fig. 3.6 has four ports. One port can be regarded as input where the generator is connected, and divided in a way that the most of the incident power exits from the through port and a fixed fraction of it propagates to the coupled port. Ideally the power flow from port one to the isolated port (which is usually terminated) four is zero, but in reality, a small part of power is coupled to the isolated port as well.

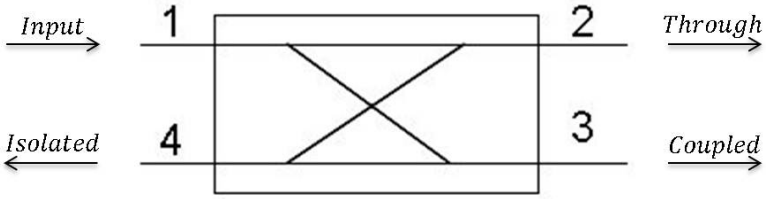

Figure 3.6: Schematic symbol for directional coupler.

The performance of the directional coupler is usually characterized with following quantities [39]:

Coupling

$$C = 10\log\frac{P_1}{P_3} = -20\log|S_{31}|\ \text{dB}, \tag{3.19}$$

Directivity

$$D = 10\log\frac{P_3}{P_4} = C - 20\log\frac{|S_{31}|}{|S_{21}|}\ \text{dB}, \tag{3.20}$$

Isolation

$$I = 10\log\frac{P_1}{P_4} = -20\log|S_{41}|\ \text{dB}, \tag{3.21}$$

Insertion loss

$$L = 10\log\frac{P_1}{P_2} = -20\log|S_{21}|\ \text{dB}. \tag{3.22}$$

The directional coupler is a reciprocal 4-port network which is matched at all ports and hence can be expressed as a following scattering matrix:

$$[S] = \begin{bmatrix} 0 & S_{12} & S_{13} & S_{14} \\ S_{12} & 0 & S_{23} & S_{24} \\ S_{13} & S_{23} & 0 & S_{34} \\ S_{14} & S_{24} & S_{34} & 0 \end{bmatrix}. \tag{3.23}$$

In this work, a WR-6 waveguide directional coupler presented in Fig. 3.7 is manufactured by Millitech®. Although it was known that the used coupler is a high-quality device, it was measured to be aware its performance.

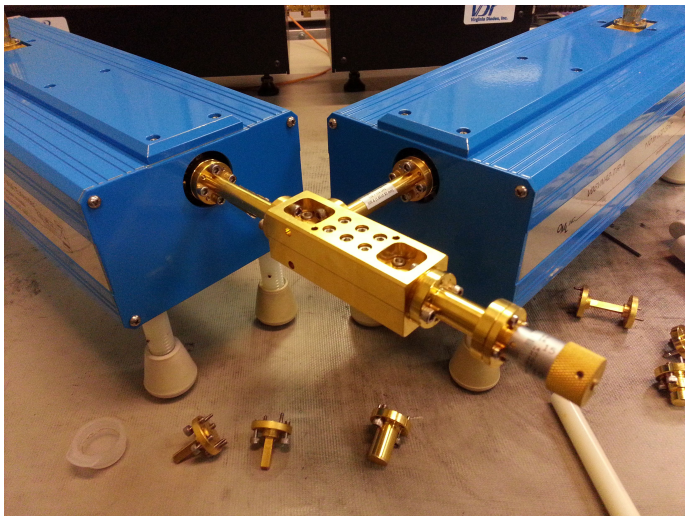

Figure 3.7: Directional coupler was measured with programmable network analyzer (PNA).

Measurements results presented in Fig. 3.8 were performed for the whole D waveguide band ($110 - 170$ GHz). All unknowns required in Eqs. (3.19)-(3.22) can be determined with three transmission measurements by connecting a matched load to the unoccupied port. The directivity found out to be from 29.8 dB to 35.7 dB along

the band (30.6 dB@120 GHz), which is an expected result since the manufacturer declares the directivity to be above 28 dB in D-band. Isolation (> 40 dB), insertion loss (< 3.18 dB) and the coupling flatness (< 1.42 dB) found out to be better or the same order as the value declared by the manufacturer. Only the coupling value (11.8 dB) was 1.8 dB higher than declared.

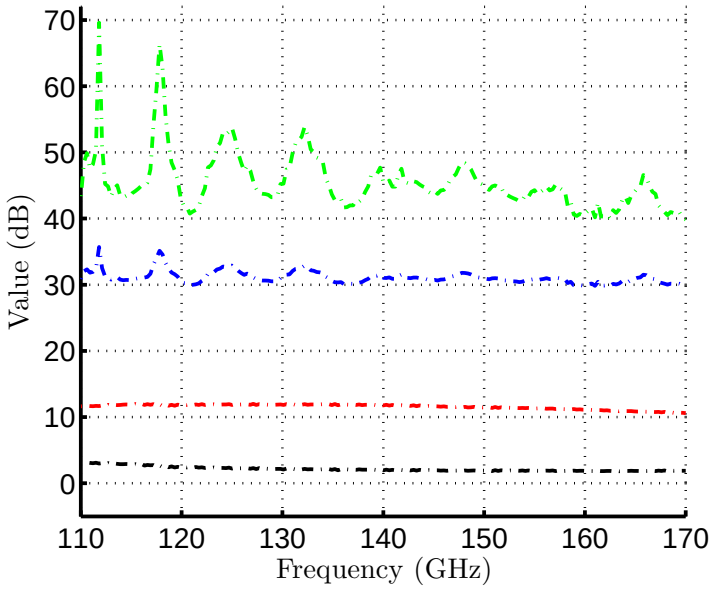

Figure 3.8: Measured isolation (green), directivity(blue), coupling (red) and insertion loss (black) of the WR-6 waveguide directional coupler.

3.2.3 Probe-target interaction

A way to evaluate the proposed measurement method is to measure a sample with known quantities. A convenient way to do so is to measure a metal plate drawn away from the probe. When the plate is moved away from the probe aperture, the phase of the received field is changing in respect to two times the change in the distance z of the plate and the probe compared to the free-space wavelength. Respectively, also the amplitude is decreasing with z and approaches the reflection coefficient of the probe. For a flat metal plate manufactured from good conductor such as aluminum, the reflection coefficient can be assumed to be exactly -1. Situation can be compared to the case of two antennas pulled away from each other. Raw measurement data presented in Fig. 3.9 has to be calibrated to take into account the effect of the directional coupler used in the measurement scheme. Thus, the reflection coefficient of the drawn away metal plate calculated with Eq. (3.6).

However, when the reflection coefficient calculated with Eq. (3.6) is examined in a complex plane presented in Fig. 3.10, one can come to a conclusion that an offset component exist in the result. This offset component is present due to the insertion loss of the OEWG probe. The measurement scheme is calibrated to the waveguide

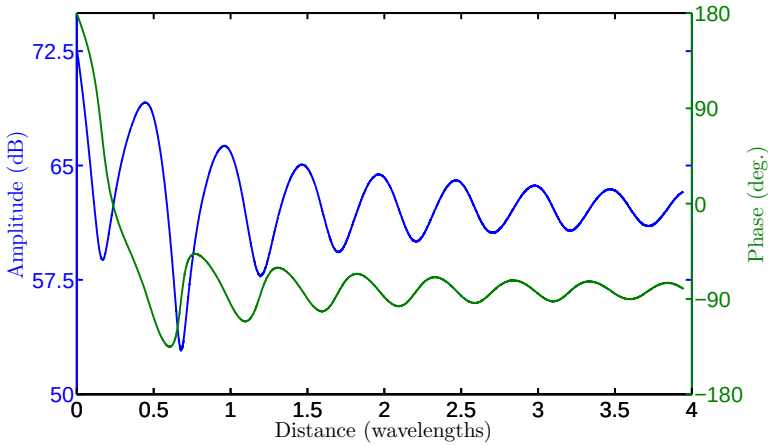

Figure 3.9: Amplitude and phase of the measured field strength (uncalibrated) when a copper plate is drawn away from the probe aperture.

flange, where the probe is connected, not to the tip of the probe. Thus, the part of the energy which is propagating in a waveguide is reflected straight back from the probe. The effect of this component is, however, an easy task to reduce by subtracting the reflection coefficient of the probe from measurement data.

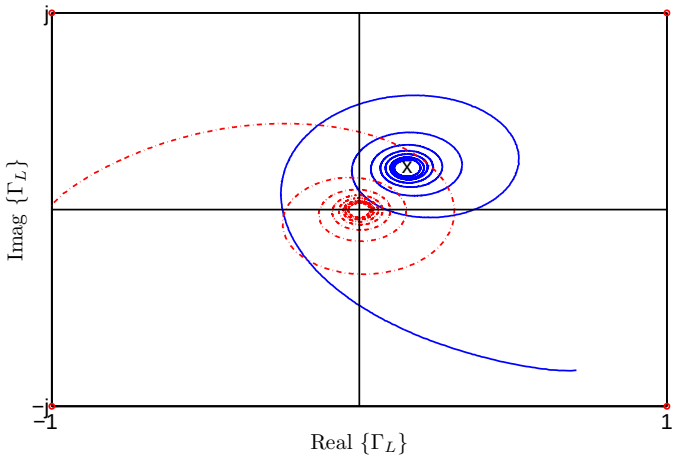

Figure 3.10: Measured reflection coefficient of a drawn away copper plate. The blue curve is obtained with calibration, and the dashed red curve, by an offset-correction of which.

The reflection coefficient of the probe can be obtained from the central point of the blue spiral, a black cross in Fig. 3.10 or equivalently, by measurement, in which absorber material is placed in front of the probe. However, when measuring a sample with unknown quantities, such as in reflectarray measurement, it is impractical to measure a drawn away metal plate every time. The dashed red curve in Fig. 3.10 represents this offset-corrected result, which is normalized and rotated in such a way

that in the position of $z = 0\,\text{mm}$, the reflection coefficient $\Gamma = 1\angle 180°$.

For a better illustration, it is convenient present the amplitude and phase of the reflection coefficient separately, with respect to the distance between the plate and the probe. Fig. 3.11 represents the amplitude (blue curve) and the phase (green curve) of the reflection coefficient calculated by the presented calibration method. The red curve is only normalized and offset corrected result of the amplitude, which is drawn in the same figure to confirm that the calibration is calculated properly. As suspected, there are noticeable fluctuation present in the amplitude due to a standing wave between the plate and the probe. This phenomena was tried to be reduced by the use of an OEWG with a sharpened tip in the measurement. In phase, the difference between these methods is not significant.

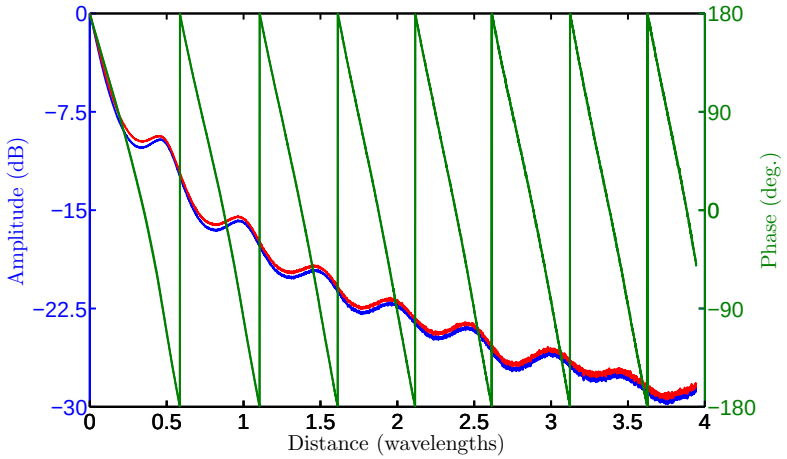

Figure 3.11: Amplitude and phase of the measured reflection coefficient, when a copper plate is drawn away from the probe aperture.

The situation was also simulated with HFSS by making a parametric sweep for probe position in respect to a metal plate. The probe was modeled in such a way that it matches with the dimensions of the real one used in measurements. The comparison between measured and simulated reflection coefficient is presented in Fig. 3.12. The phase of the measured reflection matches with the simulation result and the small difference could be caused by higher sampling interval. The measured amplitude is noticed to be decreasing more rapidly, but the shape of the curve is in a good agreement with the simulated one. At large distances, the amplitude approaches the measurement result. One thing which can explain the quicker amplitude drop is that in the simulation, aluminum plate was used instead of copper, from which the measured plate was manufactured.

It is useful to produce a mathematical model for the case of a metal plate drawn away from the probe. It can be easily done using curve fitting toolbox in Matlab. The amplitude of the reflection coefficient is modeled with a third order polynomial

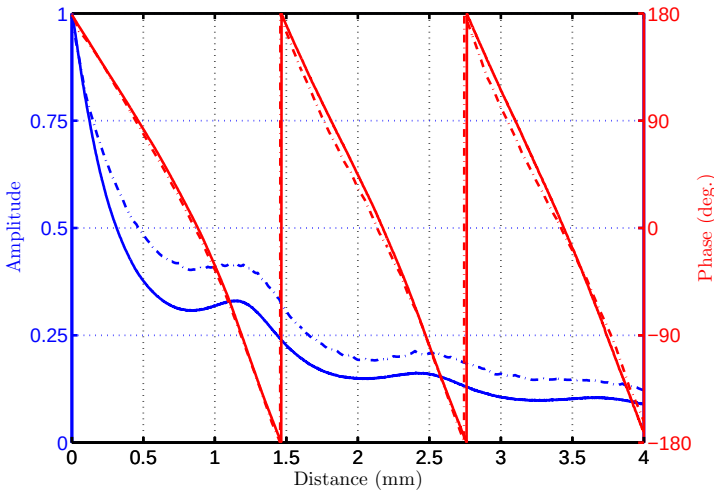

Figure 3.12: Amplitude and phase of the (solid) measured and (dashed) simulated reflection coefficient, when a copper plate is drawn away from the probe aperture.

in respect to the probe-target distance z:

$$|\Gamma_{plate}(z)| = \frac{1}{a_3 z^3 + a_2 z^2 + a_1 z + a_0}, \tag{3.24}$$

where

$$a_3 = 2.04 \times 10^5, \tag{3.25}$$
$$a_2 = 5.21 \times 10^4, \tag{3.26}$$
$$a_1 = 2.37 \times 10^3, \tag{3.27}$$
$$a_0 = 1.05. \tag{3.28}$$

In a similar manner, the reflection coefficient phase can be determined with a first order polynomial:

$$arg(\Gamma_{plate}(z)) = b_1 z + b_0, \tag{3.29}$$

where

$$b_1 = -4.96 \times 10^3, \tag{3.30}$$
$$b_0 = 4.22. \tag{3.31}$$

Hence, a mathematical expression for reflection coefficient is:

$$\Gamma_{plate}(z) = \frac{1}{2.04 \times 10^5 z^3 + 5.21 \times 10^4 z^2 + 2.37 \times 10^3 z + 1.05} e^{-j(4.96 \times 10^3 z - 4.22)}. \tag{3.32}$$

In Fig. 3.13, the measured reflection coefficient is compared to one calculated with Eq. 3.32. Modeled coefficient can be noticed to be in a fair agreement with the measured one, although the phase fit does not work before the distance z >1 mm due to nonlinear phase decrease caused by multiple reflections.

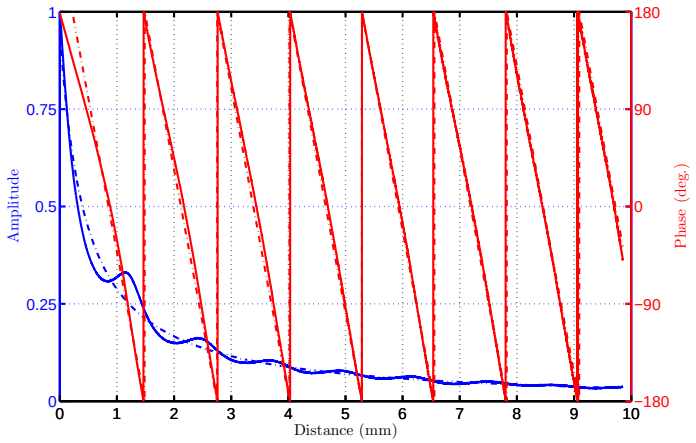

Figure 3.13: Amplitude and phase of the (solid) measured and (dashed) modeled reflection coefficient, when a copper plate is drawn away from the probe aperture.

3.2.4 Test target

Staircase shaped test target presented in Fig. 3.14 has been manufactured for the purpose of verifying proposed measurement method's functionality. A piece of high quality aluminum has been milled to the staircase form where each 10-mm wide step has a 200-µm difference in depth to the adjacent step. This corresponds to a phase difference of 57.6° for the back-reflected field from adjacent steps of the test target. To rule out machining errors, its profile was measured with a dial indicator.

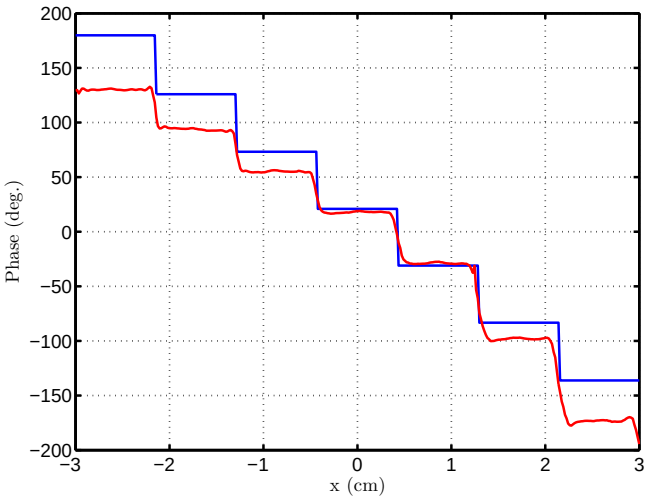

Figure 3.14: Staircase-shaped test target.

At the center of the target, the measurement result is in a good agreement with one calculated directly from the test target profile measured with a dial indicator. At small distances the change of phase between the adjacent steps is lower than the

calculated one, but the phase difference between the farthest steps is in a fair agreement with calculations. It indicates that the test target was slightly tilted during the measurement. However, alignment errors can be taken into account with test target by integrating the dial indicator to the measurement setup.

4 Measurements

The functionality of manufactured static, stub-tuned reflectarrays is verified with three different measurement methods.

(i) Beam patterns of manufactured reflectarrays are measured at 3-m distance.

(ii) The plane-wave spectrum and the diffraction efficiency of the reflectarray is determined with near-field imaging of the antenna aperture field.

(iii) Measurement from a fraction of a wavelength above the reflectarray surface is performed in order to characterize the reflection behavior of individual antenna elements in the reflectarray.

This thesis is mainly concentrated to the last one, although results of the first two are briefly presented.

4.1 Near-field measurement range

Both beam patterns and reflectarray surface are measured at 120 GHz using vertical polarization. The measurement range consists of a millimeter-wave vector network analyzer MVNA-8-350 manufactured by AB Millimétre. The transmitter used here is a fundamental frequency Gunn-oscillator millimeter-wave extension with an output of a WR-10 OEWG. In measurements (i) and (ii) it feeds the corrugated horn antenna, the phase center of which locates at a point (x=−15 cm, y=0, z=30 cm), when the origin is at the center of the RA and the z-axis is the antenna boresight direction. The setup for measurement (ii) is presented in Fig. 4.1.

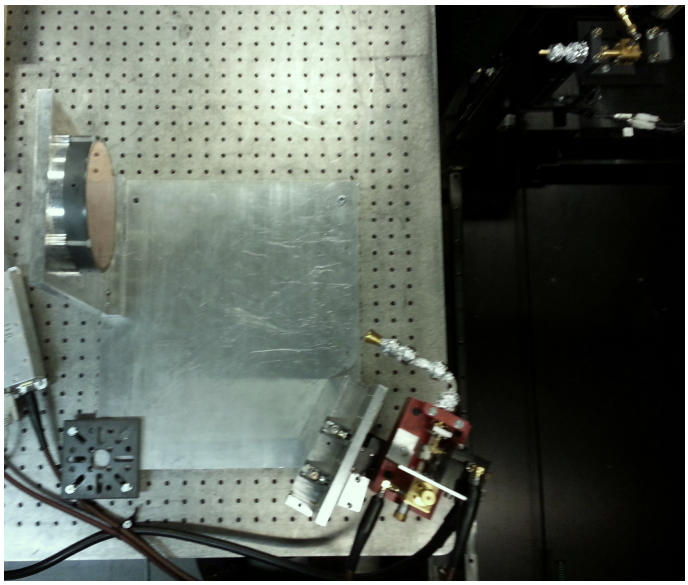

Figure 4.1: The measurement scheme for near-field imaging of the RA aperture field.

As a receiver, a conventional D-band harmonic multiplier is used with a tapered WR-6 OEWG probe. The receiver is attached to a precise near-field planar scanner, NSI 200V–5×5, at the distance of z=3 m and z=0.6 m for measurements (i) and (ii), respectively. The measurement setup is build on to an optical table, the planarity of which is confirmed with a precise bubble level. Absorber material was used to avoid multi-path propagation caused by reflections from the holding structure. The RA, the transmitter, and the receiver are aligned with lasers. Later on, a special holder for the transmitter and the RA was manufactured from aluminum to improve the alignment accuracy of the measurement scheme.

In measurement (iii), which is described further in detal in Section 3.2, the transmitter is connected to the OEWG probe trough a waveguide directional coupler. For a better dynamic range, the same Gunn-extension as in measurement (i) and (ii) is used in the setup. Reflectarray scanning is performed in such a way that the measurement probe stands still and the reflectarray is attached to a scanner which moves the antenna in the XY-plane and reads the corresponding amplitude and phase values from the MVNA. The measurement set-up is presented in Fig. 4.2.

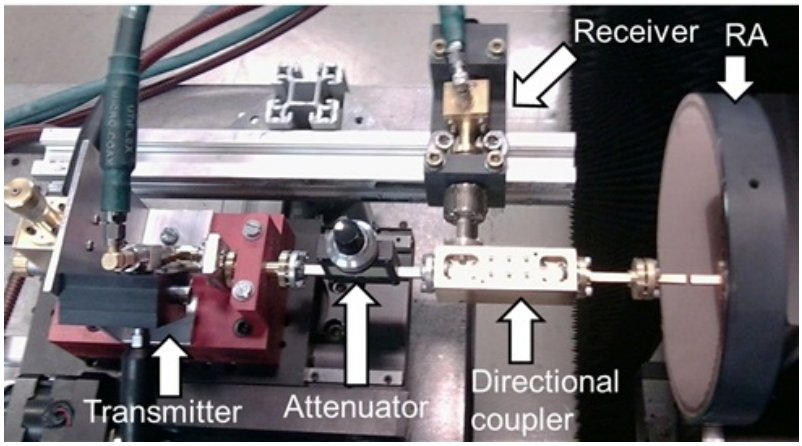

Figure 4.2: The measurement scheme for RA surface measurement.

The goal is to measure a reflection coefficient of individual antenna elements directly from a fraction of a wavelength apart from the RA surface. The measurement results and calibration are presented in Section 4.4.

4.1.1 Near- to far-field transform

The planar near-field technique is an effective method for measuring a performance of large (compared to the wavelength) high-frequency antennas [40]. The idea is to convert the measured phase front into an angular spectrum which means the spectrum of directions in which the energy is traveling. The procedure is often called the near- to far-field transformation. The term is quite misleading as the input and the output of the transform are at the same location, the location at which the

measurement were made. However, the result of the transform is equivalent to a far-field pattern because the radiated near-field energy is always traveling a straight line at any distance from the AUT [40].

The near-field amplitude and phase distribution are measured by scanning a probe in the antenna aperture field over a preselected surface which may be a plane, a cylinder or a sphere. The measured data are then transformed to the far-field using Fourier transform methods. In general, the planar system is better suited for high-gain antennas such as reflectarrays. The acquisition of the planar near-field data is often carried out with a rectangular grid and the sampling points of which must satisfy Nyquist sampling criterion, $\Delta_{x,y} \leqslant \frac{\lambda}{2}$ [41].

The scan region is chosen in such a way that the signal at the edges of the plane has very low intensity, usually about -45 dB below the largest signal level. The measurement plane is determined with

$$M = \frac{a}{\Delta x} + 1, \tag{4.1}$$

$$N = \frac{b}{\Delta y} + 1, \tag{4.2}$$

where $\Delta_{x/y}$ is the sampling interval, a and b are the width and hight of the measurement plane, respectively. If the measurement plane locates in the far-field of the source, the sample spacing can be selected to the maximum value of the Nyquist criterion. Usually the sampling of the grid is selected by the grid spacing of:

$$\Delta_x = \frac{\pi}{k_{x0}}, \tag{4.3}$$

$$\Delta_y = \frac{\pi}{k_{y0}}, \tag{4.4}$$

where k_{x0} and k_{y0} represent the largest magnitudes of the spatial frequency components k_x and k_y.

Although there is no minimum sample spacing restriction, increasing the near field sample points more than the limit above does not improve the resolution of the far-field pattern. This will only increase the limits of the wavenumber spectrum points, which are in the higher order evanescent mode region [41].

However, there is a way to improve the resolution of the far-field pattern by adding artificial sampling points (with zero value) to the outer extremes of the near-field distribution [41]. This method is often called zero-padding. Instead of using $M \times N$ raster, the grid is enlarged with

$$MI = 2^{ceil(log_2 M)+1}, \tag{4.5}$$

$$NI = 2^{ceil(log_2 N)+1}, \tag{4.6}$$

where the *ceil*-function rounds the element to the nearest integer towards the positive infinity. The spatial frequency components can now be determined:

$$k_x = \frac{2\pi m}{MI\Delta_x}, \tag{4.7}$$

$$k_y = \frac{2\pi n}{MI\Delta_y}, \tag{4.8}$$

where

$$-\frac{MI}{2} \leq m \leq \frac{MI}{2} - 1, \tag{4.9}$$

$$-\frac{NI}{2} \leq n \leq \frac{NI}{2} - 1. \tag{4.10}$$

The plane-wave spectrum of the aperture field can be now evaluated with a two-dimensional Fourier transform:

$$\mathbf{A}(k_x, k_y) = \iint_{S_a} \mathbf{E}(x, y, z_m) e^{-j(k_x x + k_y y)} dx dy, \tag{4.11}$$

where k_x and k_y are the horizontal and vertical spatial frequency components, respectively. The probe position is determined with x, y and z_m in such a way that the origin is at the center of the scan plane. The scan pattern is chosen to be planar, thus the depth component, $k_z z_m$, can be dropped out from the exponential [40].

In most cases it is convenient to represent the far-field pattern in angular domain such as in far-field measurement range acquired with a elevation over azimuth positioner. The spatial frequency components can be described in terms of elevation and azimuth angles $\theta_{el.}$ and $\theta_{az.}$, respectively:

$$k_x = \sin\theta_{az.} \cos\theta_{el.}, \tag{4.12}$$

$$k_y = \sin\theta_{el.}, \tag{4.13}$$

$$k_z = \cos\theta_{az.} \cos\theta_{el.}. \tag{4.14}$$

4.1.2 Computational back-propagation

Since the Fourier transform is a linear operation, the calculated plane-wave spectrum in the spatial domain can be converted back to the measured near-zone electric field by an inverse Fourier transform:

$$\mathbf{E}(x, y, z_m) = \iint_{S_a} \mathbf{A}(k_x, k_y) e^{j(k_x x + k_y y)} dk_x dk_y. \tag{4.15}$$

By including the tangential, k_z, into Eq. (4.15), the calculated plane-wave spectrum can be back-propagated to a different plane parallel to the aperture. This procedure is often called a plane-to-plane transform. Thus, the calculated PWS from the

measured aperture field of the reflectarray can be back propagated to the electric field in the surface of the antenna by the expression:

$$\mathbf{E}(x, y, z_{RA}) = \iint_{S_a} \mathbf{A}(k_x, k_y) e^{j(k_x x + k_y y)} e^{-jk_z(z_{RA} - z_m)} dk_x dk_y, \tag{4.16}$$

where k_z can determined with k_x and k_y by using the relation in Eq. (2.35):

$$k_z = \begin{cases} k_0\sqrt{1 - k_x^2 + k_y^2}, \text{ for } k_x^2 + k_y^2 < 1, \\ 0, \text{ for } k_x^2 + k_y^2 \geq 1. \end{cases} \tag{4.17}$$

To simplify the calculation of the PWS, the scan plane is chosen as a reference plane in such a way that $z_m = 0$. Thus the term z_{RA} lies in the negative z-axis, because the direction of energy propagation (minus sign in the second exponential) is from RA towards the measurement plane.

The plane-to-plane transform is a conventional tool to characterize how much energy is lost to the specular reflection. An estimate for the RA element efficiency can be determined by dividing the plane-wave spectrum to the main beam and specular reflection components in respect of direction of propagation [12]. Then the field of these components is back propagated in the RA surface and an estimate of the element efficiency is calculated with Eq. (2.77). The result of RA#1 element efficiency calculated by this method is presented in Fig. 4.3.

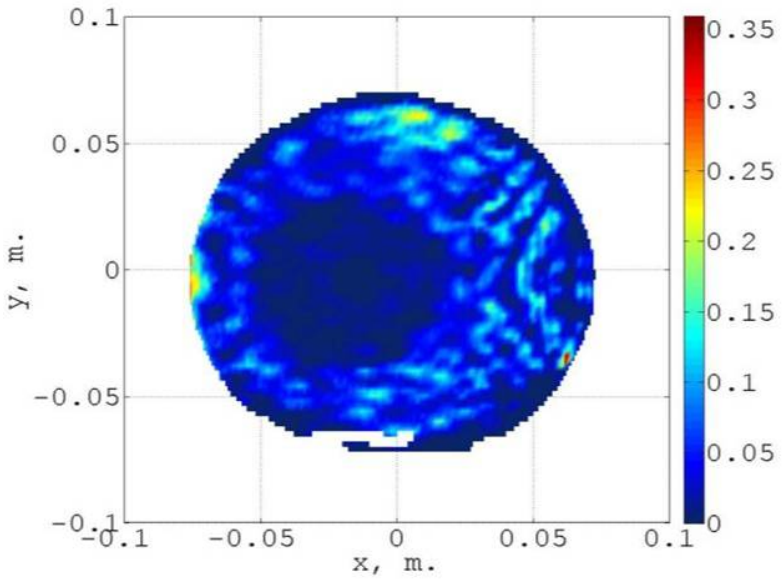

Figure 4.3: Reflectarray element efficiency evaluated with a method based on computational back-propagation from the measured PWS.

4.2 Beam patterns

The measured beam patterns for the manufactured reflectarrays are presented in Figs. 4.4-4.6. Scan plane was chosen to be 0.4×0.4 m^2 with the sampling interval of 2 mm. It locates at a distance of z=3 m from the AUT. The goal is to produce measurement results for beam width, beam direction and the side-lobe level and compare those with the simulated ones.

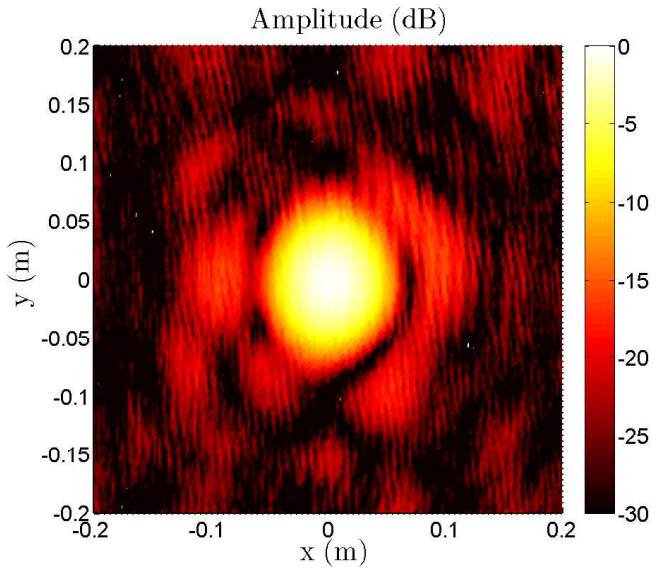

Figure 4.4: Beam pattern of RA#1.

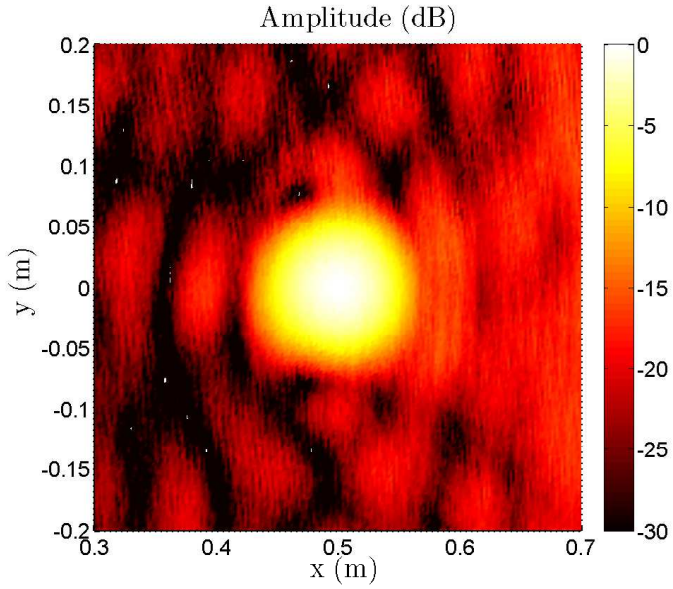

Figure 4.5: Beam pattern of RA#2.

When the beam pattern of RA#2 is examined, it shows that the specular reflection is clearly visible at the upper x-axis. The calculated maximum of the specular reflection lies at 1.5 m in the x-axis and thus it should not be visible at the scan plane of RA#2. The observed phenomena indicates that the element efficiency of the reflectarray is smaller than the designed (0.45-0.62), which means that about a one half of the radiated energy is in the direction of the main beam.

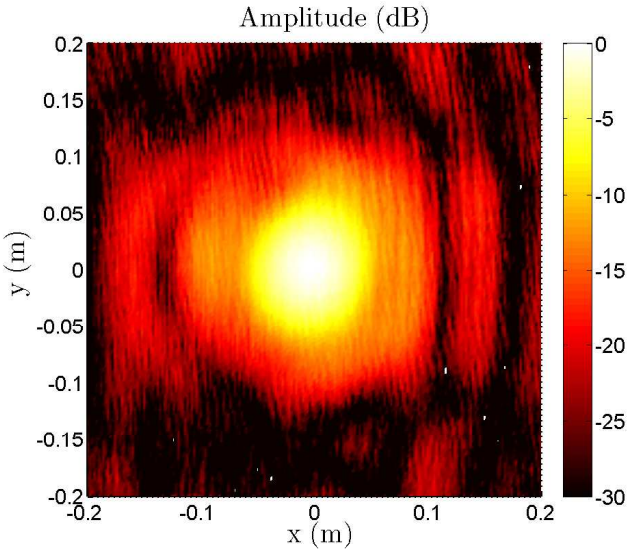

Figure 4.6: Beam pattern of RA#3.

For comparison, beam patterns were centered to the maximum of the main beam. In reality, the measured beam location differs from the designed one. The biggest deviation in position was 19 mm which means that the beam was tilted 0.36°. This is in the same order as the mechanical positioning uncertainty. For better illustration of the side-lobe level, horizontal and vertical cuts of the measured beam patterns are presented in Figs. 4.7 and 4.8.

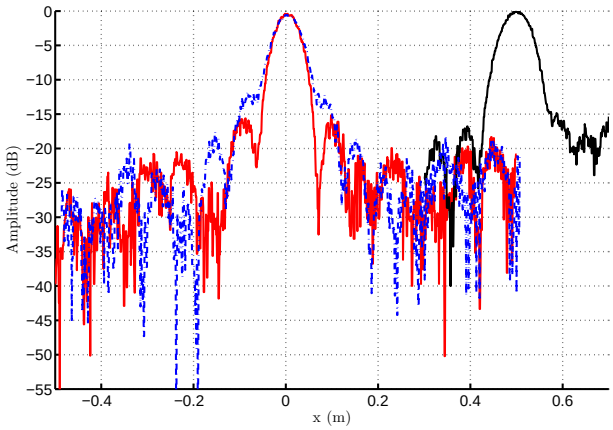

Figure 4.7: Horizontal cut of the measured beam pattern of (red) RA#1, (black) RA#2 and (blue) RA#3.

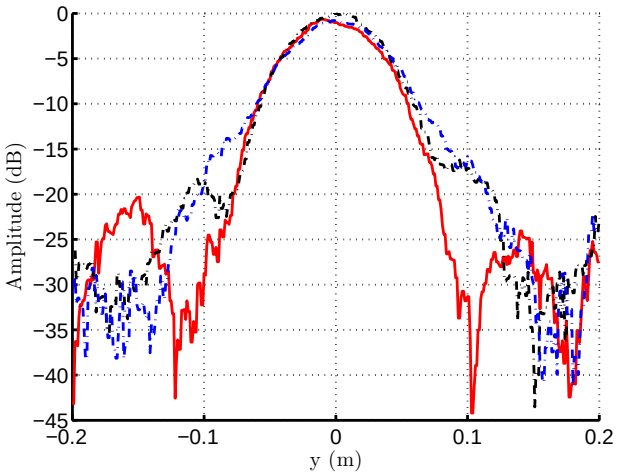

Figure 4.8: Vertical cut of the measured beam pattern of (red) RA#1, (black) RA#2 and (blue) RA#3.

When the measured beam patterns are compared to the simulated ones presented in Section 2.3.4, one can come to a conclusion that the beam shape and direction is in a close match with calculations but the level of the first side-lobes was up to 8 dB higher than designed depending on the type of the antenna. Key features of the measured beam patterns are listed in Table 3.

Table 3: Measured beam patterns of the fabricated reflectarrays

		3-dB Beam width		Side-lobe level		Main beam
		Measured	Simulated	Measured	Simulated	Deviation
RA#1	x	55 mm	58 mm	−14.8 dB	−19 dB	−2 mm
	y	64 mm	64 mm	−19.7 dB	−18 dB	17 mm
RA#2	x	67 mm	62 mm	−15.0 dB	−18 dB	14 mm
	y	64 mm	64 mm	−16.2 dB	−15 dB	−19 mm
RA#3	x	61 mm	60 mm	−11.2 dB	−16 dB	−2 mm
	y	68 mm	62 mm	−11.4 dB	−20 dB	−13 mm

4.3 Near-field measurement of the RA aperture field

Direct measurement at the distance of the focus point (RA#1 and RA#2) is a convenient way to determine characteristics of the main beam, but the result does not tell anything about the efficiency of the antenna. In all offset-fed reflectarrays, a notable amount of power is lost in the specular reflection. The phenomena is described in more detail in Section 2.3.2.

Reflectarray aperture field is measured at a $z_{RA} = -59\,\text{cm}$ distance from the AUT. The measurement grid is chosen to be $60 \times 46\ \text{cm}^2$ with the sample spacing of $\Delta_x = 1$

mm and $\Delta_y = 4$ mm, respectively. Note that in the vertical direction it exceeds the $\frac{\lambda}{2}$ sampling at 120 GHz. In the RA measurement this is not crucial since the level of specular reflection drops below -45 dB at the direction corresponding the vertical spatial frequency component of $|k_y| = \pm 0.75 \frac{\text{rad}}{\text{mm}}$, which according to Eq. (4.4), corresponds a 4-mm sampling interval.

The plane-wave spectrum of RA#1 is presented in Fig. 4.9. Rectangular grid is increased by the use of zero-padding introduced in Section 4.1.1. The measured field is transformed to a spatial domain by calculating the integral defined in Eq. (4.11) by using two-dimensional fast Fourier transform algorithm (fft2) in Matlab.

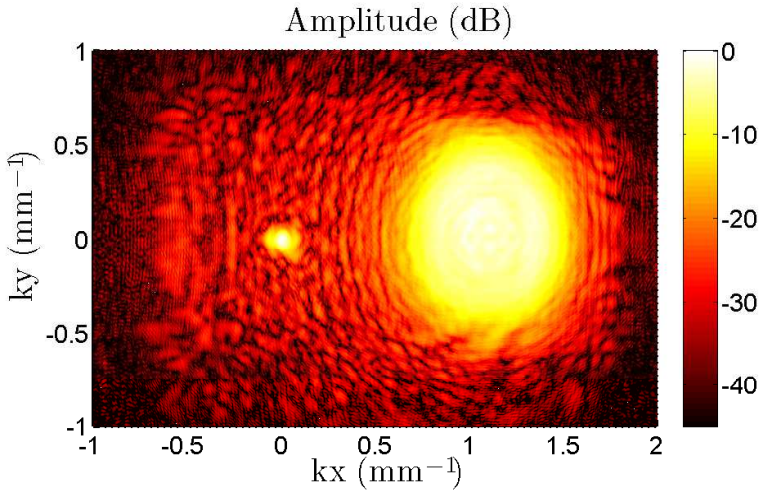

Figure 4.9: Plane-wave spectrum of RA#1 measured at 120 GHz.

The Fourier transform in Eq. (4.11) converts the RA aperture field in the k-space domain, where the direction of propagation is determined with spatial frequency components. In general, an angle space output corresponding to azimuth and elevation angles is more conventional manner of representation for far-field pattern. The angular spectrum of RA#1 can be calculated from the spatial domain result with Eqs. (4.12) and (4.13) by using two dimensional interpolation algorithm (interp2) in Matlab. The angular spectrum of RA#1 is presented in Fig. 4.10.

When examining the result, one can come in to a conclusion that a much higher amount than one half of the radiated energy is lost in the direction of the specular reflection. Manufactured reflectarrays are suffering from over etching since the measured gap width of the CPW-structure was almost twice the designed value. Since the resonant frequency of the CPA is determined with the effective length of the patch, this could be one of the main reasons why a considerable large amount of power is lost in the specular reflection instead of the focused main beam.

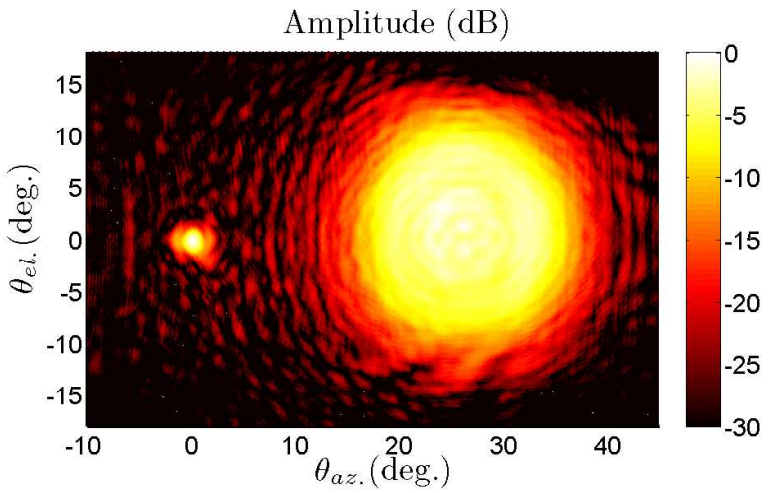

Figure 4.10: Angular spectrum of RA#1 measured with 120 GHz. The main beam lies at the antenna boresight direction, and the maximum of the specular reflection at azimuth direction of 25.6°.

4.3.1 Resonant frequency of the RA

Determination of the resonant frequency for over-etched patches is not a very straightforward procedure, although the resonance properties of a single element could be determined by an on-wafer measurement performed with a probe station. The result itself would not provide information about the level of specular reflection, and thus the effect to the modulation efficiency, which is in our interest.

However, a way to determine also the properties of specular reflection at once, is to perform a frequency sweep for the RA aperture field measurement. Despite the fact that the Gunn-oscillator transmitter significantly increases the dynamic range of the measurement, its major drawback is the inability to perform frequency sweeps. The measurement can still be performed with one point frequency at a time, although each frequency step would last several hours.

One way to overcome this problem is to measure only a wide horizontal cut for each frequency step, because the maximum of both main beam and the specular reflection locates in the xz-plane. Then, an angular spectrum is calculated for each cut separately and comparison between the main beam and the specular reflection is presented in Fig. 4.11. Note that this is not an accurate way to determine the angular spectrum of the RA, but gives a rough estimate, where the most efficient resonant properties should be looked for and the time-consuming planar near-field measurement is done only at the frequency of the observed maximum. An angular spectrum of RA#2 measured with the frequency of 132.7 GHz is presented in Fig. 4.12.

It can be noticed that the level of specular reflection is now at considerable lower

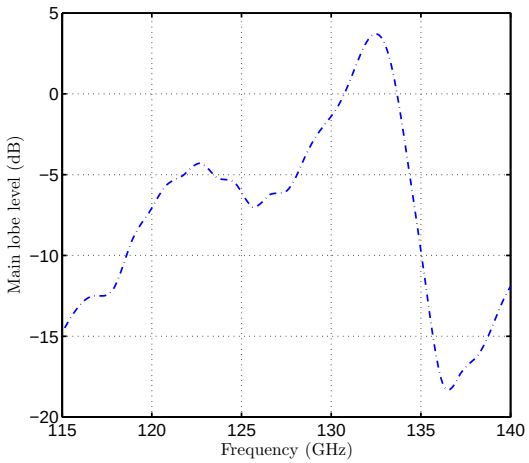

Figure 4.11: Suggestive comparison between the level of the main beam and the specular reflection in respect of frequency.

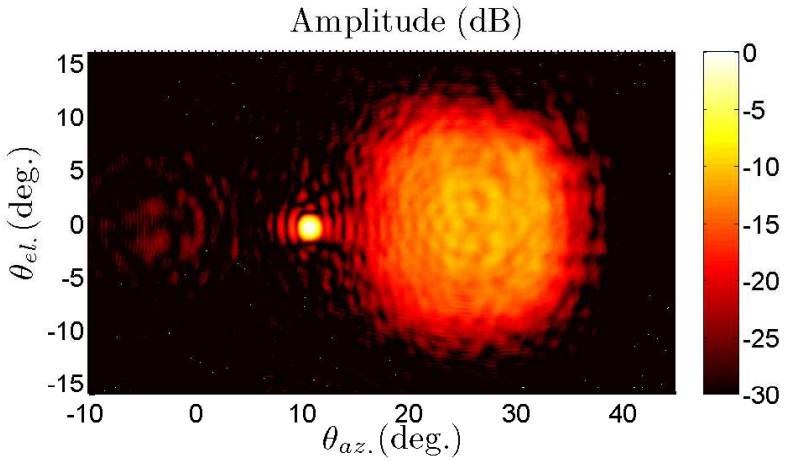

Figure 4.12: Angular spectrum of RA#2 measured with 132.7 GHz.

level than that seen in Fig. 4.10. Because the phasing of the elements is calculated for the 120-GHz central frequency, the azimuth direction of the main beam is now to 10.65° instead of the designed 9.46°.

For comparison, in Fig. 4.13, an azimuth cut of the angular spectrum for RA#1 and RA#3 measured at 120 GHz, and RA#2 at the observed resonant frequency of 132.7 GHz. Patterns are normalized to the specular reflection. It can be noticed that the main beam of RA#2 is now at a 7.4 dB to 8.7 dB higher level than those measured with the designed central frequency of 120 GHz. Since the RA element efficiency is determined by how the power is divided between the steered beam and the specular reflection, the over-etching of the antenna elements cased by manufacturing errors could be the main reason of observed decrease in RA efficiency. For clarification, the main beam of RA#2 is tilted off-broadside. Due to the projected aperture,

main beam directivity has a $\cos\theta$-dependence [7], which would mean a -0.15 dB gain reduction for 10° beam tilt. Thus, the tilted beam can be compared with the broadside ones.

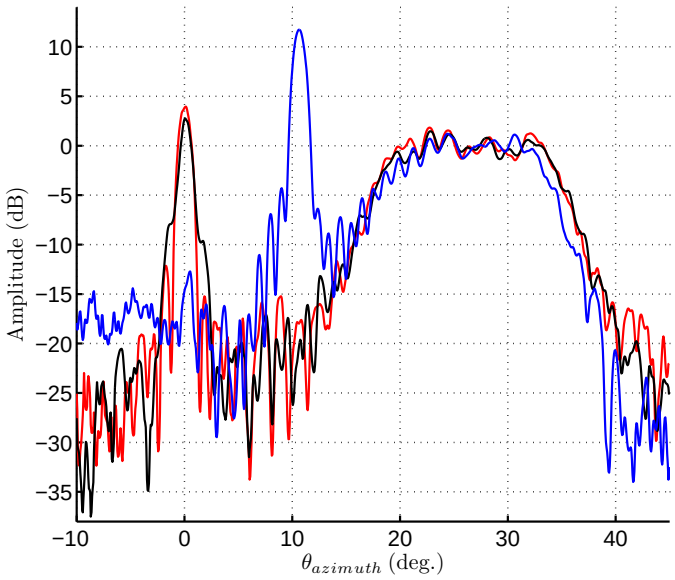

Figure 4.13: Azimuth cut ($\theta_{elevation} = 0$) of the PWS. RA#1 (black) and RA#3 (red) are measured at 120 GHz, RA#2 (blue) at 132.7 GHz.

4.4 Near-field measurements of the reflectarray surface

Reflectarray is measured at a $z_{RA} = -1$ mm distance from the RA surface. The measurement grid is chosen to be 50×50 mm^2 with the sample spacing of $\Delta = 0.2$ mm. The area incorporates 25×25 antenna elements, which is enough for statistical analysis. The first step is to measure the received field strength of the reflectarray surface, which is presented in Fig. 4.14. At this point, the representation is chosen to be in a complex plane, where the effect of each step in the parameter extraction from raw data is clearly visible.

In addition to the RA, calibration standards for short circuit, open-circuit and matched load are also measured in order to solve the calibration parameters a, b and c from Eqs. (3.7)-(3.9). The measured field strength is calibrated by using Eq. (3.6). The result is a reflection coefficient of the RA surface presented in Fig. 4.15. For clarification, the values of the measured calibration standards for short-circuit (circle), open-circuit (star), matched load (triangle), and OEWG-probe (x-mark) are shown in each step. The calibration procedure discussed further in detail in Section 3.1.

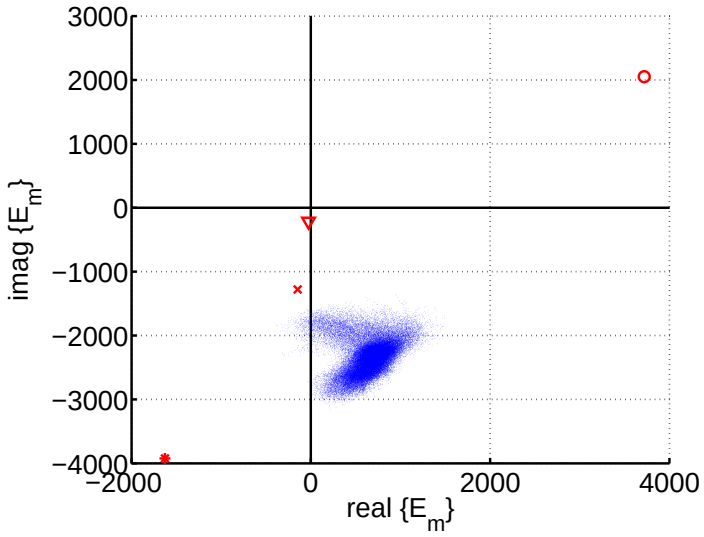

Figure 4.14: Received uncalibrated field strength data (blue dots) in complex plane from the near-field measurement of the reflectarray surface. Red-colored symbols for short-circuit (circle), open-circuit (star), matched load (triangle) and OEWG-probe (x-mark) are placed in the figure.

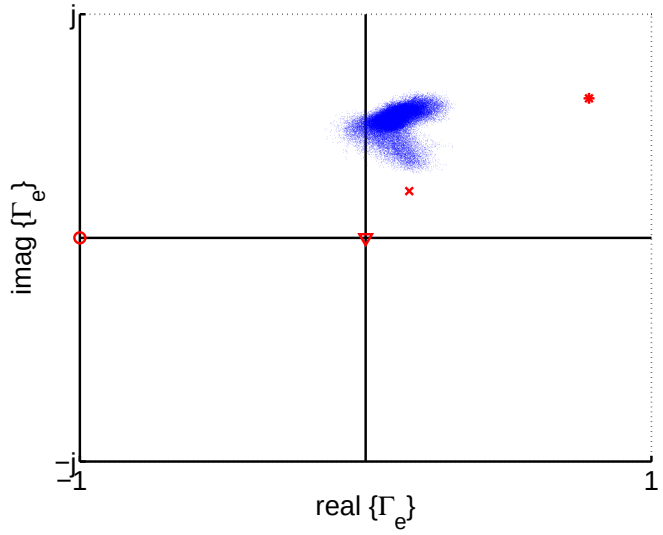

Figure 4.15: Calibrated reflection coefficient data (blue dots) of reflectarray elements and calibration standards (red symbols) in a complex plane.

The calibrated result includes an offset-component caused by the return loss of the OEWG-probe, the effect of which can be easily eliminated by subtracting the calibrated measurement result of the probe from the RA reflection coefficient. The calibrated and offset corrected result of the RA reflection coefficient is presented in Fig. 4.16.

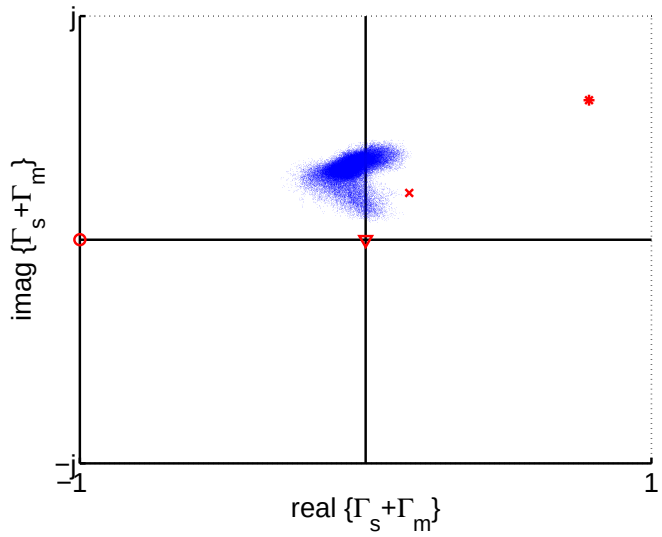

Figure 4.16: Calibrated and offset-corrected reflection coefficient data (blue dots) of reflectarray elements and calibration standards (red symbols) in a complex plane.

The next step is to separate the modulated field from the specular reflection. The specular component can be determined by measuring an equal-sized (to RA) copper plate reference in place of the AUT. However, this is a time-consuming method and does not take the curvature of the RA into account. Since the ground plane occupies 81.7% of the RA area, and the reflection coefficient of which is directly proportional to the measurement distance as described in Section 3.2.3, a more convenient way is extract the specular component by 2-D filtering of the offset-corrected reflection coefficient. Filtering algorithm can be improved to be based on perpendicular cuts and thus to be more rapid for reconfigurable reflectarray characterization. Fig. 4.17 represents a vertical cut of the phase and amplitude of the specular component determined by a filtering method.

Once the reflection coefficient of the specular component is determined for all points of the measurement grid, the effect of which can be subtracted from the data. The only parameter left is the reflection coefficient of the modulated field shown in Fig. 4.18. It has settled around the origin of the complex plane covering the full 360° phase range of the relative phase shift distribution.

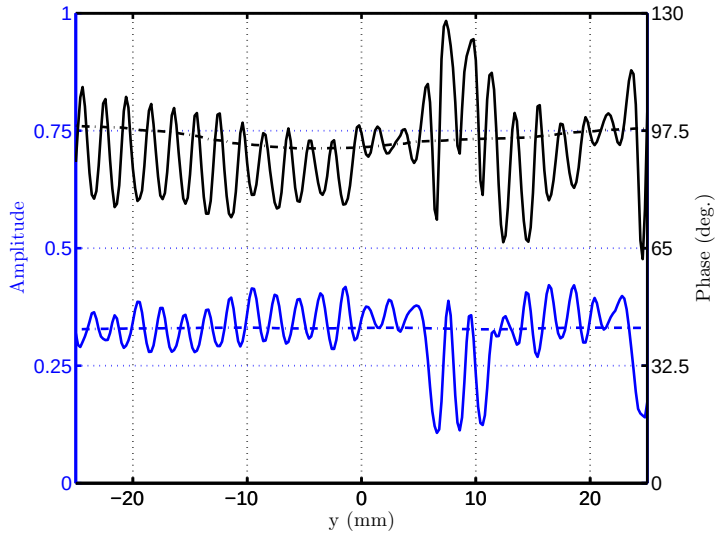

Figure 4.17: Amplitude (blue) and phase (black) of the specular reflection component in y-direction (x=0). Solid curves represent a vertical cut of the reflection coefficient data from Fig. 4.16 and dashed curves are calculated specular components for the cut.

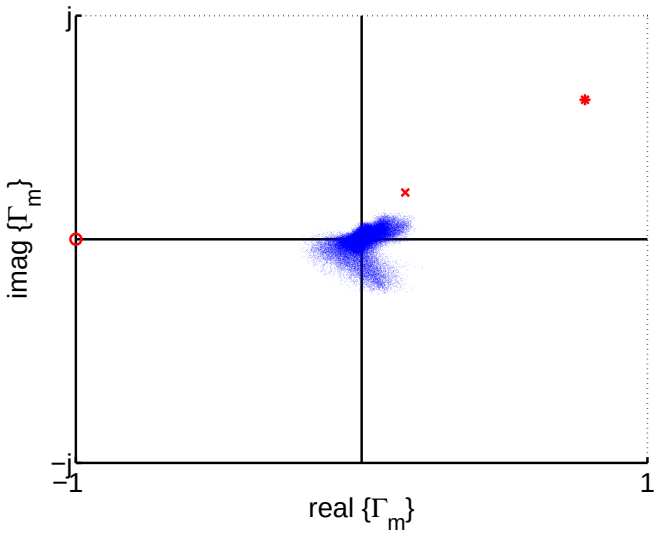

Figure 4.18: Complex plane representation of the calibrated, offset-corrected reflection coefficient data (blue dots) of the modulated field in RA elements.

4.4.1 Measured reflection coefficients

The reflection coefficient of the modulated field in the RA surface is represented in Fig. 4.19. When the result is compared with the calculated phase shift presented in Fig. 2.2, antenna elements with a different modulation can be clearly distinguished in both amplitude and phase. However, it can be noticed that the steps of the phase

quantization are varying from 20° to 190°. The designed phase step of 90° fulfills only between the open-ended 200 µm stub and the short-circuited 195 µm stub.

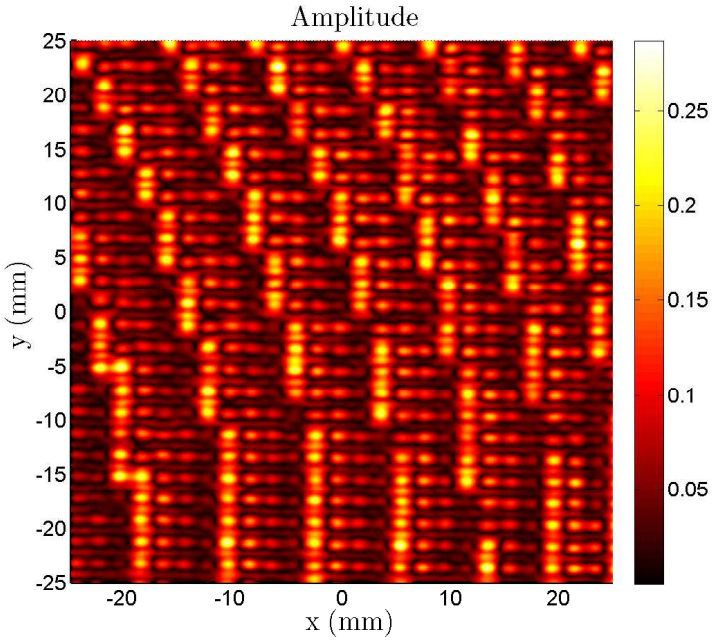

(a)

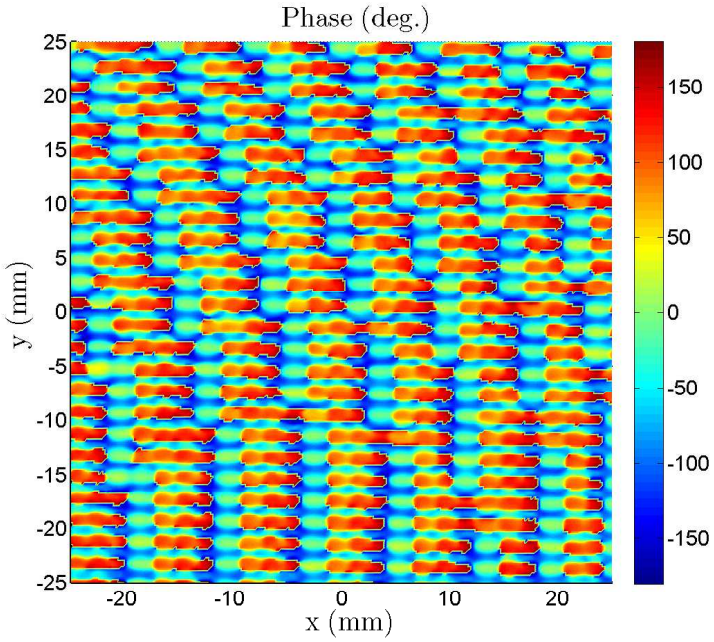

(b)

Figure 4.19: Amplitude (a) and phase (b) of the reflection coefficient calculated from the near-field measurement of the reflectarray surface.

4.4.2 Reflectarray element efficiency

Since the reflection coefficients for both specular and modulated field components are known for the whole measured area, the element efficiency shown in Fig. 4.20 can be calculated with Eq. (2.77).

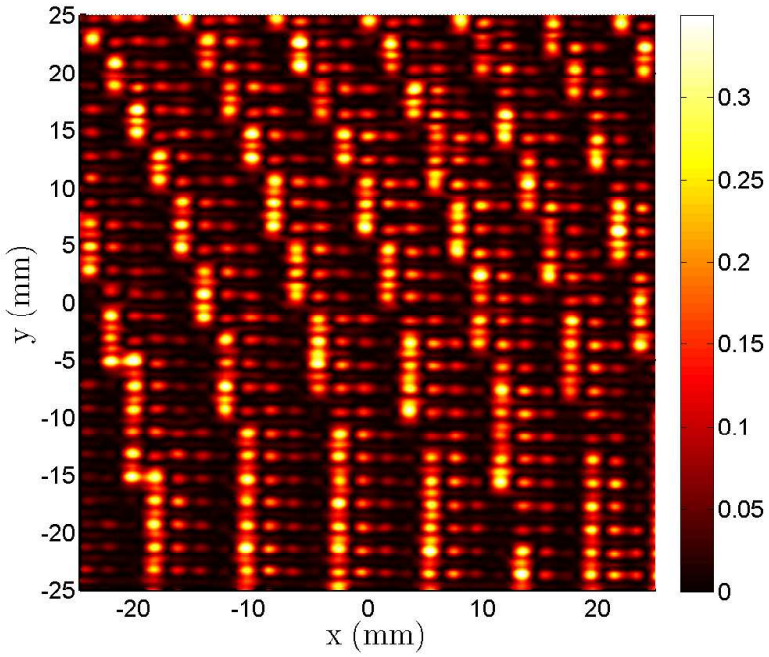

Figure 4.20: Reflectarray element efficiency measured with the proposed method.

The measured element efficiency is in a range of 0.02 to 0.20 depending on the length and type of the stub. The result is in line with one calculated by a method based on computational back-propagation presented in Fig. 4.3.

Table 4: Measured reflection coefficients

Coupling element		Simulated		Measured		
Stub length	Type	Efficiency	Phase shift	Amplitude	Efficiency	Phase shift
195 µm	open	0.45	0°	0.17±0.04	0.20±0.07	0.0±11.0°
366 µm	open	0.45	−90°	0.04±0.02	0.02±0.01	−197.0±22.4°
54 µm	short	0.62	−180°	0.10±0.02	0.08±0.04	−249.5±8.91°
200 µm	short	0.62	−270°	0.13±0.02	0.14±0.04	−268.4±9.3°

4.5 Measurement uncertainty

The value of the measurements of the antenna performance cannot be regarded as significant if their accuracy cannot be specified. The accuracy of the measurement depends on how various error sources propagate through the system. The result of a planar near-field measurement technique is exact if the following conditions are satisfied [40]:

- The electromagnetic field outside of the scan area is zero,
- The scanner positioning is infinitely accurate,
- The network analyzer is perfectly linear and free of noise,
- No multipath propagation occurs,
- The only coupling mechanism between the test and probe antennas is by free-space propagation (no evanescent coupling).

However, in a real-world antenna measurement, all of these conditions are violated to some extent, thus an error analysis is required. The most important factor of uncertainty in the near field antenna measurement is the dynamic range of the VNA or interferometer used in the measurement. Also additional error sources such as drift, scanner positioning errors, VNA stability, scan plane truncation, AUT alignment error, aliasing, RF leakage, IF leakage, and multipath reflections exist.

Dynamic range of the measurement scheme can be resolved in different ways. For measurements (i) and (ii) the signal-to-noise ratio is determined by comparing the levels of the main beam and the first sidelobes, to the noise level, which is measured by covering the transmitter and receiver with aluminum foil. In measurement (iii) signal and noise levels are evaluated by terminating the directional coupler with a short-circuit and with a matched load, respectively. The uncertainty in measured amplitude and phase due to electrical noise is calculated from the SNR [40]:

$$U_{amp.} = 20\log_{10}(1 \pm 10^{-\frac{SNR(dB)}{20}}), \tag{4.18}$$

$$U_{phase} = \arctan(\pm 10^{-\frac{SNR(dB)}{20}}). \tag{4.19}$$

The SNR for measurements (i) and (ii) typically varies from 40 dB to 60 dB, which corresponds the uncertainty of ± 0.01 dB to ± 0.1 dB in amplitude and of $\pm 0.06°$ to $\pm 0.57°$ in phase. However, the post-processing of the data is measurement (ii) increases the dynamic range, because the near- to far-field transform coherently sums all measurements into each output point [40]. The processing gain is proportional to the number of measurement points n:

$$G_p = 20\log_{10}(\sqrt{n}). \tag{4.20}$$

In measurement (iii), the dynamic range is from 32 dB to 37 dB, which gives the uncertainty from ±0.14 dB to ±0.34 dB in amplitude and of ±0.81° to ±1.44° in phase. Note that this is the uncertainty of the received field strength, not of the calculated reflection coefficient. Since the measured area contains various identical elements, the uncertainty of the reflection coefficient can be estimated by the standard deviation.

Amplitude and phase drift is significant source of error in long-lasting near-field measurements. It could be up to 0.37 dB and 5.5° (for RA#2 near-field measurement presented in Fig. 4.12) in a 6-hour 2-D measurement. However, since the 2-D scanning is performed one vertical cut at a time (and the drift can be assumed to negligible for a rapid cut), the drift can be compensated by measuring rapid horizontal cuts before and after as it is presented in Fig. 4.21.

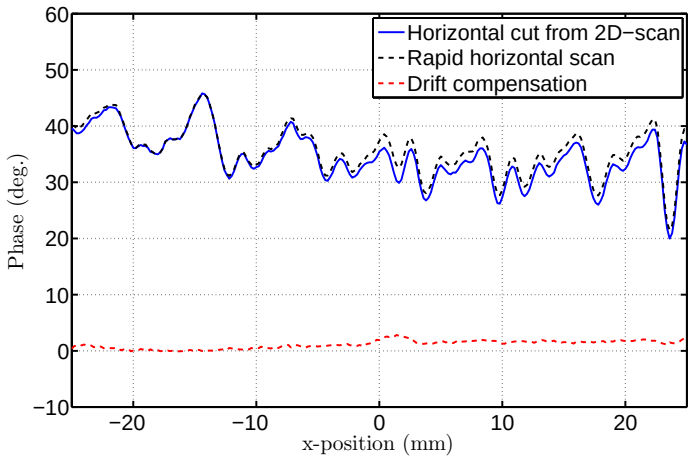

Figure 4.21: Phase drift compensation for a 4-hour reflectarray near-field measurement.

5 Summary and conclusions

In this thesis, the operation principle, design considerations and measurements of a 120-GHz reflectarray antenna are presented. The thesis is a part of a work towards a millimeter wave radar for imaging an identification applications. The fundamentals of millimeter-wave reflectarray antenna design and analysis are described in detail followed by introducing the operation principle and the main characteristics of the manufactured static reflectarrays.

A reflection measurement scheme for characterization of individual antenna elements in the reflectarray has been developed. To compensate the effect of the directional coupler used in the scheme, a precise calibration procedure was introduced. It enables a parameter extraction from the measurement data and relates the measured electric field to the actual reflection coefficient of the antenna element. Functionality of manufactured reflectarrays in a larger scale was verified in the near-field measurement range, where both beam pattern and aperture field were measured.

The measured beam direction of fabricated reflectarrays is within 0.5° from the desired, which is in the same order as the estimated mechanical positioning inaccuracy. The measured beam patterns are in a close match with calculations in respect of -3 dB beam width and shape. However, the level of the first side-lobes is up to 8 dB higher than the calculated one.

The element efficiency in offset-fed reflectarrays is determined by how the energy is divided between the steered beam and the specular reflection. In the near-field measurements of the reflectarray aperture field, the presence of a strong specular component was observed, which decreases the element efficiency. The manufactured reflectarrays found out to be suffering from over etching, as the measured gap width (15.5 µm) of the CPA was almost twice the designed value of (8 µm). It decreases the effective length of the patch which indicates that the resonant frequency of the RA is higher than designed. Thus, a significant amount of power is lost due to frequency mismatch. By performing a frequency sweep for a horizontal cut and comparing the levels of the main beam and the specular reflection in the plane-wave spectrum, reflectarray resonance frequency can be estimated to be 132.7 GHz. An angular spectrum of the planar near field measured at this frequency verifies that the level of the main beam is increased 7.4 dB to 8.7 dB compared to ones measured with the designed central frequency of 120 GHz.

The proposed measurement method for near-field imaging of the reflectarray surface proved to be sufficient for distinguishing the differently tuned elements from the adjacent ones in both amplitude and phase. In the measured reflection coefficients, the phase interval of the elements varies from 20° to 190° and the designed one, 90° is reached only with open-ended 195-µm stub and short-circuited 200-µm stub. The measured element efficiency is in a range of 0.02 to 0.20 depending on the length and the type of the stub. The result is in line with one calculated by a method based on

computational back-propagation from the plane-wave spectrum of the reflectarray aperture field. The method can be implemented for characterization of reconfigurable reflectarrays by improving the determination of the specular component for rapid calculations.

To our best knowledge the reflectarray presented here is the first operating one at such high frequency. The experimental results presented here and in [12] are in a reasonable agreement with calculations. The problems in the manufacturing process were identified and by further improvements, the reflectarray is suitable for adaptive beam steering by replacing the static phase shifting stubs with reconfigurable MEMS phase shifters.

References

[1] S. Hum, M. Okoniewski, and R. Davies, "Modeling and design of electronically tunable reflectarrays," *IEEE Transactions on Antennas and Propagation*, vol. 55, pp. 2200–2210, Aug. 2007.

[2] J. Huang and J. Encinar, *Reflectarray Antennas*. Piscataway, NJ: Wiley-IEEE Press, 2008.

[3] D. Pozar, S. Targonski, and R. Pokuls, "A shaped-beam microstrip patch reflectarray," *IEEE Transactions on Antennas and Propagation*, vol. 47, pp. 1167–1173, Jul. 1999.

[4] D. Berry, R. Malech, and W. Kennedy, "The reflectarray antenna," *IEEE Transactions on Antennas and Propagation*, vol. 11, pp. 645–651, Nov. 1963.

[5] J. Huang, "Capabilities of printed reflectarray antennas," in *IEEE International Symposium on Phased Array Systems and Technology*, Oct. 1996, pp. 131-134.

[6] D. M. Pozar, "Bandwidth of reflectarrays," *Electronics Letters*, vol. 39, pp. 1490–1491, Oct. 2003.

[7] D. Pozar, S. Targonski, and H. Syrigos, "Design of millimeter wave microstrip reflectarrays," *IEEE Transactions on Antennas and Propagation*, vol. 45, pp. 287–296, Feb. 1997.

[8] M. Hajian, A. Coccia, and L. Ligthart, "Design, analysis and measurements of reflected phased array microstrip antennas at ka-band using passive stubs," in 1^{st} *European Conference on Antennas and Propagation*, Nov. 2006, 5p.

[9] S. Targonski and D. Pozar, "Analysis and design of a microstrip reflectarray using patches of variable size," in *Antennas and Propagation Society International Symposium*, vol. 3, June 1994, pp. 1820-1823.

[10] R. Jedlicka, M. Poe, and K. Carver, "Measured mutual coupling between microstrip antennas," *IEEE Transactions on Antennas and Propagation*, vol. 29, pp. 147–149, Jan. 1981.

[11] R. Mailloux, *Phased Array Antenna Handbook*. Boston, MA: Artech House, 1994.

[12] A. Tamminen, S. Mäkelä, J. Ala-Laurinaho, J. Häkli, P. Koivisto, P. Rantakari, J. Säily, A. Luukanen, and A. V. Räisänen, "Reflectarray design for 120-GHz radar application: measurement results," *IEEE Transactions on Antennas and Propagation*, vol. 61, pp. 5036–5047, Oct. 2013.

[13] I. Lindell and K. Nikoskinen, *Antenniteoria*. Helsinki, Finland: Oy Yliopistokustannus/Otatieto, 1995.

[14] Y. Huang and K. Boyle, *Antennas: from Theory to Practice*. Chichester, United Kingdom: John Wiley & Sons Ltd., 2008.

[15] A. E. H. Love, "The integration of the equations of propagation of electric waves," *Proceedings of the Royal Society of London*, vol. 68, no. 442-450, pp. 19–21, 1901.

[16] W. L. Stutzman and G. A. Thiele, *Antenna Theory and Design*. Hoboken, NJ: John Wiley & Sons Ltd., 1982.

[17] A. Tamminen, "Developments in imaging at millimeter and submillimeter wavelengths," *D. Sc. dissertation, Department of Radio Science and Engineering, Aalto University School of Electrical Engineering, Espoo, Finland*, 2011.

[18] K. Li, C. Cheng, T. Matsui, and M. Izutsu, "Coplanar patch antennas: principle, simulation and experiment," in *IEEE Antennas and Propagation Society International Symposium*, vol. 3, July 2001, pp. 402-405.

[19] A. Tamminen, J. Ala-Laurinaho, J. Häkli, P. Koivisto, J. Säily, A. Luukkanen, and A. V. Räisänen, "Reflectarray design for 120 GHz MMID application: simulation results," in *6th ESA Workshop on Millimetre Wave Technology and applications, Espoo, Finland*, May 2011.

[20] W. Hu, M. Arrebola, R. Cahill, J. Encinar, V. Fusco, H. Gamble, Y. Alvarez, and F. Las-Heras, "94 GHz dual-reflector antenna with reflectarray subreflector," *IEEE Transactions on Antennas and Propagation*, vol. 57, pp. 3043–3050, Oct. 2009.

[21] R. Sorrentino, R. Gatti, and L. Marcaccioli, "Recent advances on millimetre wave reconfigurable reflectarrays," in 3^{rd} *European Conference on Antennas and Propagation*, Mar. 2009, pp. 2527-2531.

[22] J. Greiser, "Coplanar stripline antenna," *Microwave Journal*, vol. 19, pp. 47–49, Oct. 1976.

[23] K. Li, C.-P. Chen, T. Anada, and T. Matsui, "Electric field in coplanar patch antenna (CPA) - simulation and measurement," in *Proceedings of Asia-Pacific Conference Microwave Conference*, vol. 1, Dec. 2005, 4p.

[24] K.-H. Oh and J.-I. Song, "Investigation of parallel plate mode suppression in UC-PBG FW-CBCPW by using a transient electro-optic field-mapping," in *International Topical Meeting on Microwave Photonics*, Oct. 2005, pp. 277-280.

[25] S. Mäkelä, A. Tamminen, J. Ala-Laurinaho, A. Räisänen, P. Koivisto, J. Säily, J. Häkli, P. Rantakari, R. Tuovinen, and A. Luukanen, "Near-field measurements of a millimeter-wave reflectarray at 120 GHz," in *Proceedings of the* 42^{nd} *European Microwave Conference, Amsterdam, The Netherlands*, Oct. 2012, pp. 807-810.

[26] S. Mäkelä, A. Tamminen, J. Ala-Laurinaho, A. Räisänen, P. Koivisto, J. Säily, J. Häkli, P. Rantakari, R. Tuovinen, and A. Luukanen, "Calibration method for near-field measurement used in reflectarray characterization," in *Proceedings of the* 43^{nd} *European Microwave Conference, Nuremberg, Germany*, Oct. 2013, 4 p.

[27] S. Dieter and W. Menzel, "High-resolution probes for near-field measurements of reflectarray antennas," *IEEE Antennas and Wireless Propagation Letters*, vol. 8, pp. 157–160, Jan. 2009.

[28] J.-D. Lacasse and J.-J. Laurin, "A method for reflectarray antenna design assisted by near field measurements," *IEEE Transactions on Antennas and Propagation*, vol. 54, pp. 1891–1897, June 2006.

[29] R. Clarke, R. Pollard, N. Ridler, M. Salter, and A. Wilson, "Traceability to national standards for s-parameter measurements of waveguide devices from 110 GHz to 170 GHz," in 73^{rd} *Microwave Measurement Conference*, June 2009, 10p.

[30] H. Rajagopalan and Y. Rahmat-Samii, "Reflectarray antennas: An intuitive explanation of reflection phase behavior," in 30^{th} *General Assembly and Scientific Symposium*, Aug. 2011, 4p.

[31] K. Silvonen, "New algorithms for network analyzer, test fixture and wafer prober calibration," *ACTA POLYTECH. SCAND. ELECTR. ENG*, no. 95, 1999.

[32] R. F. Bauer Jr. and P. Penfield, "De-embedding and unterminating," *IEEE Transactions on Microwave Theory and Techniques*, vol. 22, pp. 282–288, Mar. 1974.

[33] A. Räisänen and A. Lehto, *Radiotekniikan perusteet.* Helsinki, Finland: Oy Yliopistokustannus/Otatieto, 2003.

[34] B. Bianco, A. Corana, S. Ridella, and C. Simicich, "Evaluation of errors in calibration procedures for measurements of reflection coefficient," *IEEE Transactions on Instrumentation and Measurement*, vol. 27, pp. 354–358, Dec. 1978.

[35] A. Lehto and A. Räisänen, *Mikroaaltomittaustekniikka.* Helsinki, Finland: Oy Yliopistokustannus/Otatieto, 1992.

[36] W. Wiatr, "Line-length optimization of offset-short standards for broadband VNA calibration," in 18^{th} *International Conference on Microwave Radar and Wireless Communications*, June 2010, 4 p.

[37] S. Dieter, Z. Yang, and W. Menzel, "A 77 GHz near-field probe with integrated illuminating waveguide," in *German Microwave Conference*, Mar. 2011, 4 p.

[38] M. D. Weiss, B. Zadler, S. Schafer, and J. Scales, "Near field millimeter wave microscopy with conical teflon probes," *Journal of Applied Physics*, vol. 106, pp. 044912–044912–8, Aug. 2009.

[39] D. M. Pozar, *Microwave Engineering,* 4^{th} *Edition.* Hoboken, NJ: John Wiley & Sons Ltd., 2011.

[40] D. Slater, *Near-Field Antenna Measurements.* Norwood, MA: Artech House, Inc., 1991.

[41] C. A. Balanis, *Antenna Theory, Analysis and Design,* 3^{rd} *Edition.* Hoboken, NJ: John Wiley & Sons Ltd., 2005.

A Publication I

S. Mäkelä, A. Tamminen, J. Ala-Laurinaho, A. V. Räisänen, P. Koivisto, J. Säily, J. Häkli, P. Rantakari, R. Tuovinen, and A. Luukanen, "Near-field measurements of a millimeter-wave reflectarray at 120 GHz," in *Proceedings of the 42nd European Microwave Conference*, Amsterdam, The Netherlands, 29-30 October 2012, pp. 807-810.

Near-Field Measurements of a Millimeter-Wave Reflectarray at 120 GHz

S. Mäkelä, A. Tamminen, J. Ala-Laurinaho and A. V. Räisänen
MilliLab and SMARAD, Department of Radio Science and Engineering Aalto University
Espoo, Finland
sampo.makela@aalto.fi

P. Koivisto, J. Säily, J. Häkli, P. Rantakari, R. Tuovinen, and A. Luukanen
Millilab, VTT Technical Research Centre of Finland
Espoo, Finland

***Abstract*—In this paper, we describe the near-field measurements of the surface of a 120 GHz reflectarray. The reconfigurable offset-fed reflectarray under development consist of approximately 3700 coplanar patch antenna elements which are individually controlled by 4-state micro-electro-mechanical (MEMS) phase shifters. Measurements of a static reflectarray preceding the MEMS-controlled one are done in order to characterize the behavior of individual antenna elements of the reflectarray. Measurement setup, probe selection and the effect of the directional coupler are described. Amplitude and phase patterns of the reflectarray are shown. Also the main characteristics of the static reflectarray under test are presented.**

Keywords- antenna measurements; millimeter-wave; reflectarray; near-field-probe measurements

I. INTRODUCTION

A reflectarray antenna is used to replace the conventional reflector antenna or phase-controlled antenna array. Its operation principle resembles a parabolic reflector antenna and it uses similar feeding structures. Advantages of the reflectarray compared to the conventional reflector antenna are thin planar structure and the possibility to form various beam patterns with simple radiating elements, for example with microstrip patches [1]. Reflectarray antennas are typically manufactured with lithographic process which keeps the manufacturing costs low, at least when producing large quantities [2]. Since the reflectarray uses a spatial feed, lossy RF-feed network is not needed. Therefore, reflectarray antennas could achieve high efficiency and gain compared to phased arrays. The efficiency of the reflectarray antenna is nevertheless bounded due to illumination spillover, material losses, and phase errors. Also the modulation efficiency must be taken into account. The most significant weaknesses of the reflectarray could be considered to be the limited bandwidth, which occurs from the narrow bandwidth of the microstrip antenna elements and the phase delay inflicted by spatial feed [1, 3].

A reconfigurable 120-GHz reflectarray antenna is being developed at Aalto University Department of Radio Science and Engineering and at VTT (Technical Research Centre of Finland). The reflectarray will consist of approximately 3700 microstrip-based antenna elements similar to the coplanar patch antenna (CPA) presented in [4]. Antenna elements will be coupled with MEMS phase shifters, which can be individually controlled to create the desired beam. The element spacing is 2 mm which allows beam steering up to 38 degrees from normal [2]. Because the state of the MEMS phase shifters can be rapidly changed, it makes real-time scanning for video imaging applications or millimeter wave identification (MMID) possible. For electronic beam steering also the pin-diodes are used for antenna element tuning but they are consired to be too lossy at the frequency range above 100 GHz [1].

Near-field probing of the individual antenna elements of the reflectarray came into consideration in order to study reasons for the observed decrease in the modulation efficiency of the antenna elements. According to simulations presented in [2], the modulation efficiency should be above 0.5. It means that the field strength of the specular reflection should be at a lower level than the modulated field.

Near field probing of a 30-GHz 16-element reflectarray surface has been presented in [5]. Measurements have been made with different types of high resolution near-field probes. In this paper, the near-field-probe measurement is applied for studying the behavior of the antenna elements of the developed reflectarrays at 120 GHz.

II. STATIC REFLECTARRAY FOR MMID APPLICATION

The reflectarray is designed to be illuminated with Gaussian beam which is created by a corrugated horn antenna. The feed structure is located at position of (x = −150 mm, y = 0, z = 300 mm), when the origin is at the center of the reflectarray. A corrugated horn antenna has good electrical characteristics for Gaussian beam forming. It produces extremely spherically symmetric beam which has low sidelobe and cross polarization levels although the antenna has considerably wide bandwidth.

Before designing the final, reconfigurable reflectarray, three static reflectarray wafers have been manufactured for measurements. These antennas are focused to three different focus points. The focus point in two of them is at boresight direction, first one at 3 m and the second one at 3 km. The third one is focused 0.5-m off-boresight at 3-m distance [1].

Antenna elements of these static reflectarrays are coupled with both open-ended and short-circuited stubs with various lengths for discrete 4-state phase shift generation. Coupling is needed for two reasons. Because of the planar aperture of the reflectarray the path length difference from the spatial feed

This work has been partially supported by Tekes the Finnish Agency for Technology and Innovation through SIMIDS project, and by the Academy of Finland under the Centre of Excellence in Research Programme.

antenna to each element must be compensated by relative phase shift for each individual antenna element. In parabolic reflectors, this problem is solved by unique curvature of the dish. The other reason for coupling the antenna elements separately is an opportunity to steer the beam to the desired location [2]. This obviously requires reconfigurable phase shifters. Computation of the required relative phase shift for each element is done with a genetic algorithm (GA) developed in house. Fig. 1 shows the calculated relative phase shift for boresight-focused (to 3 m) reflectarray [2].

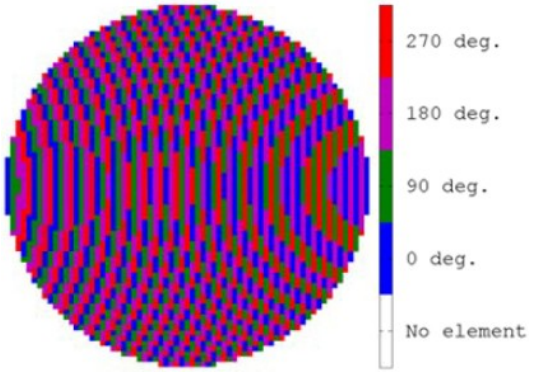

Figure 1. Relative phase shift of the static reflectarray (focused to 3 m, boresight direction) calculated by GA. [2]

Tuning elements are connected to the antennas with grounded coplanar waveguide (GCPW) transmission lines which are used with MEMS-phase shifters in the future. The major issue with GCPWs is the unwanted wave mode creation [6]. Although the desired CPW-mode must propagate without notable attenuation, generation of most dominating unwanted wave mode, parallel-plate-mode, must be prevented to maintain the sufficient efficiency of the antenna element. For the static reflectarrays, leakage of power to the substrate between the parallel ground planes is prevented by surrounding the each coupled antenna element with grounding vias which can be seen in Fig. 2. Physical dimensions of the patch antenna element needs to be changed depending from the distance to the via structure. The via pattern and antenna dimensions are optimized with simulations.

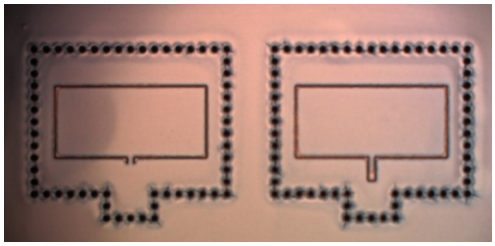

Figure 2. Microscope image of the static reflectarray antenna elements. 64 µm short-circuited stub (left) represents relative phase shift of 0° and the 195 µm open stub on the right, 90°, respectively. Vias are shown in black around the antenna

III. Measurements of the Reflectarray Surface With Millimetre Wave Network Analyzer

Analysis of the single antenna element in reflectarray is possible with advanced simulation tools by creating infinite array with periodic boundary conditions. Simulation results can be verified with near field probe measurements for characterizing behavior of the individual elements a fraction of a wavelength apart from the surface of the reflectarray antenna [5].

A. Near-field Probe Selection

Various types of probes can be used for near field millimeter-wave imaging. The simplest solution is to use open-ended waveguide (OEWG) as a receiving antenna, although it can at its best reach for a slightly below one wavelength resolution. However the performance of a waveguide can be improved by filling it with a dielectric material, for example sapphire rod [5]. The rod is shaped in such a way that outside of the waveguide is a sharp tip of the rod where the field is focusing. Dimensions can be optimized with simulation tools for a specific frequency.

Another option is to use conical antennas filled with dielectric material, for example corrugated conical horn antenna which is used as a feed antenna for the reflectarray. The dielectric probe could be manufactured from Teflon, Rexolite or other easily machined material and the achieved beam depends on its dimensions and dielectric characteristics. Because of the spherically symmetric shape of the conical probes, the resolution is nearly the same in every direction unlike in rectangular-waveguide-based probes. In [7], conical Teflon probe have been designed for millimeter wave near field imaging.

Two different near-field probes have been designed for measuring the surface of the reflectarray. First one is an open ended WR-6 waveguide which is filled by a sapphire rod. The second one is similar to the probe illustrated in [7] but instead of Teflon the probe is made from Rexolite and dimensions have been optimized for 120-GHz frequency. Both of these probes worked well in the simulations but did not achieve the performance of an open-ended waveguide in a resolution test measurements. Although both of the designed probes focused the beam sufficiently, power leakage before the tip of the probe causes unwanted illumination of the adjacent elements. Also, the measurement setup alone is fairly complicated and the increased number of multiple reflections from the dielectric material interfaces makes the system more difficult to calibrate. Therefore, open-ended WR-6 waveguide is chosen for measurements presented here.

B. The Measurement Setup

Measurement method presented in [5] cannot be directly implemented to our 120-GHz reflectarray. At first, the separate illumination is not possible because the receiver probe would obscure the line-of-sight propagation path since it is located about 1 mm away from the surface. Secondly, the structure of our reflectarray is notably different. Modulation of the 30-GHz reflectarray is carried out with patches of variable size and the antenna does not contain a ground plane at the surface. One of the main challenges in our measurement is separating the modulated field from the field reflected from the surrounding ground plane.

Because a separate feed cannot be used for reflectarray illumination, measurement is performed by using a waveguide directional coupler for measurement of the scattering parameter S_{11} from the reflectarray surface. The directional coupler is fed with a millimeter wave network analyzer (MVNA). Tunable local oscillator produces a stable microwave signal which is multiplied to a 120-GHz millimeter wave signal. The multiplier output and open-ended waveguide probe is connected to the through path of the directional coupler. The sample taken from the reflected field received by the probe is mixed back to microwave frequency for the receiver of the MVNA. Besides the reflected field, also the part of the transmitted field is leaking straight to the receiver due to reflection from the probe and unideality of the directional coupler. Measurements were repeated by replacing the multiplier of the transmitter with a Gunn-oscillator to achieve more dynamic range for the measurement. Due to high mm-wave output power (about 32 mW@120 GHz) of the Gunn oscillator, waveguide attenuator was used because the received signal would otherwise be cut at the receiver amplifier.

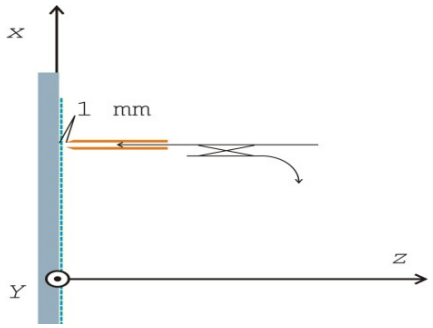

Figure 3. The measurement setup.

Reflectarray scanning is performed in such a way that the measurement probe stands still and the reflectarray is attached in a precise scanner which moves the antenna in the XY-plane and reads the corresponding amplitude and phase values from MVNA. The measurement setup is presented in Fig. 3. Distance between the reflectarray surface and open-ended waveguide probe is chosen to be about 1 mm for the whole reflectarray scan. According to simulations, the resolution of the measurement improves slightly when probe is located closer to the antenna surface.

C. *Effect of the Directional Coupler and Reflectarray Tilt-correction*

As mentioned above, part of the transmitted field is leaking straight to the receiver in the directional coupler. Influence of this leaking field can mostly be eliminated from the measurement results. That is because the transmitted field has a stable amplitude and phase, also the sampled leaked wave acts like a stationary vector which can be subtracted from the measurement data. Besides the scanning of the reflectarray, free-space measurement has also been performed, thus the offset-component can be calculated by averaging all the free space points of the measurement data.

Analysis of the near-field surface scan reveal that the reflectarray was slightly tilted in the horizontal direction during the measurements. Variation of the measurement distance has a significant influence to the results and has to be corrected. Correction has been done by horizontal cuts which has been measured between the antenna elements because the reflected field from the ground plane should be almost identical for both amplitude and phase when the distance between probe and the surface of the reflectarray does not vary. The curves of the cuts are filtered to get the correction factor for amplitude and relative phase shift due to tilt of the reflectarray. These fitting curves shown in Fig. 5 are used to reduce the effect of the variation of the measurement distance. Besides the reflectarray was slightly tilted, the non-linear phase-curve in Fig. 5 indicates that the antenna is slightly concave due to polyimide substrate fabrication process. Measurements verified that the center of the reflectarray is at 0.3 mm lower level than the edge which is truly significant compared to the wavelength.

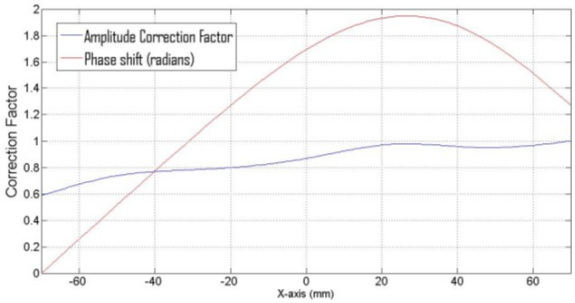

Figure 4. Phase and amplitude correction curves (y=0) of a slightly tilted reflectarray.

One problem with the correction method presented above is that the ground plane reflection could not be completely distinguished from the interference of the nearby antenna elements, especially between the elements at the horizontal direction where the resolution of the OEWG is weaker. For better ground plane reference, one copper plated wafer was produced. It is fabricated alike the reflectarray antennas, but without etching of the antenna elements. Copper plate was measured from the same distance as the reflectarray scan was performed. When the probe was moved farther away from the surface, rapid changes in phase of the received field was noticed at a specific distances. It indicates that the multiple reflections between the probe and the copper plate are decreasing the accuracy of the measurements although its effect can be reduced by subtracting the received field of the copper plate scanned from the same distance from the measurement results.

IV. RESULTS

A. *The Whole Reflectarray Antenna Surface Scan*

Scan interval is chosen to be 1 mm, two times the element spacing (2 mm). Amplitude and phase information of the near-field-probe measurements are shown in Fig. 5. When comparing the measurement results to the designed relative phase shift (Fig. 1), it is noticed that the amplitude of individual elements is varying in relation of the relative phase shift. Different amplitude values can partly be explained due to different modulation efficiency between the short-circuited and

open-ended tuning elements according to simulation results in [2].

It seems that the reflectarray tilt-correction shown in Fig. 4 is working well for the amplitude values, hence the amplitude of the reflected field from the ground plane varies only slightly. The measured phase is obviously more sensitive for the variation of the measurement distance, although the similar phase patterns as in Fig. 5 can be found when examining only small areas of the array. Therefore it is expected that we can actually distinguish the modulated field of every individual element from the ground plane reflection in both amplitude and phase. The main reason for the whole reflectarray scan performed was not to actually get accurate and comparable values of the individual elements but to roughly determine the functionality of the antenna.

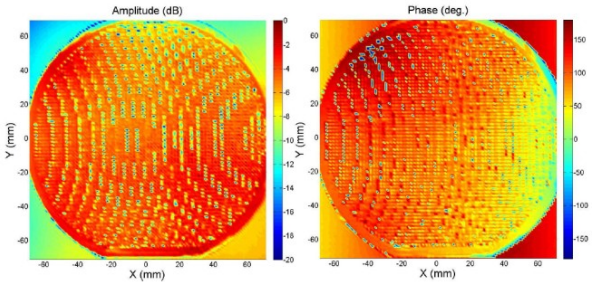

Figure 5. Amplitude(left) and phase(right) of the whole reflectarray near-field surface scan.

B. 20x20 Elements scan

As mentioned, the resolution of the measurement improves slightly when the measurement distance is chosen to be smaller. The reflectarray curvature due to 50-µm polyimide substrate fabrication is less significant when examining only small areas of the array. Other reason for the smaller scan area selection is to avoid the drift of amplitude and phase during scan and scan interval could be decreased to avoid quantization errors. In Fig. 6, amplitude and phase pattern of a 0.5-m aside focused (to 3 m distance) reflectarray are presented. Measurement distance was chosen to be about 0.2 mm where the phase-response of the received field was satisfactory, when the distance from the ground plane slightly changed.

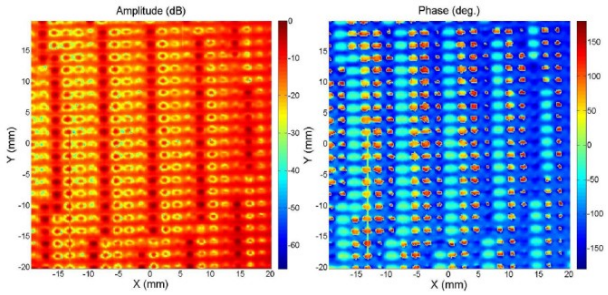

Figure 6. Amplitude (left) and phase(right) of 20x20 elements near-field surface scan.

By averaging the measured amplitude and phase of the uniformly coupled elements, suggestive comparison with the designed values can be made as shown in Table I. Different amplitude distribution of the elements could partly be explained by the offset field created by multiple reflections in the measurement system. The other reason could be the losses in the GCPW-transmission lines due to over-etching of the slots. Microscope measurements showed that the slot width is about 16 µm, twice the designed value. Different slot width changes the characteristic impedance of the line and could partly explain the weaker amplitude of the elements which has a longer coupling stub.

TABLE I. MEASURED AMPLITUDE AND PHASE

Coupling element			**Measured Value**	
Stub length	***Type***	***Relative phase shift (deg.)***	***Normalized amplitude(dB)***	***Phase(deg.)***
54 µm	short	0	0	2.9
195 µm	open	90	-9.93	93.3
200 µm	short	180	-13.69	119.0
366 µm	open	270	-11.04	226.5

V. CONCLUCIONS

In this paper, the near-field measurements of a 120-GHz static reflectarray antenna are described. Measurement results show that the method can be used to gather information from antenna elements. Resolution of the selected probe and the signal-to-noise ratio of the measurement are sufficient for distinguishing individual antenna elements from the ground plane reflection.

The major issue of the near-field probing of the reflectarray surface is the unavoidable multiple reflections which are interfering the accurate analysis of the measurement results. In order to characterize the modulation efficiency of the antenna elements with the measurement method presented, comprehensive calibration model of the measurement scheme will be designed in the future.

REFERENCES

[1] J. Huang and J. A. Encinar, *Reflectarray Antennas,* Hoboken, New Jersey: John Wiley & Sons, Inc., 2007.

[2] A. Tamminen, J. Ala-Laurinaho, J. Häkli, P. Koivisto, J. Säily, A. Luukkanen, and A. V. Räisänen, "Reflectarray design for 120 GHz MMID application: simulation results." in *Sixth ESA Workshop on Millimetre Wave Technology and applications,* Espoo, Finland, 2011.

[3] D. Pozar, S. D. Targonski, and H. D. Syrigos, "Design of millimeter wave microstrip reflectarrays" *IEEE Transactions on Antennas and Propagation*, vol. 45, pp. 287-296, February 1997.

[4] K. Li, C. H. Cheng, T. Matsui, and M. Izutsu, "Coplanar patch antennas: principle, simulation and experiment," in *Digest of the Society International Sympozium on Antennas and Propagation*, Boston, MA, 2001.

[5] S. Dieter and W. Menzel, "High-resolution probes for near-field measurements of reflectarray antennas" *IEEE Antennas and Wireless Propagation Letters*, vol. 8, pp. 157-160, 2009.

[6] C.-C. Tien, C.-K. C. Tzuang, and S. T. Peng, "Transmission characteristics of finite-width conductor-backed coplanar waveguide" *IEEE Transactions on Microwave Theory and Techniques*, vol. 41, pp. 1616-1624, September 1993.

[7] M. D. Weiss, B. Zadler, S. Schafer, and J. Scales, "Near field millimeter wave microscopy with conical teflon probes" *Journal of Applied Physics*, vol. 106, no. 4, pp. 044912-044912-8, August 2009.

B Publication II

S. Mäkelä, A. Tamminen, J. Ala-Laurinaho, and A. V. Räisänen, "Calibration method for near-field Measurement used in reflectarray characterization," in *43rd European Microwave Conference*, Nuremberg, Germany, Oct. 2013, pp. 183-186.

Calibration Method for Near-Field Measurement Used in Reflectarray Characterization

S. Mäkelä, A. Tamminen, J. Ala-Laurinaho, and A. V. Räisänen
MilliLab, Department of Radio Science and Engineering
Aalto University
Espoo, Finland
Email: sampo.makela@aalto.fi

***Abstract*—In this paper, a calibration method of a near-field measurement for reflectarray characterization is presented. First, a waveguide calibration is performed to eliminate the influence of the directional coupler used in the measurement scheme. Second, the reflection measurement is modelled with a metal plate drawn away from the probe aperture. With this model, the variation of the measurement distance due to alignment errors can be taken into account in the reflectarray element characterization. A staircase-shaped test target has been manufactured and measured for validating the functionality of the model.**

I. Introduction

In recent years, a reflectarray antenna, which combines the best features of phased arrays and reflector antennas, has become an appealing low-cost alternative for high-gain antennas due its flatness and beam shaping flexibility [1]. Strong interest in reconfigurable reflectarrays has been risen especially at millimeter-wave frequencies where the use of directly radiating phased arrays is impractical due to inevitable losses in the feed network [2]. However, a contemporary trend of rising frequency in reflectarray applications makes its performance very vulnerable to manufacturing errors. In addition, the use of reconfigurable phase shifters or stacked patches increases the uncertainty of operation even more. The major part of the reflectarray design procedure is to evaluate reflection characteristics of the unit cells, often called as S-curves, which can be obtained with commercial software by using an infinite array approach with Floquet's periodic boundary conditions. However, a practical method to verify the performance of the fabricated element is needed.

Near-field probing has been found to be a potential method for experimental characterization of the reflectarray element performance. In [3], a 15 GHz reflectarray consisting of printed dipoles has been experimentally studied using measurements with an integrated miniaturized monopole probe placed in the reactive near-field of the scattering element. A different approach has been presented by Dieter and Menzel in [4]. They propose characterization of a 30 GHz reflectarray by Fresnel-region near-field measurements with three different high-resolution probes. The method can also be used for characterization of the whole reflectarray, and hence for finding possible defective regions of the antenna.

However, applying the characterization method to higher frequencies is challenging due to alignment issues of a separate transmitter and receiver. A way to overcome this problem is to use an integrated near-field probe [5] or waveguide directional coupler [6]. Calibration of such a system cannot be done directly with a vector network analyzer (VNA) but can be established manually as presented in Section III-A. Another problem with the high frequency is the variation of the measurement distance. At 120 GHz a $100\,\mu\text{m}$ change in distance turns the measured phase of the received reflected field by $28.8°$. This is a significant issue, which has not been discussed in the previous publications on the near-field probing.

II. 120 GHz Reflectarray for Radar Application

We are currently developing a 120 GHz reconfigurable reflectarray at Aalto University Department of Radio Science and Engineering in collaboration with VTT (Technical Research Centre of Finland). Design goal is to develop a millimeter-wave radar for imaging and identification applications. In addition to the reflectarray design, a millimeter-wave front-end for illumination is being developed. The reflectarray cell consists of a coplanar patch antenna (CPA) element, similar as in [7], which is coupled with a conductor-backed coplanar waveguide (CBCPW) transmission line. Three capacitive shunt type microelectromechanical systems (MEMS) phase shifters are located in the CBCPW shorting the line when pulled down, and hence inducing a phase-shift proportional to the distance to the CPA. The state of the MEMS phase shifters can be rapidly changed, which provides the possibility to use the reflectarray for real-time video imaging. Preceding the MEMS-controlled reflectarray, three static ones have been manufactured for measurements. Design procedure of these antennas is described in details in [8]. MEMS phase shifter design and measurement results of static reflectarrays with an efficiency analysis based on near-field imaging of the reflectarray aperture field are discussed in [9]. A photograph of the CPA element in the static reflectarray is presented next to the fabricated MEMS phase shifter in Fig. 1.

Manufactured reflectarrays have been found to suffer from over-etching, which decreases the performance of the antenna. Over-etching reduces the effective height of the CPA, which determines its resonant frequency. CPAs, like any other type of microstrip antennas, are narrow band (about 5 GHz in this case), and hence really sensitive for dimensional changes. Further investigation showed that CPAs were in resonance at 132 GHz, which is 10 percent higher than the designed central frequency. This problem is, however, related to the manufacturing process which can be improved.

Measurement scheme for the near-field element characterization, which is represented in Fig. 2, is described in more detail in [6]. Measurements are performed with a millimeter-wave vector network analyzer (MVNA), which includes a fundamental frequency Gunn-oscillator mm-wave extension used as a transmitter. The receiver is a D-band harmonic mixer where the received signal is down-converted to a microwave frequency. Transmitter and receiver are connected together with a WR-6 waveguide directional coupler. Between the transmitter and the directional coupler, a 10-dB waveguide attenuator is used to reduce the effects of the multiple reflections.

III. Calibration

Systematic errors are commonly the foremost factor of uncertainty in VNA measurements. These errors are caused by mismatch between components of the test unit, finite directivity of directional couplers, and crosstalk between channels. In order to reduce the effect of systematic errors, calibration is established by measuring S-parameters of precise calibration standards with known electrical characteristics, in the place of the device under test (DUT). The actual S-parameters of the DUT can be calculated from the calibration data by using conventional de-embedding techniques.

A. 3-Term Error Model for Reflection Measurement in Waveguide Environment

The effect of systematic errors can be significantly reduced with an error model. For reflection measurements the simplest way is a response calibration, which can be done by measuring either short or open circuit in addition to a matched load for solving error terms. However, this calibration method does not take into account the port match error, which reduces the accuracy of the measurement. The most common method for VNA error correction is a short-open-load-through (SOLT) calibration, where the last one (through) is only applied in 2-port measurements. Terms in the model are directivity error E_{DF}, port match error E_{SF} and reflection tracking error E_{RF}. In most cases VNA calculates these error coefficients, but when non-standard external transmitter and receiver units are used, the calibration process has to be done manually.

If the measurement plane locates at a distance from the DUT, the actual impedance of the DUT can be determined from the measured one by using de-embedding procedure, which requires that the electrical properties of the intervening structure are known [10]. The structure between the measurement plane and DUT is described with a scattering matrix. If a load Z_L with known reflection coefficient Γ_L terminates

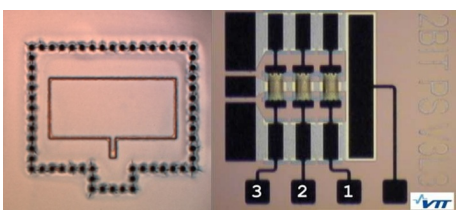

Fig. 1. Coplanar patch antenna (left) with a 200 µm long open-ended CBCPW transmission line, which will be replaced with MEMS phase shifter (right) in the reconfigurable reflectarray. Samples are fabricated at VTT, Finland.

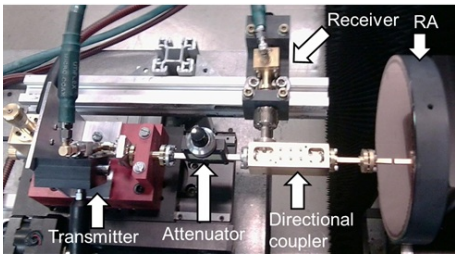

Fig. 2. Near field measurement setup for reflectarray characterization.

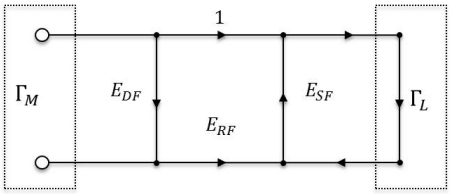

Fig. 3. Three-term error model for reflection measurement.

the embedding network represented with a scattering matrix S, the reflection coefficient of the input can be expressed with Eq. (1). Three-term error model is presented as a flow chart in Fig. 3, where the actual reflection coefficient (Γ_L in Eq. (2)) of the load can be solved from the measured one (Γ_M) by using Eq. (1). To make Eq. (2) easier to solve, variables a, b and c defined in Eq. (3) are used. Eq. (2) can be now written as Eq. (4).

$$\Gamma_s = S_{11} - \frac{S_{12}S_{21}}{S_{22} - \frac{1}{\Gamma_L}} \tag{1}$$

$$\Gamma_L = \frac{\Gamma_M - E_{DF}}{E_{RF} - E_{SF}E_{DF} + \Gamma_M E_{SF}} \tag{2}$$

$$\begin{cases} a = E_{RF} - E_{SF}E_{DF} \\ b = E_{DF} \\ c = -E_{SF} \end{cases} \tag{3}$$

$$\Gamma_L = \frac{\Gamma_M - b}{a - \Gamma_M c} \tag{4}$$

In order to solve parameters a, b and c from Eq. (4), reflection coefficients Γ_{M1}, Γ_{M2} and Γ_{M3} have to be measured with corresponding loads Z_1, Z_2 and Z_3 with known reflection coefficients Γ_1, Γ_2, and Γ_3, respectively.

$$a = \frac{\Gamma_{M2} - \Gamma_{M1} - (\Gamma_{M1}\Gamma_1 - \Gamma_{M2}\Gamma_2)}{\Gamma_2 - \Gamma_1} \tag{5}$$

$$b = \Gamma_{M1} - \Gamma_1 a + \Gamma_{M1}\Gamma_1 c \tag{6}$$

$$c = \tag{7}$$

$$\frac{(\Gamma_2 - \Gamma_1)(\Gamma_{M3} - \Gamma_{M1}) - (\Gamma_3 - \Gamma_1)(\Gamma_{M2} - \Gamma_{M1})}{(\Gamma_2 - \Gamma_1)(\Gamma_{M1}\Gamma_1 - \Gamma_{M3}\Gamma_3) - (\Gamma_3 - \Gamma_1)(\Gamma_{M1}\Gamma_1 - \Gamma_{M2}\Gamma_2)}$$

The accuracy of the calibration depends on the availability of high-quality calibration standards. For coaxial media, it is

easy to fabricate a set of three distinct impedances, such as open-circuit, short-circuit, and matched load. In a waveguide environment the task is not that straightforward except for the short-circuit standard, which can be applied by using just a flat metal flange. If the waveguide is terminated with an ideal matched load, the amplitude of the reflected signal is exactly zero. However, a perfect matched load is impossible to fabricate for waveguide environment, which means that a small reflection ΔE_{DF} from an unideal termination is always present. ΔE_{DF} adds up with the calibration model error term E_{DF}, and hence reduces the accuracy of the calibration. The effect of ΔE_{DF} can be taken into account with a sliding termination. When the position of the termination is changed, angle between E_{DF} and ΔE_{DF} also changes and forms an error circle. When the measurement is done with a multiple positions of the load, the actual E_{DF} can be solved from the central point of this circle [11]. Measured reflection coefficient of an open-ended waveguide probe is $0.233\angle 40.03°$, when a static load is used, and $0.227\angle 41.98°$ when the reflection from an unideal load is taken into account. An amplitude error of 2.5% and phase error of $1.96°$ may not sound much, but can be truly significant, when the reflection from the probe is used as a reference point.

Determination of the calibration standard for open-circuit is slightly more complicated but can be established using offset shorts [12]. In terms of reflection coefficients in a waveguide reflection measurement, open-circuit standard can be achieved by adding a quarter-wave waveguide section, often called as an offset shim, between the reference plane and a short-circuit flange. However, for the WR-6 waveguide band, the thickness of such shim would be only 0.703 mm, thus it could easily bend or become distorted during use, and hence is not a practical choice for a calibration standard. In waveguide calibration kits for millimeter-wave frequency range, a quarter-wave shim is commonly replaced with two precise waveguide sections, the separation of which in length (thickness) is a quarter of a guided wavelength (Eq. (8)) at the central frequency of the waveguide band. Therefore, two measurements are needed to realize a calibration standard for open circuit.

$$\lambda_g = \frac{\lambda_0}{\sqrt{1-(\frac{\lambda_0}{\lambda_c})^2}}, \tag{8}$$

where $\lambda_c = 2a$ and a is the width of the waveguide. For reflectarray central frequency, 120 GHz, guided wavelength in a WR-6 waveguide is 3.8 mm. The waveguide section can be expressed as:

$$S_{thru} = \begin{bmatrix} 0 & e^{-\gamma s} \\ e^{-\gamma s} & 0 \end{bmatrix}, \tag{9}$$

where s is the length of the transmission line and $\gamma = \alpha + j\beta$ is the complex propagation constant, which can be separated to the attenuation constant α and the phase constant β. The waveguide section is assumed to be perfectly matched ($S_{11} = S_{22} = 0$). Reflection measurement is calibrated with a standard D-band waveguide calibration kit. The calibration kit includes waveguide sections with lengths of 2.542 mm and 3.2741 mm. The difference in length of these sections is 0.7316 mm, which means $0.1915\lambda_g$ in guided wavelengths at 120 GHz. To obtain the response of a waveguide section having the length (thickness) of the difference between the two measured offset shorts, the short-circuited end of the thinner waveguide section has to be chosen as the reference plane. Offset short with a thicker waveguide section can be de-embedded to this plane by using Eq. (1).

$$\Gamma_{ref} = S_{11} - \frac{S_{12}S_{21}}{S_{22} - \frac{1}{\Gamma_{os}}}. \tag{10}$$

$$\Gamma_{ref} = \tau_{os} e^{-2\gamma s} \tag{11}$$

$$\frac{|\Gamma_{ref}|}{|\Gamma_{os}|} e^{j(\phi_{ref} - \phi_{os})} = e^{-2(\alpha + j\beta)s} \tag{12}$$

The phase constant β, and the attenuation constant α, can be calculated from the phase difference of two offset shorts.

$$\beta = \frac{\phi_{ref} - \phi_{os}}{2s} \tag{13}$$

$$\alpha = -\frac{\ln(\frac{|\tau_{ref}|}{|\tau_{os}|})}{2s} \tag{14}$$

However, determination of the attenuation constant this way is not feasible due to probable standing wave propagation between the directional coupler and the short-circuit termination at the end of the transmission line. Although its effect could be taken in account by using a sliding short-circuit termination, the waveguide attenuation is neglected in this model.

B. Modelling of the Near-Field Measurement

An accurate model of the reflection measurement is mandatory for implementing the measurement method to reflectarray characterization. At this point, the measurement scheme is assumed to be calibrated to the waveguide flange, where the probe is attached.

1) Distance calibration with an moving metal plate: A way to verify the proposed measurement method is to measure a sample with known quantities. A convenient way here is to use a flat metal plate as a sample. When the plate is moved away from the probe aperture, the phase of the received field is changing with respect to twice the distance d between the plate and the probe compared to the free-space wavelength. Respectively, also the amplitude of the received field is decreasing with d and approaching that of the reflection coefficient of the probe. For a flat metal plate manufactured from good conductor such as aluminium, the reflection coefficient can be assumed to be exactly -1. The situation can be compared to the case of two antennas pulled away from each other. From the results presented in Fig. 4 one can come to a conclusion that the measurement distance should not be more than a half of a wavelength since the variation of the measured phase is linear only till this point. A strong amplitude fluctuation can be noticed at this range, which is due to standing wave caused by probe-target interaction.

2) Test target: Staircase shaped test target has been manufactured for verifying the functionality of the proposed measurement method. A piece of high quality aluminium has been milled to the staircase form, where each 10 mm wide step has a $200\,\mu$m difference in depth to the adjacent step. This corresponds to a phase difference of $57.6°$ for the back-reflected field from adjacent steps of the test target. To rule out machining errors, its profile was measured with a dial indicator.

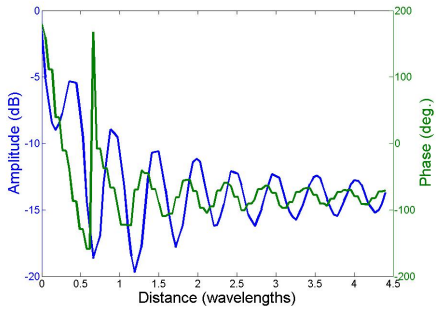

Fig. 4. Amplitude and phase of the measured reflection coefficient when an aluminium plate is drawn apart from the probe aperture. The transient in phase after 0.6λ is caused due to under-sampling of the measurement.

IV. Results

Comparison between the test target phase response measured with the proposed near-field measurement method and calculated values is presented in Fig. 5. At the center of the test target, the measurement result is in a good agreement with a result calculated directly from the test target profile measured with a dial indicator. At small distances the change of phase between the adjacent steps is lower than the calculated one, but this non-linearity can be taken into account. It also indicates that the test target was slightly misaligned during the measurement. However, alignment errors can be taken into account with test target by integrating the dial indicator to the measurement setup.

The measurement method can be applied for reflectarray characterization as follows. In the designed reflectarray, more than 70 % of the surface area is covered with a ground plane. Thus, by filtering the reflection from antenna elements out of the measurement data, the measurement distance for every antenna element can be calculated. Distance calibration is established by fitting the measured reflection coefficient to the result of the outdrawn aluminium plate.

V. Conclusion

In this paper, a calibration method of a near field measurement for reflectarray characterization is presented. To compensate the effect of the directional coupler and relate the measured electric field to the actual reflection coefficient of the terminating impedance, a waveguide calibration is established. Because the near-field reflection measurement is performed at such a high frequency, the variation of measurement distance makes a significant effect to the measurement result in both amplitude and phase. Effect of the measurement distance is modelled with a metal plate drawn away from the probe aperture. Linear relation with a measured phase was observed until the distance of a half of the free-space wavelength.

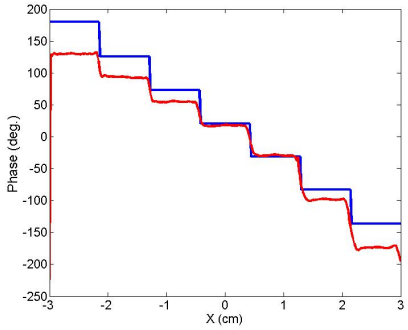

Fig. 5. Comparison between the phase response of the test target profile measured with a near-field measurement (red line) and calculated phase (blue line).

Acknowledgment

This work has been partially supported by Tekes, the Finnish Funding Agency for Technology and Innovation, through SIMIDS project, and by the Academy of Finland under the Centre of Excellence in Research Programme.

References

[1] D. Pozar, S. Targonski, and H. Syrigos, "Design of millimeter wave microstrip reflectarrays," *IEEE Transactions on Antennas and Propagation*, vol. 45, pp. 287–296, Feb. 1997.

[2] R. Sorrentino, R. Gatti, and L. Marcaccioli, "Recent advances on millimetre wave reconfigurable reflectarrays," in 3^{rd} *European Conference on Antennas and Propagation*, Mar. 2009, pp. 2527–2531.

[3] J.-D. Lacasse and J.-J. Laurin, "A method for reflectarray antenna design assisted by near field measurements," *IEEE Transactions on Antennas and Propagation*, vol. 54, pp. 1891–1897, Jun. 2006.

[4] S. Dieter and W. Menzel, "High-resolution probes for near-field measurements of reflectarray antennas," *IEEE Antennas and Wireless Propagation Letters*, vol. 8, pp. 157–160, Jan. 2009.

[5] S. Dieter, Z. Yang, and W. Menzel, "A 77 GHz near-field probe with integrated illuminating waveguide," in *German Microwave Conference*, Mar. 2011, 4 p.

[6] S. Mäkelä, J. Ala-Laurinaho, A. Tamminen, A. Räisänen, P. Koivisto, J. Säily, J. Häkli, P. Rantakari, R. Tuovinen, and A. Luukanen, "Near-field measurements of a millimeter-wave reflectarray at 120 GHz," in *Proceedings of the* 42^{nd} *European Microwave Conference, Amsterdam, The Netherlands*, Oct. 2012, pp. 807–810.

[7] K. Li, C. Cheng, T. Matsui, and M. Izutsu, "Coplanar patch antennas: principle, simulation and experiment," in *IEEE Antennas and Propagation Society International Symposium*, vol. 3, Jul. 2001, pp. 402–405.

[8] A. Tamminen, J. Ala-Laurinaho, J. Häkli, P. Koivisto, J. Säily, A. Luukkanen, and A. V. Räisänen, "Reflectarray design for 120 GHz MMID application: simulation results," in *6th ESA Workshop on Millimetre Wave Technology and applications, Espoo, Finland*, May. 2011.

[9] A. Tamminen, S. Mäkelä, J. Ala-Laurinaho, J. Häkli, P. Koivisto, P. Rantakari, J. Säily, A. Luukanen, and A. V. Räisänen, "Reflectarray design for 120-GHz radar application: measurement results," *IEEE Transactions on Antennas and Propagation*, accepted for publication, 2013.

[10] R. F. Bauer and P. Penfield Jr., "De-embedding and unterminating," *IEEE Transactions on Microwave Theory and Techniques*, vol. 22, pp. 282–288, Mar. 1974.

[11] D. M. Pozar, *Microwave Engineering, 4th Edition*. Hoboken, NJ: John Wiley & Sons Ltd., 2011.

[12] W. Wiatr, "Line-length optimization of offset-short standards for broadband VNA calibration," in 18^{th} *International Conference on Microwave Radar and Wireless Communications*, Jun. 2010, 4 p.